الجـــــــــــــــــــــمهـوريـــــة الجـــــــــــــزائـريـة الديمـــــــقـراطيـة الـشـــــــــعبيـة

REPUBLIQUE ALGERIENNE DEMOCRATIQUE ET POPULAIRE

وزارة التـــــــــــــــــــــــــــــعـليـم العـــــــالي والبـــــــــــحث العـــــلـمـــي

Ministère de l'Enseignement Supérieur et de la Recherche Scientifique

جـــــــــــــــامعة أبي بكـــر بـلـقـايد – تـلمســـــــــــــــان –

Université Aboubakr Belkaïd – Tlemcen –

Faculté de TECHNOLOGIE

THESIS

Presented for the obtaining the **degree** of **DOCTORATE 3rd Cycle**

In: Mechanical Engineering

Specialty: Mechanical Construction

Presented by: Karima BOUSMAHA

Subject

Dynamic and static study of plates made of porous advanced materials reinforced with carbon nanotubes

Publicly defended ,18/06/2026, in front of a board of examiners:

M. Mohammed Amirat	Professor	Univ. Tlemcen	Chairman
M. Sid Ahmed Belalia	Professor	Univ. Tlemcen	Supervisor
M. Sidi Mohammed Chorfi	Assoc. Prof. 'A'	Univ. Tlemcen	Co-Supervisor
M. Ismail Bensaid	Assoc. Prof. 'A'	Univ. Tlemcen	Examiner 1
M. Mohammed Nadjib Serdoun	Assoc. Prof. 'A'	ESSAT	Examiner 2
M. Abdelouahed Tounsi	Professor	Univ. Sidi Bel Abbes	Guest 1

Academic year : 2025/2026


بسم الله الرحمن الرحيم

Dedication

This thesis is dedicated to:

My dear parents,

My grandfather and my uncle may Allah welcome them into His vast paradise,

My dear little sister,

My dear friend, a PhD candidate in Telecommunications, who has been like a sister for me,

All my dear friends,

My family,

To all my colleagues in the Class of 2022 in Mechanical construction,

And to all those who have helped me,

Acknowledgements



First and foremost, I would like to thank Allah for offering me the strength, courage, and will to successfully complete this modest work.

I sincerely express my thanks and deep gratitude to my thesis supervisor **Pr**. Sid Ahmed Belalia, and my co-supervisor, **M**. Sidi Mohammed Chorfi, I wish to convey my sincere appreciation to them for their expertise, trust, guidance, and encouragement throughout this work. I extend to them my respectful wishes for continued success, in all their future professional and personal endeavors.

With sincere gratitude, I acknowledge the members of jury, especially **Pr.** Mohammed Amirat who did me the honor of chairing the jury and **M.** Ismail Bensaid and **M.** Mohammed Nadjib Serdoun who agreed to review my thesis.

I warmly thank my dear parents for their sacrifices, constant encouragement, and help throughout my studies.

I am pleased to sincerely thank the entire Mechanical Engineering Department team for their support and assistance through my years of study.

I wish to express my sincere thanks to everyone who, directly or indirectly, has contributed toward the successful completion of this thesis.

Abstract

Functionally graded material (FGM) sandwich plates are widely used as structural components in various branches of engineering such as mechanical, aerospace, civil, and naval engineering. To ensure proper design and performance of these structures, it is essential to analyze and understand their behavior.

In this thesis, both the static and dynamic behavior of FGM sandwich plate incorporate the effect of porosity distribution and Carbone nanotube (CNT) reinforcement are analyzed using the p-version of the Finite Element Method (p-FEM) based on the First- order Deformation Theory (FSDT). The sandwich plate consists of three layers, where the core layer is made of functionally graded carbon nanotube-reinforced material (FG-CNTR), including three distribution types: Uniform, FG-X, and FG-O. The top and bottom face sheets are composed of a porous functionally graded material (FGM), modeled using five different porosity distributions: Perfect, Imperfect I, …, V. The numerical results demonstrate convergence and are validated through comparison with previously published data, confirming the accuracy of the proposed formulation. The dynamic behavior is analyzed by comparing the results obtained from the p-version of the (FEM) with the mode superposition approach those derived from a newly developed analytical solution formulated within the framework of the Classical Plate Theory (CPT).

The effects of several parameters such as the carbon nanotube distribution pattern, porosity model, CNT volume fraction, geometric characteristics, mechanical loading, volume fraction exponent, damping coefficient, and boundary conditions are thoroughly illustrated and analyzed for static and dynamic responses.

Keywords: FGM; sandwich plates; *p*-FEM; dynamic response; static analysis; porosities; FG-CNTRC; FSDT; Carbon nanotubes distribution; bending analysis.

Résumé

Les plaques sandwich en matériau à gradient fonctionnel (FGM) sont largement utilisées comme composants structurels dans divers domaines de l'ingénierie, tels que l'ingénierie mécanique, aérospatiale, civile et navale. Pour assurer une conception appropriée et des performances optimales de ces structures, il est essentiel d'analyser et de comprendre leur comportement.

Dans cette thèse, les comportements statique et dynamique des plaques sandwich FGM, en tenant compte de l'effet de la distribution de porosité et du renforcement par nanotubes de carbone, sont analysés en utilisant la méthode des éléments finis (MEF) en p-version basée sur la théorie des déformations du premier ordre. La plaque sandwich est constituée de trois couches, où la couche centrale est faite d'un matériau renforcé par des nanotubes de carbone à gradient fonctionnel (FG-CNTR), comprenant trois types de distribution : Uniforme, FG-X et FG-O. Les faces supérieure et inférieure sont composées d'un matériau à gradient fonctionnel poreux (FGM), modélisé selon cinq distributions de porosité différentes : Parfaite, Imperfect I, …, V. Les résultats numériques démontrent la convergence et sont validés par comparaison avec des données publiées précédemment, confirmant l'exactitude de la formulation proposée. Le comportement dynamique est analysé en comparant les résultats obtenus par la p-version de la MEF utilisant la méthode de superposition des modes avec ceux dérivés d'une solution analytique récemment développée, formulée dans le cadre de la théorie classique des plaques.

Les effets de plusieurs paramètres, tels que le type de distribution des nanotubes de carbone, le modèle de porosité, la fraction volumique de Carbone nanotube, les caractéristiques géométriques, la charge mécanique, l'exposant de la fraction volumique, le coefficient d'amortissement et les conditions aux limites, sont décrits et analysés en profondeur pour les réponses statiques et dynamiques.

Mots clés : FGM ; plaques sandwich ; p-MEF ; réponse dynamique ; analyse statique ; porosités ; FG-CNTRC ; Théorie du premier ordre des plaques ; distribution des nanotubes de carbone ; analyse de flexion.

ملخص

تُستخدم صفائح الساندويتش المصنوعة من المواد متدرجة الخصائص على نطاق واسع كمكونات هيكلية في مختلف فروع الهندسة، مثل الهندسة الميكانيكية، والهندسة الفضائية، والهندسة المدنية، والهندسة البحرية. لضمان تصميم مناسب وأداء مثالي لهذه الهياكل، من الضروري تحليل سلوكها وفهمه.

في هذه الأطروحة تم تحليل السلوكين الثابت والديناميكي لصفائح الساندويتش مع الأخذ بعين الاعتبار تأثير توزيع المسامية وتعزيزها بـالأنابيب النانوية الكربونية باستخدام النسخة p من طريقة العناصر المحددة المستندة إلى نظرية تشوه القص من الرتبة الأولى. تتكون صفيحة الساندويتش متدرجة الخصائص من ثلاث طبقات، حيث تتألف الطبقة الوسطى من مادة معززة بـالأنابيب النانوية الكربونية، وتشمل ثلاثة أنواع من التوزيع Uniform، FG-X وFG-O، أما الطبقات العليا والسفلى فهي مكونة من مادة متدرجة الخصائص مسامية تم نمذجتها وفق خمسة توزيعات مختلفة للمسامية Perfect، Imperfect I،...،V. تُظهر النتائج العددية التقارب وتم التحقق من صحتها بالمقارنة مع البيانات المنشورة مسبقًا، مما يؤكد دقة الصياغة يتم تحليل السلوك الديناميكي من خلال مقارنة النتائج التي تم الحصول عليها بواسطة (p-FEM) باستخدام طريقة تراكب الأوضاع (mode superposition method) مع النتائج المستمدة من حل تحليلي تم تطويره حديثًا وصياغته ضمن إطار نظرية الصفائح الكلاسيكية.

قدمت هذه الدراسة تأثير عدة عوامل مثل نوع توزيع الانابيب النانوية الكربونية، المسامية، الكسر الحجمي للكربون، الخصائص الهندسية، القوى الميكانيكية، أسس كسر الحجم، معامل التخميد، والظروف الحدودية بشكل مفصل للاستجابات الثابتة والديناميكية.

الكلمات المفتاحية :المواد المتدرجة وظيفيا؛ صفائح الساندويتش؛ النسخة p من طريقة العناصر المحددة؛ الاستجابة الديناميكية؛ التحليل الثابت؛ المسامية؛ النسخة p من طريقة العناصر المحددة؛ توزيع الأنابيب النانوية الكربونية؛ تحليل الانحناء.

Contents

Contents ..... **I**

List of figures ..... **II**

List of tables ..... **III**

List of abbreviations ..... **IV**

List of symbols ..... **V**

General Introduction **1**

Chapter 1 Literature Review

Objective 5

1.1. Free vibration of FGM sandwich plate 6

1.2. Free vibration and static analysis of porous FGM sandwich plate 7

1.3. Free vibration and static analysis of FGM sandwich plate reinforced with CNTs 9

1.4. Dynamic analysis of porous sandwich FG-CNTRC plate 9

1.5. Research gaps and motivation of the current work 10

Chapter 2 Theoretical background and material modeling

Objective 11

2.1. Functionally Graded Materials (FGM) 12

2.1.1. Introduction to functionally graded materials 12

2.1.1.1 FGM definition and concept 12

2.1.1.2 FGM history and evolution [Koizumi (1997)] 13

2.1.2. Classification and types of FGM material 14

2.1.2.1 FGM on ceramic and metal base 14

2.1.2.2 Porous FGM 14

2.1.2.3 CNT-Reinforced Functionally Graded Materials 15

2.1.3. Material properties of FGM 16

2.1.3.1 Power-law(P-FGM) 16

2.1.3.2 Exponential-law(E-FGM) 16

2.1.3.3 Sigmoid law(S-FGM) 16

2.1.4. Industrial applications of FGM 16

2.2. Sandwich composite structure 18

2.2.1. Definition and fundamental principles 18

2.2.2. Advantages of sandwich structures 18

2.2.3. Composition of a Sandwich Structure 19

2.2.3.1 Face sheets(skins) 19

2.2.3.2 Core 19
2.2.3.3 Adhesives and interfaces 21
2.2.4. Sandwich structure applications 22
2.3. Porosity in Sandwich Plates 23
2.3.1. Porosity definition and origin 23
2.3.2. Effects of porosity on structure properties 23
2.4. Carbon 24
2.4.1. Electronic structure 24
2.4.2. Forms of carbon 24
2.4.2.1 Graphite 25
2.4.2.2 Diamond 25
2.4.2.3 Fullerene 26
2.5. Carbon nanotube 26
2.5.1. Discovery of carbon nanotubes 27
2.5.2. Carbon nanotube structure 28
2.5.3. Properties of carbon nanotubes 28
2.5.3.1 Mechanical properties 29
2.5.3.2 Electrical properties 29
2.5.3.3 Chemical properties 29
2.5.3.4 Physical properties 30
2.5.3.5 Optical properties 30
2.5.4. Synthesis of Carbon Nanotubes 30
2.5.5. Carbon nanotube applications 31

Chapter 3 Plate theory

Objective 33
3.1. Theory of plates including shear effects 34
3.1.1. Theory of thin plates 34
3.1.1.1 Classic plate theory (CPT) 34
3.1.2. Theory of thick plates 35
3.1.2.1 First-order shear deformation theory (FSDT) 35
3.1.3. Higher-order shear deformation theory (HSDTs) 36
3.1.4. Refined Plate Theory (RPT) 39
3.1.5. Quasi-3D Theory 40
3.1.6. Layered approach 40
3.1.6.1 Discrete-layer models 40

3.1.6.2 Zigzag models 40

Chapter 4 P-version of Finite Element Method

Objective 42

4.1. Brief history of the p-version of the finite element method 43

4.2. Advantages of the p-version 43

4.3. Limitations of the p-version 44

4.4. Comparison between version-p and -h 44

4.5. Mesh adaptation 45

4.6. Numerical implementation of the p-version approach 46

4.6.1. Legendre polynomials 46

4.6.2. Shifted Legendre polynomials 46

4.6.3. *p*-version and hierarchical interpolation functions 47

4.6.3.1 One-dimensional elements 48

4.6.3.2 Two-dimensional p-elements 50

Chapter 5 Finite element formulation based on FSDT

Objective 54

5.1. FGM sandwich plate model 55

5.2. Theoretical formulation 55

5.2.1. Displacement fields 55

5.2.2. Strain–Displacement relations 56

5.2.3. Stress–Strain relations 57

5.2.4. Transverse shear correction factors 58

5.2.5. Kinetic and Strain energy of FGM sandwich plate 58

5.2.6. Equation of motion 59

5.3. Modeling using rectangular p-element 59

5.3.1. Displacement field approximation and shape functions 60

5.3.2. Mass and Stiffness matrices 61

5.4. Porous FGM sandwich plate reinforced with CNT 61

5.4.1. Porosity-dependent FG sandwich plates 61

5.4.1.1 Imperfect I- FGM (even) 62

5.4.1.2 Imperfect II- FGM (uneven) 62

5.4.1.3 Imperfect III- FGM (logarithmic-uneven) 62

5.4.1.4 Imperfect IV-FGM (linear-uneven) 63

5.4.1.5 Imperfect V-FGM (sinusoidal -uneven) 63

5.5. Material properties of CNTs 63

Chapter 6 Programming Techniques

Objective 67

6.1. Software and hardware used 68

6.2. Flowchart of the program 68

6.3. Program description 68

6.3.1. Data file 68

6.3.1.1 Element parameters 68

6.3.1.2 Physical parameters 70

6.3.1.3 Geometric parameters 71

6.3.1.4 Loading Conditions (Static and Dynamic) 71

6.3.1.5 Boundary conditions 71

6.3.2. Programming 72

6.3.2.1 Subroutine PROMAT 72

6.3.2.2 Subroutine JMATRIX 72

6.3.2.3 Subroutine GAUSS 72

6.3.2.4 Subroutine CONNECT 73

6.3.2.5 Subroutines STIFF & MASS & INVERT 73

6.3.2.6 Subroutine JACOBI 73

6.3.2.7 Subroutine SORT 74

6.3.2.8 Subroutine GFUNCT 74

6.3.2.9 Subroutine MODE 74

6.3.2.10 Subroutine DEFLECTION 74

6.3.2.11 Subroutine DRESP 74

6.3.2.12 Subroutine LOADF 74

6.3.2.13 Subroutine DISPLAY 74

6.3.3. Output file 74

Chapter 7 Static and dynamic analysis of porous FGM sandwich plate reinforced CNT

Objective 76

7.1. Static analysis 77

7.1.1. Numerical solution procedure 77

7.1.2. Convergence analysis and validation modeling 77

7.1.2.1 Validation free vibration 77

7.1.2.2 Validation static analysis 80

7.2. Dynamic analysis 83

7.2.1. Analytical solution for FGM plates 83

7.2.2. FEM solution 83
7.2.3. Validation and Convergence 84
7.3. Parametric study 85
General Conclusions and Perspectives 101
Bibliography 103
Appendix A 119
A.1 Analytical solution for FGM plates 119

List of figures

Figure 2.1: Analytical model for a FGM layer: a) First approach b) Second approach 13
Figure 2.2: Volume fraction of metal along the thickness 13
Figure 2.3 : Different sandwich core types [Kausar et al. (2023)]. 21
Figure 2.4 : Electronic Configuration of a Carbon Atom 24
Figure 2.5 : Different Allotropes of Carbon 25
Figure 2.6 : Graphite structure 25
Figure 2.7 : Diamond structure 26
Figure 2.8 : Fullerene structure 26
Figure 2.9 : Schematic of how graphene could roll up to form a carbon nanotube 27
Figure 2.10 : Types of Carbon Nanotubes structure : a) SWCNT ; b) DWCNT ; c) MWCNT 28

Figure 3.1: Love Kirchhoff plate kinematics (CPT) [Reddy (2003)]. 34
Figure 3.2 : Reissner-Mindlin plate kinematics (FSDT) [Reddy (2003)]. 36
Figure 3.3 : Comparison of transverse shear shape function of the different models 39
Figure 3.4 : Schematic representation of the zig-zag displacement field of first order zig-zag models [D. Baptiste, R. O. Polit, R. A. Chabot, E. M. Boussu, and J. F. Caron (2004)] 41

Figure 4.1 : Shifted Legendre Polynomial. 47
Figure 4.2 : One-dimensional element. 48
Figure 4.3 : Hierarchical structure of a stiffness matrix corresponding to polynomial degree $p = 3$. 49
Figure 4.4 : Hierarchical shape functions. 49
Figure 4.5 : "Serendipity" family 50
Figure 4.6 : "Lagrange" family 50
Figure 4.7 : Two-dimensional quadrilateral element 51
Figure 4.8 : Quadratic functions of the nodes. 51
Figure 4.9 : Quadratic functions of the sides. 52
Figure 4.10 : Quadratic internal shape function. 52
Figure 4.11 : Triangular p-element 52

Figure 5.1: FGM plate model 55
Figure 5.2 : Types of porosity distribution. 62

Figure 5.3 : Geometries of face-sheets reinforced sandwich plate: a) Uniform distribution, b) FG-CNT distribution. 64
Figure 5.4 : Geometries of core reinforced sandwich plate: a) Uniform distribution, b) FG-X distribution, c) FG-O distribution..... 64

Figure 6.1: Flowchart of the program. 70
Figure 6.2 : Numbering of nodes and sides of the p-element..... 71

Figure 7.1 : Comparative analysis of the dynamic response of simply supported square FGM sandwich plate. 85
Figure 7.2 : Effect of volume fraction exponent on the dimensionless central deflection of simply supported FG-CNTR sandwich plate (UD; a/b=1; e=0; $h_c/h_f = 2$): a) $V_{CNT}^* = 0.17$, b)$V_{CNT}^* = 0.28$ 86
Figure 7.3 : Effect of volume fraction exponent on the dynamic response of simply supported FG-CNTR sandwich plate (UD; e=0.1; a/h=10; $V_{CNT}^* = 0.12$): a)1-2-1, b)1-8-1..... 86
Figure 7.4 : Influence of CNT distribution on dimensionless central deflection of simply supported square FG-CNTR sandwich plate ($V_{CNT}^* = 0.17$): a) $1-6-1$, b) $1-8-1$ 87
Figure 7.5 : Dynamic response of the sandwich FG-CNTR reinforced plate with different CNT distributions: ($V_{CNT}^* = 0.12; a/h = 10;\ C_0 = 10\ 000$ N): a) $1-6-1$, b) $1-8-1$87
Figure 7.6 : The dimensionless central deflection of square FG-CNTR porous sandwich plate 88
Figure 7.7 : Effect of CNT models on the dimensionless central deflection of FG-CNTR 88
Figure 7.8 : Dynamic response of the sandwich FG-CNTR reinforced plate with different distribution of CNT (a/h=10; $C_0 = 8\ 000$ N): a) UD, b) FG X distribution, c) FG O distribution. 89
Figure 7.9 : Influence of core-to-face sheet thickness ratio h_c/h_f on dimensionless central deflection of simply supported square porous FG-CNTR sandwich plate (FG-X; $V_{CNT}^* = 0.17; e = 0.1$)..... 90
Figure 7.10 : Effect of core-to-face sheet thickness ratio hc/hf on the dynamic response of simply supported FGM sandwich plate (UD; $a/h = 20$; $V_{CNT}^* = 0.12$; $e = 0$)..... 90
Figure 7.11 : Influence of CNT volume fraction on the undamped response of central deflection of the simply supported square FGM sandwich plate ($a/h = 20$): $a)1-6-1, b)1-8-1$ 91

Figure 7.12 : Effect of mechanical loads on the dynamic response of the central deflection of simply supported FG-CNTR sandwich plate (UD; a/h = 10; $e = 0.1; V_{CNT}^{*} = 0.12$): $a)$ 1 − 1 − 1, $b)$1 − 2 − 1, $c)$1 − 8 − 1. 91
Figure 7.13 : Effect of damping coefficient on the dynamic response of simply supported FG-CNTR sandwich plate (a/h = 10; C_0 = 8 000 N): $a)$1 − 2 − 1, $b)$1 − 8 − 1. 92
Figure 7.14 : Influence of CNT distribution on the dimensionless central deflection of FG-CNTR sandwich plate with different porosities models (a/h = 10; $n = 2$; $e = 0.1$; $V_{CNT}^{*} = 0.17$) 92
Figure 7.15 : The dynamic behavior of simply supported FG-CNTR sandwich plate (n = 1; a/b = 1; a/h = 10): a) 1 − 8 − 1, b) 2 − 2 − 1 93
Figure 7.16 : Influence of boundary conditions on the dimensionless central deflection of square FG-CNTR (1–2–1) sandwich plate (UD; $n = 2$; $e = 0.1$; $V_{CNT}^{*} = 0.17$) 94
Figure 7.17 : The dimensionless central deflection of FG-CNTR porous sandwich plate for different configurations of plates under various boundary conditions (UD; n = 2; e = 0.1; $V_{CNT}^{*} = 0.17$) 94
Figure 7.18 : Influence of boundary conditions on the undamped response of the central deflection of square FG-CNTR sandwich plate (a/h = 10; C_0 = 10 000 N, n = 5; e = 0.1): a) UD, b) FG-O distribution, c) FG-X distribution. 95
Figure 7.19 : Influence of ratio h/a on the dynamic response of simply supported FG-CNTR sandwich plate (UD; a/b = 1): a) 1 − 2 − 1, b) 1 − 8 − 1 96
Figure 7.20 : Dynamic behavior of simply supported FG-CNTR sandwich plate with the influence of ratio a/b (UD; a/h = 10): a) 1 − 1 − 1, b) 1 − 2 − 1, c) 1 − 4 − 1. 96
Figure 7.21 : Dynamic response analysis for different models of simply supported FG-CNTR sandwich plate (a/b = 1; a/h = 10; C_0 = 10 000 N). 97
Figure 7.22 : Influence of volume fraction exponent on dimensionless central deflection of simply supported square FG-CNTR sandwich plate for the first mode (UD, a/h = 10; e=0.1; $V_{CNT}^{*} = 0.17$) 97
Figure 7.23 : Effect of coefficient of porosity on dimensionless central deflection of simply supported square FG-CNTR sandwich plate for the first mode (UD, a/h = 10; n=2; $V_{CNT}^{*} = 0.17$) 98

Figure 7.24 : Influence of CNT volume fraction on dimensionless central deflection of simply supported square FG-CNTR sandwich plate for the first mode (UD; a/h $= 10$; $e = 0.1$; $n = 2$; $h_c/h_f = 2$)..... 98

Figure 7.25 : Effect of core-to-face sheet thickness ratio h_c/h_f on dimensionless central deflection of simply supported square FG-CNTR sandwich plate for the first mode (FG-X; a/h = 10; n=2; $V_{CNT}^{*} = 0.17$) 99

List of tables

Table 2.1 : Properties of Ceramic and Metal materials 14
Table 2.2 : Types of CNTs distribution 15

Table 3.1 : Different shear functions formula 38

Table 4.1 : Comparison between -h and -p versions of FEM 45

Table 5.1 : Mechanical properties of CNTs and matrix materials 66
Table 5.2: CNT efficiency parameter 66

Table 6.1 : Node boundary conditions 72
Table 6.2 : Side boundary conditions 72

Table 7.1 : FGM sandwich plate 77
Table 7.2 : Material properties of FGM components 77
Table 7.3 : Convergence and comparison of fundamental frequencies of FGM sandwich plates with existing theories 78
Table 7.4 : Comparison of fundamental frequencies of a simply supported FGM sandwich plate with various porosity distributions ($\mathrm{a/h} = 10$, n = 2 and $\mathrm{a/b} = 1$) 79
Table 7.5 : Fundamental frequency comparison for a simply supported square sandwich plate (a/h=20, $h_c/h_f = 4$) with a homogeneous core. 80
Table 7.6 : Convergence and comparison of the nondimensional central deflection w for a simply supported perfect $\mathrm{Al/ZrO_2}$ sandwich plate with different volume fraction (a/h = 10). 81
Table 7.7 : Convergence and comparison of the nondimensional central deflection w for a simply supported porous $\mathrm{Al/ZrO_2}$ sandwich plate ($\mathrm{a/h} = 10, \mathrm{n} = 2$). 81
Table 7.8 : Convergence and comparative analysis of the dimensionless central deflection (w) for a simply supported square sandwich plates with homogeneous core and CNT reinforced face-sheets 82

List of abbreviations

FEM	Finite Element Method.
FGM	Functionally Graded Materials.
CNTs	Carbon Nanotubes.
FG-CNTR	Functionally Graded plates reinforced with carbon nanotubes.
FSDT	First-order Deformation Theory.
HSDT	Higher-order Shear Deformation Theory.
p-FEM	p-version Finite Element Method.
h-FEM	h-version Finite Element Method.
CVD	Chemical Vapor Deposition.
PVD	Physical Vapor Deposition.
P-FGM	Power-law Functionally Graded Materials.
E-FGM	Exponential-law Functionally Graded Materials.
S-FGM	Sigmoid- law Functionally Graded Materials.
VARIM	Vacuum-Assisted Resin Injection Molding.
3D	Three-Dimensional.
4D	Four-Dimensional.
SWCNT	Single-Walled Carbon Nanotube.
DWCNT	Double- Walled Carbon Nanotube.
MWCNT	Multi-Walled Carbon Nanotube.
TEM	Transmission Electron Microscope.
AFM	Atomic Force Microscope.
CPT	Classical Plate Theory.
RPT	Refined Plate Theory.
TSDT	Third-order Shear Deformation Theory.
SSDT	Sinusoidal Shear Deformation Theory.
HFEM	Hierarchical Finite Element Method.
DOFs	Degrees Of Freedom.
UD	Uniform Distribution.
FG-CNT	Functionally Graded Carbon Nanotube Distribution.
MEMS	Micro-Electro-Mechanical Systems.
NEMS	Nano-Electro-Mechanical Systems.

List of symbols

V_m	Metal volume fraction.
n_1, n_2	Volume fraction exponent.
h	Plate thickness.
V_{CNT}	Volume fraction of CNTs.
V^m	Volume fraction of matrix.
V_{CNT}^*	Specified volume fraction of CNTs.
u_0, v_0, w_0	Displacement components of the Mid-Surface.
u, v, w	Displacement field components.
θ_x, θ_y	Transverse rotations about the x and y axes.
$f(z)$	Transverse shear shape function.
w_b, w_s	Bending and shear-related components of the transverse displacement.
$P_i(\tau)$	Shifted Legendre Polynomials.
$N_i(\xi, \eta)$	Shape functions.
k	Shear correction factor.
$E^{(i)}(z)$	Young's modulus.
$\rho^{(i)}(z)$	Mass density.
$\nu^{(i)}(z)$	Poisson's ratio.
x, y	Cartesian Coordinates.
ξ, η	Local Coordinates.
t	Time.
ε_{ij}	Strain tensor.
σ_{ij}	Stress tensor.
$C_{jk}^{(i)}$	Elasticity constants.
$V^{(i)}(z)$	Volume fraction of the FGM sandwich.
T	Kinetic energy.
U	Strain energy.
L	Lagrangian function.
q_j	Vector of Generalized Transverse Displacement and Rotations
a, b	Plate length and width.
e_1, e_2	Porosity coefficient.

P_m	Material properties of the metal.
P_c	Material properties of the ceramic.
$E_{11}^{CNT}, E_{22}^{CNT}$	Young's modulus of CNTs.
G_{12}	Shear modulus of CNTs.
E^m, G^m	Young's modulus and shear modulus of the polymer matrix.
W_{CNT}	Mass fraction of CNTs.
η_1, η_2, η_3	CNT efficiency parameter.
p	Polynomial order.
A_{ij}	Extensional stiffness constants.
D_{ij}	Bending stiffness constants.
S_{ij}	Shear stiffness constants.
I_1, I_3	Inertia constants.
K_L	Stiffness matrix.
M	Mass matrix.
C_0	Mechanical load.
$\{P\}$	Load vector.
h_c	Core thickness.
h_f	Facesheets thickness.
$\overline{w}$	Dimensionless central deflection.
D_f	Flexural rigidity of the FGM plate.
I_0	Inertial coefficient of the FGM plate
Ω	Fundamental frequency parameter.
ξ	Damping coefficient.
Φ	Normalized modal matrix.

General Introduction

Due to their lightweight nature, high specific stiffness, and excellent mechanical performance, sandwich structures play a major role in advanced industrial applications, particularly in the fields of aerospace, automotive engineering, civil engineering, and biomechanics. However, limitations in terms of thermal resistance, dynamic behavior under external excitation are often encountered with conventional materials.

To address these limitations, Functionally Graded Materials (FGMs) have been introduced. These materials enable continuous variation of mechanical properties throughout their thickness, offering enhanced thermal shock resistance and smooth transitions between constituent materials. When incorporated into sandwich structures, FGMs enhance overall performance by minimizing stress concentrations and improving stability.

Furthermore, integration of Carbon Nanotubes (CNTs) as reinforcement in the core or skins of FGM sandwich plates has paved the way for a new generation of high-performance composite materials. Carbon nanotubes (CNTs) demonstrate excellent thermal conductivity, outstanding mechanical strength, and exceptional chemical stability, thereby making them particularly suited for demanding applications.

During the manufacturing processes, the intentional or unavoidable introduction of porosities is common. These porosities reduce the overall mass of the structure or tailor its vibrational behavior. However, their presence significantly affects the stiffness, mass, and consequently, the static and dynamic responses of the present structure.

This thesis focuses on the static and dynamic analysis of porous functionally graded (FG) sandwich plates reinforced with CNTs. Particular attention is paid to the influences of porosity distribution, CNT reinforcement ratio, and CNT dispersion patterns on the overall mechanical behavior. The analysis is conducted using First-order Deformation Theory, combined with robust numerical approaches such as the *p*-version of Finite Element Method (FEM) and the mode superposition technique.

Motivation and objective

This thesis focuses on both static and dynamic analysis of porous functionally graded (FG) sandwich plates reinforced with CNTs using the *p*-version of the finite element method.

The main aims of this work are:

- Analyze the combined effects of carbon nanotube (CNT) reinforcement and material porosity on the mechanical behavior of functionally graded (FGM) sandwich plates.
- Develop and implement a numerical framework using the p-version of the Finite Element Method (p-FEM) based on the First-Order Shear Deformation Theory (FSDT), allowing for a detailed investigation of static and dynamic responses.
- Examine linear free vibration characteristics of FG-CNTR sandwich plates involving different CNT distributions and porosity patterns with validation of the proposed model against reference solutions.
- Analyze the time-dependent dynamic response of the plates under using the mode superposition technique within the developed p-FEM framework. For this part two dedicated programs in FORTRAN90 have been developed:

  - ✓ An analytical solution program tailored for dynamic response of FGM plates, based on simplified assumptions.
  - ✓ A numerical program using the p-version FEM, which incorporates mode superposition method to solve the full dynamic response of porous FG-CNTR sandwich plates.

Thesis organization

This thesis is organized into seven chapters.

- **Chapter 1**, provides a comprehensive overview of previous research on the static and dynamic behavior of FGM sandwich plates, with a particular focus on different effects of porosity and carbon nanotube (CNT) reinforcement. In the first section, the free vibration behavior of FGM sandwich plates is reviewed. Next, the static and vibrational responses of porous FGM plates are examined. Subsequently, the influence of CNT reinforcement on mechanical performance of sandwich plates is discussed. Then, special attention is given to dynamic response analysis of porous FG-CNTRC plates. Finally, the last section of chapter identifies the key research gaps in literature and presents the motivations for the current study.

- **Chapter 2**, presents a summarized theoretical background essential for understanding the modeling of FG porous sandwich plates reinforced carbon nanotubes (CNTs). It begins by introducing the concept, classifications, and material property variations of Functionally Graded Materials (FGMs), combined with their practical applications. The fundamentals and advantages of sandwich composite structures are then discussed, including their components, manufacturing methods, and usage in various industries. The chapter also addresses the role of porosity, its origin, and its influence on structural performance. A brief overview of carbon allotropes and their properties is presented, followed by a detailed focus on carbon nanotubes, covering their structure, exceptional properties, synthesis techniques, and engineering applications.
- **Chapter 3**, outlines a comprehensive overview of classical and advanced theories used to model the mechanical behavior of plates, especially functionally graded and sandwich composite structures. In the first part, different plate theories that account for shear deformation are introduced. In the second part, the chapter addresses plate theories incorporating scale effects**.**
- **Chapter 4**, presents the fundamental aspects of the *p*-version of finite element method (FEM), emphasizing its historical development, key advantages, and limitations. A comparison with the classical h-version highlights the p-version's superior accuracy for smooth solutions. It also introduces mesh adaptation strategies used in p-FEM and provides a comprehensive discussion on the numerical implementation.
- **Chapter 5**, provides the finite element formulation of FGM sandwich plates based on First-order Shear Deformation Theory (FSDT)**.** It begins by introducing the FGM sandwich plate model. Then, the associated theoretical formulation is presented**.** The next section describes the numerical modeling using rectangular p-elements**,** focusing on the approximation of displacement fields through hierarchical shape functions**,** and the computation of element mass and stiffness matrices required for solving the governing equations. In the last, the foundational data and mathematical relations necessary for integrating porosity and CNT effects into the finite element analysis of sandwich structures model are presented. The objective in the first part is to investigate five types of porosity-dependent FGM configurations. For the second part, it describes the effective material properties of CNTs.
- **Chapter 6**, details the computational environment, software, hardware used and programming methods to implement the p-version finite element model for porous FGM sandwich plates reinforced CNTs.

- **Chapter 7**, presents the numerical investigation of static and dynamic behavior of FGM sandwich plates with porosity and a core reinforced by carbon nanotubes (CNTs). First, a numerical procedure has been developed to calculate the central deflection of plate. Then, a convergence study and model validation are conducted by comparing the numerical results with published data. In the next, a dynamic analysis of porous FGM sandwich plates with a CNT reinforced core using two methods: an analytical solution for FGM plates and numerical solution derived from the *p*-version FEM with mode superposition is presented. After validating the FEM results, a detailed parametric study is performed to investigate the effect of different parameters on both static and time-dependent dynamic responses.

This thesis finishes with general conclusion listing the principal findings of this study carried out and briefly outlines potential future work.

Chapter 1 Literature Review

Objective

Chapter 1 is dedicated to a comprehensive literature review, providing a state-of-the-art survey of various research domains that form foundation of the studies presented in this thesis.

First, a general history of free vibration of FGM sandwich plate. In the second part, a rich review of the free vibration and static analysis of porous FGM sandwich plate. This is followed by a summary of the work found in the literature on the free vibration and static analysis of FGM sandwich plate reinforced CNTs. In the fourth part, a general overview of the research carried out on dynamic analysis of porous sandwich FG-CNTRC plate. Finally, the research gaps and motivation of the present work are discussed.

1.1. Free vibration of FGM sandwich plate

The free vibration of functionally graded sandwich plates (FGMs) has attracted increasing attention due to their capability to combine lightweight characteristics of sandwich structures with spatially varying mechanical properties through the thickness. This combination results in vibration behaviors with tunable performance tailored to specific applications. Li et al. (2008) conducted a three-dimensional (3D) vibration analysis of functionally graded sandwich plates with both simply supported and clamped boundary conditions. Mahi et al. (2015) proposed novel Hyperbolic Shear Deformation Theory (HSDT) to analyze the free vibration and bending behavior of isotropic, sandwich, laminated composite and functionally graded plate. Kiani et al. (2012) studied the instability behavior of (FG) sandwich plates under coupled mechanical and thermal loads while resting on two-parameter elastic foundation. Additionally, a QUAD-8 Shear-flexible Finite Element, combined with a Higher-order Structural Theory, was employed to examine the vibration and bending responses of sandwich FG plates [Natarajan et Manickam (2012)]. Mohammadi et Khalili (2012) employed an analytical approach to investigate the free vibration of simply supported FG sandwich plates subjected to various thermal loading conditions. Dozio (2013) proposed an advanced two-dimensional Ritz-based formulation for the vibration analysis of sandwich plates with functionally graded cores. Xiang et al. (2013) conducted a vibration analysis of FG sandwich plates using a meshless global collocation method. Loja et al. (2013) developed B-spline finite strip element models to investigate the static behavior and free vibration of FG sandwich plates integrated with piezoelectric face layers. Pandey et Pradyumna (2015a) performed an investigation into the free vibration behavior of FG sandwich plates subjected to thermal environments using Finite Element Method (FEM). In a subsequent study [Pandey et Pradyumna (2015b)], they adopted a layer-wise finite element formulation to analyze the vibration response of FG sandwich plates under nonlinear thermal loads, accounting for thermo-dependent material properties. According to First-order Shear Deformation Theory (FSDT), Nguyen et al. (2014) investigated the buckling and vibration behavior of FG sandwich plates by incorporating advanced transverse shear stiffness formulation. In another study, Dat et al. (2016) employed the Finite Element Method (FEM) using Third-order Shear Deformation Theory (TSDT) to analyze FG sandwich plates reinforced incorporating stiffeners. Fazzolari (2015) conducted an investigation into the thermal stability and free vibration behavior of FG sandwich plates under thermal loading. Alibeigloo et Alizadeh (2015) employed Three-dimensional Theory of elasticity in conjunction with Differential Quadrature Method (DQM) to investigate the free vibration and bending responses

of FG sandwich plates. Tossapanon et Wattanasakulpong (2020) applied the Chebyshev collocation method along with the First-order Shear Deformation Theory (FSDT) to examine the flexural response of FG sandwich plates on combined Winkler and Pasternak elastic foundations. Liu et al. (2018) adopted Higher-order Shear Deformation Theory (HSDT) combined with mixed layer-wise approach to investigate the free vibration behavior of sandwich plates with non-monotonic flexible core properties. Based on Von Kármán's nonlinear hypotheses, Belalia (2019) developed a geometrically nonlinear formulation to analyze the free vibration of FG sandwich plates. The *p*-version of Finite Element Method (FEM) was employed to study nonlinear vibration of bi-FG material sandwich plates, accounting for the influence of transverse shear deformation and rotary inertia [Belalia (2017)]. Burlayenko et Sadowski (2020) developed a comprehensive three-dimensional modeling approach to study free vibration and static responses of sandwich FGM plates. Their methodology employed Finite Element Method implemented within the ABAQUS™ software environment, utilizing a three-dimensional graded brick finite element to accurately capture the material gradation and structural behavior. Vu et al. (2023) introduced novel Refined Arctangent Exponential Shear Deformation Theory (RAESDT) for the analysis of isotropic and FGM sandwich plates with power-law material gradation. This theory inherently satisfies the traction-free boundary conditions and reduces computational cost. It is coupled with an improved Moving Kriging Interpolation (MKI) meshfree method. Furthermore, Vu et al. (2021) proposed new four-variable Quasi-3D Logarithmic Shear Deformation Theory, also combined with an enhanced MKI meshfree method for investigating the static bending, free vibration, and buckling analysis of FG plates resting on elastic foundations. Van Vinh (2023) proposed a Hybrid Quasi-3D Shear Deformation Theory that integrates both polynomial and trigonometric functions to effectively represent the transverse shear strain distribution and account for thickness stretching effects in functionally graded sandwich plates. (Ghazwani 2024) developed an nth-order Shear Deformation Theory aimed at simplifying structural analysis of FGM sandwich plates by introducing a formulation involving only four displacement variables.

1.2. Free vibration and static analysis of porous FGM sandwich plate

The presence of porosity results in a decrease in structural stiffness. These porosities may either arise inherently during the manufacturing process or be intentionally introduced to tailor the mechanical characteristics of structural element according to specific performance requirements [Saleh et al. (2020)]. Various theories have been introduced in the literature to analyze the bending and vibration behaviors of FGM sandwich plates incorporating porosities.

Zhou et al. (2018) conducted a thermo-mechanical vibration analysis of porous functionally graded (FG) plates using the First-order Shear Deformation Theory (FSDT). Zhang et al. (2020) employed Fourier-Ritz method based on the FSDT to analyze the free vibration and damping behavior of porous FGM sandwich plates with viscoelastic cores. Daikh et Zenkour (2019a) developed a novel higher-order shear deformation theory (HSDT) to investigate the bending, free vibration, and buckling behaviors of simply supported porous FGM sandwich plates governed by power-law and sigmoidal material distributions. Zenkour (2018) proposed a Quasi-3D Higher-order Shear Deformation Theory (HSDT) for bending analysis of thick rectangular plates made of single-layered and sandwich functionally graded materials (FGMs). Singh et Harsha (2020) introduced a non-polynomial Shear Deformation Theory (SDT) formulated using the Galerkin–Vlasov approach to investigate the thermo-mechanical bending behavior of porous FGM sigmoidal sandwich plates. Liang et Wang (2020) proposed a Quasi-3D Trigonometric Shear Deformation Theory to investigate wave propagation in porous FGM sandwich plates resting on a viscoelastic foundation. Adhikari et al. (2020) investigated the influence of different porosity types on the buckling behavior of various FGM sandwich plate configurations using the HSDT. Tahir et al. (2021) employed simplified hyperbolic HSDT to explore wave propagation in porous FGM sandwich plates subjected to various porosity models and hygro-thermal environments. Meanwhile, Van Vinh et Huy (2022) conducted a Finite Element analysis based on novel a hyperbolic shear deformation theory adopted to examine bending, free vibration, and buckling behaviors of FGM sandwich plates with different porosity patterns. Demirhan et Taskin (2019) investigated the flexural behavior and natural vibration characteristics of functionally graded plates, highlighting the effect of porosity distribution on effective material properties and structural behavior, particularly with respect to thickness effects. Kumar Sah et Ghosh (2022) conducted free vibration and buckling of multidirectional porous FG sandwich plates, highlighting influence of porosity orientation and distribution on the structural response. Bentrar et al. (2023) employed the *p*-version Finite Element Method combined with the FSDT to analyze the free vibration of FGM sandwich plates with spatially varying porosity in the face sheets. Belarbi et al. (2022) analyzed the bending and free vibration behavior of porous FG sandwich plates for various porosity distribution models within the framework of an extended layer-wise theory. Belkhodja et al. (2023) conducted comprehensive investigation of thermal buckling and thermo-mechanical bending behavior of sandwich plates with FGM face sheets, considering the effect of thermal loading and porosity distributions on structural response of plates. Lakhdar et al. (2024) investigated the free vibration and bending responses of bi-directional porous FGM sandwich shells using the Third-Order Shear

Deformation Theory (TSDT). The analysis was conducted within *p*-version finite element framework, allowing for enhanced accuracy in capturing the complex through-thickness gradation and porosity effects. Vu et Cao (2023) proposed a hyperbolic quasi-3D shear deformation theory to analyze the static behavior and natural frequency response of FG porous plates resting on elastic foundations. Their model effectively captures both shear strain and normal deformation using only four displacement variables, avoiding the use of shear correction factors, and thereby improving computational efficiency without compromising accuracy.

1.3. Free vibration and static analysis of FGM sandwich plate reinforced with CNTs

The remarkable attributes of advanced functionally graded carbon nanotube-reinforced (FG-CNTR) sandwich plates including their lightweight structure, exceptional thermal resistance, and superior mechanical and chemical performance have garnered increasing attention from researchers. Kiani (2017) employed the FSDT in combination within the framework of Donnell's shell theory to analyze vibrational behavior of carbon nanotube-reinforced composite conical panels embedded in a polymer matrix, emphasizing the effects of CNT distribution patterns and volume fraction on their dynamic response. Lei et al. (2016) investigated the free vibration characteristics of functionally graded carbon nanotube-reinforced thick quadrilateral plates with straight sides resting on a Pasternak-type elastic foundation, employing Improved Moving Least Squares (IMLS)-Ritz method. Zhu et al. (2012) conducted an analysis of static and free vibration responses of carbon nanotube-reinforced plates within the framework of FSDT. The study considered a polymer matrix reinforced with carbon nanotubes (CNTs), without accounting for thermal effects. The results indicated that CNT volume fraction plays significant role in influencing both fundamental vibration frequency and maximum central deflection of the plate. Natarajan et al. (2014) employed a Higher-order Structural Theory to investigate the bending behavior and free vibration response of sandwich plates featuring carbon nanotube-reinforced composite face sheets. Singh et Sahoo (2021) provided an analytical solution to assess both the static behavior along with natural vibration characteristics of FG-CNT reinforced sandwich plates.

1.4. Dynamic analysis of porous sandwich FG-CNTRC plate

The dynamic response of functionally graded sandwich plates is essential for understanding their behavior under time-dependent service loading conditions, particularly in the aerospace field, automotive, and mechanical applications where impact and vibration resistance are critical. Hajmohammad et al. (2019) developed dynamic response model for auxetic

honeycomb sandwich plates with reinforced face sheets containing agglomerated carbon nanotubes (CNTs), subjected to explosive loading. The analysis employed a viscoelastic sinusoidal formulation. Medani et al. (2019) investigated both static and dynamic behaviors of FG-CNT reinforced porous polymer sandwich plates by employing the FSDT. Dat et al. (2022) performed nonlinear dynamic and vibration study of sandwich plates made of FG-CNTRC materials, which incorporated a core layer containing pores, through the application of Hamilton's variational principle, TSDT, and Galerkin approach combined with fourth-order Runge-Kutta method. Rai et Gupta (2024) studied dynamic response of FG sandwich nanoplates under thermal environments and supported by elastic foundations through the Dynamic Stiffness Method (DSM).

1.5. Research gaps and motivation of the current work

The originality of the present research lies in advanced computational modeling and systematic analysis of static and dynamic responses of porous functionally graded carbon nanotube-reinforced (FG-CNTR) sandwich plates. The structure under investigation consists of top and bottom face sheets made of FGMs incorporating five distinct porosity profiles, and a CNT-reinforced core layer characterized by three different CNT dispersion patterns (uniform, FG-X, and FG-O models). This level of material modeling complexity remains scarcely explored in the current literature.

To address the challenges associated with such heterogeneous and multilayered systems, the *p*-version Finite Element Method (*p*-FEM) is adopted based on First-order Shear Deformation Theory (FSDT), allowing high-accuracy approximation using a minimal overall degree of freedom. The dynamic response of structure is studied via the mode superposition technique, and analytical solution is developed in parallel to verify numerical implementation.

This study also carries out a detailed parametric investigation. According to the authors' knowledge, this is the first research to combine such an in-depth multiparameter static and dynamic analyses with the p-FEM formulation for porous FG-CNTR sandwich plates. The findings are of particular interest for high-performance structural components used in aerospace, automotive, and microelectromechanical systems, where tailored mechanical response, weight reduction, and thermal stability are critical design requirements.

Chapter 2 Theoretical background and material modeling

Objective

The aim of this chapter is to provide more details on the fundamental theoretical framework necessary for modeling functionally graded porous sandwich plates reinforced with carbon nanotubes (CNTs). This chapter is organized into several parts. The first part, an *overview of functionally graded materials (FGMs), including their fundamental concept, classification into various types, their material property gradation models and a summary of their industrial applications. Sandwich composite structure and porosity in sandwich plates are given in the second and the third part, respectively. The description of Carbon element, their specific characteristics are discussed in the fourth part. The last part is focused to Carbon nanotube, their properties are first introduced, followed by an in-depth examination, including their structural configuration, outstanding characteristics, synthesis methods, and diverse engineering applications.*

2.1. Functionally Graded Materials (FGM)

2.1.1. Introduction to functionally graded materials

2.1.1.1 FGM definition and concept

Functionally Graded Materials (FGMs) are a class of advanced composite materials engineered with a continuous and spatially varying distribution of their constituent phases. This gradual variation in composition and microstructure across material volume results in smooth transitions in mechanical, thermal, and physical properties, typically along the thickness direction. Such gradation is intentionally designed to meet specific performance criteria such as elevated thermal stability, enhanced load-bearing capacity, or improved damage tolerance while mitigating stress discontinuities and interfacial weaknesses typically observed in conventional layered composites.

Several FGMs are manufactured by combining two material phases with different properties. A detailed description of the actual graded microstructure is generally unavailable, except perhaps for information related to the volume fraction distribution.

While the phase volume fraction varies gradually along the grading direction, the effective properties of the FGM also change along this direction. Accordingly, two modeling approaches are typically considered for FGMs:

- In the **first approach**, a piecewise variation of the volume fraction of ceramic or metal is assumed. The FGM is modeled as being composed of layers with constant volume fraction in each region, i.e., quasi-homogeneous ceramic-metal layers (figure 2.1-a).
- In the **second approach**, continuous variation of the ceramic or metal volume fraction is assumed (figure 2.1-b), and the metal volume fraction can be represented in terms of coordinate along the thickness direction (z).

$$V_m = \left(\frac{2z + h}{2h}\right)^n \tag{2.1}$$

Where h represent the thickness of plate and, n $(0 < n < \infty)$ refers to the volume fraction exponent of the material profile through the thickness of FGM layer. As can be seen in Figure 2.2, changing the value of *n* generates an infinite number of composition distributions

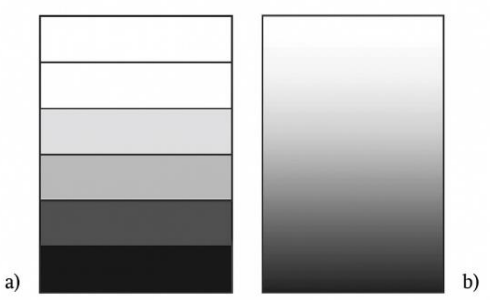


Figure 2.1: Analytical model for a FGM layer: a) First approach b) Second approach

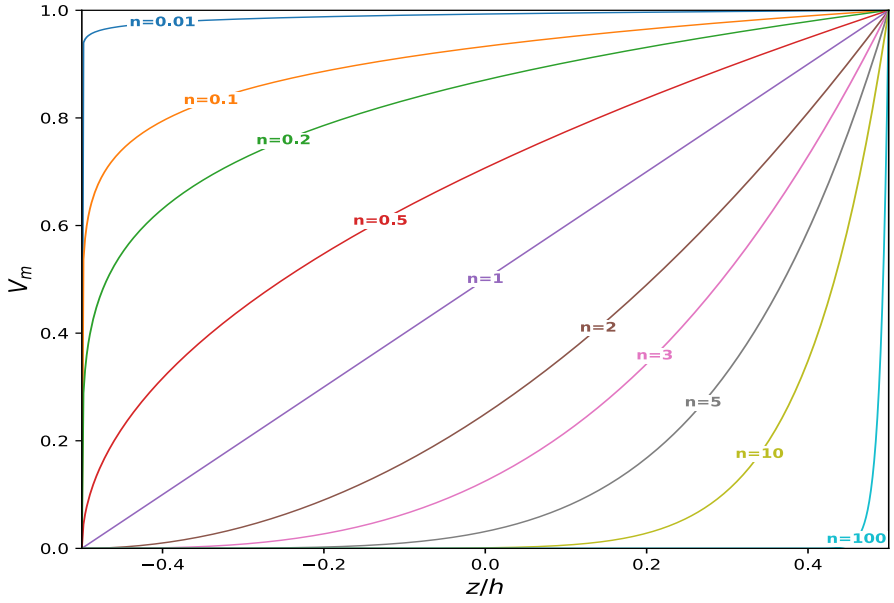


Figure 2.2: Volume fraction of metal along the thickness

2.1.1.2 FGM history and evolution [Koizumi (1997)]

Functionally Graded Materials (FGMs) were first introduced by Japan in 1984 as part of a spaceplane project. The goal aimed to develop a thermal barrier coating capable of withstanding extreme surface temperatures of up to 2000 K while maintaining with a temperature variation of 1000 K over a 10 mm thickness. This was achieved by engineering gradual transition in composition from ceramic (heat-resistant) surface to metallic substrate thereby minimizing thermal stresses and improving durability.

In 1987, Japan launched a national R&D program focused on FGMs, primarily for aerospace and thermal protection systems. In 1992, FGMs have been acknowledged as one of Japan's top ten advanced technologies, highlighting their strategic importance.

Since the early 2000, FGM research has expanded globally, with significant contributions from Europe. In Germany, breakthroughs were made in thermomechanical coupled fabrication techniques for graded monomaterials like steel and aluminum. Advanced manufacturing methods, including :

- Powder metallurgy
- Chemical/physical vapor deposition (CVD/PVD)
- Electrodeposition methods (EPD)
- Thermal spray method
- Solid state methods
- Liquid state methods
- Centrifugal casting
- Additive manufacturing (3D printing)

Have enabled precise control of compositional gradients.

2.1.2. Classification and types of FGM material

2.1.2.1 FGM on ceramic and metal base

A metal-ceramic functionally graded material (FGM), is a class of advanced composites featuring a continuous spatial gradation showing a gradation from a ceramic-rich phase to metal-rich phase across the thickness or volume. This gradation is engineered to effectively combine the superior thermal resistance and hardness of ceramics with the ductility and fracture toughness of metals as shown in table 2.1.

Table 2.1 : Properties of Ceramic and Metal materials

Property	**Ceramic**	**Metal**
Hardness	High	Moderate
Thermal resistance	Excellent	Moderate to Good
Fracture toughness	Low	High
Electrical conductivity	Insulator	Conductor
Machinability	Difficult	Easier

Ceramic-metal FGM smoothly bridges these properties to achieve thermal stress resistance, wear resistance, and structural reliability in extreme environments.

2.1.2.2 Porous FGM

Porous Functionally Graded Materials (FGMs) are advanced heterogeneous structures in which not only the material composition but also the porosity varies gradually across one or more spatial directions. The introduction of porosity aims to reduce structural weight, enhance energy absorption, and improve thermal insulation and biological integration in specific applications. In particular, the gradual porosity distribution helps to avoid abrupt changes in mechanical properties, which can lead to stress concentrations and failure.

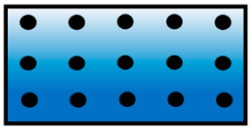
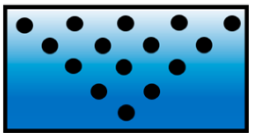
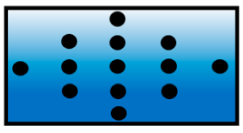
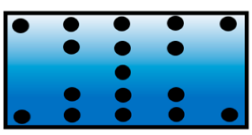
Porous FGMs have attracted significant interest in various engineering and biomedical fields, including lightweight aerospace components, thermal barrier coatings, and orthopedic implants. In biomedical applications, for instance, the presence of graded porosity enhances osseointegration and promotes nutrient transport, while maintaining mechanical compatibility with surrounding bone tissues.

2.1.2.3 CNT-Reinforced Functionally Graded Materials

Functionally Graded Materials (FGMs) reinforced with carbon nanotubes (CNTs), known as FG-CNT composites, combine the advantages of continuous material gradation with the exceptional mechanical, thermal, and electrical properties of CNTs. In these advanced composites, the volume fraction of CNTs is distributed non-uniformly through the thickness, often following power-law, exponential, or sigmoid profiles.

Table 2.2 summarizes the principal types of carbon nanotube (CNT) distributions used in functionally graded CNT-reinforced composites, including their mathematical formulations, physical descriptions, and schematic representations through the thickness direction Ansari et al. (2018).

Table 2.2 : Types of CNTs distribution

Type	Formula	Description	Schema
UD	$V_{CNT} = V_{CNT}^{*}$	CNTs are uniformly distributed throughout the thickness.	
FG-V	$V_{CNT} = \left(1 + \frac{2\lvert z\rvert}{h}\right) V_{CNT}^{*}$	CNTs are localized near the top surface and decrease towards the bottom.	
FG-O	$V_{CNT} = 2\left(1 - \frac{2\lvert z\rvert}{h}\right) V_{CNT}^{*}$	CNTs are concentrated in the center of the plate and reduce toward the outer surfaces in a symmetric manner	
FG-X	$V_{CNT} = 2\left(\frac{2\lvert z\rvert}{h}\right) V_{CNT}^{*}$	CNTs are concentrated on both the top and bottom surfaces, low in the core.	

2.1.3. Material properties of FGM

The material properties of FGMs are typically modeled as continuous functions varying along the thickness of the material. Three common laws describe this variation:

2.1.3.1 Power-law(P-FGM)

The property $P(z)$ at a position z through the thickness h is given by [Bao et Wang (1995)]:

$$P(z) = P_2 + (P_1 + P_2)\left(\frac{1}{2} + \frac{z}{h}\right)^n \tag{2.2}$$

P_2 and P_1 are the properties at top and bottom surfaces, respectively. n is the power-law index (the volume fraction exponent) controlling the gradation profile

When $n = 0$, the material is fully ceramic (top surface). Increasing n shifts the property distribution towards the bottom material (usually metal).

2.1.3.2 Exponential-law(E-FGM)

In the exponential law, the property variation is modeled as [Karami et al. (2019)] :

$$P(z) = P_2\, e^{\frac{1}{h}\left(ln\frac{P_1}{P_2}\right)\left(z+\frac{h}{2}\right)} \tag{2.3}$$

The effective mass density ρ was evaluated through the application of the rule of mixtures, regardless of micromechanical model adopted. According to Delale et Erdogan (1983), the influence of Poisson's ratio on the deformation behavior is considerably less significant compared to that of Young's modulus. Therefore, Poisson's ratio was considered to remain constant throughout FGM plate.

2.1.3.3 Sigmoid law(S-FGM)

The sigmoid law provides a smooth S-shaped variation of properties [Chi et Chung (2003)]

$$P(z) = P_2 + (P_1 - P_2)\left(1 - \frac{1}{2}\left(\frac{h/2 - z}{h/2}\right)^n\right) \text{ For } 0 \le z \le \frac{h}{2} \tag{2.4}$$

$$P(z) = P_2 + (P_1 - P_2)\left(\frac{1}{2}\left(\frac{h/2 + z}{h/2}\right)^n\right) \quad \text{For } -\frac{h}{2} \le z \le 0 \tag{2.5}$$

2.1.4. Industrial applications of FGM

The various industrial applications of Functionally Graded Materials (FGMs) are summarized below, highlighting their multifunctional use across different sectors such as:

- **Aerospace Sector** [Saleh et al. (2020)]

FGMs are employed in thermal barrier coatings, rocket nozzles, heat shields, and turbine engine parts thanks to their ability to withstand extreme temperatures and oxidation. Their

excellent thermal and mechanical stability makes them essential for high-performance aerospace systems.

- **Biomedical Sector** [Matsuo et al. (2001), Watari et al. (2004), Sadollah et al. (2013)]

In medical applications, FGMs serve in orthopedic and dental implants with graded stiffness and bone-like behavior, ensuring better load transfer and enhanced biocompatibility. These features improve implant integration and long-term durability.

- **Energy Sector** [Niino et al. (2005)]

FGMs contribute to thermal insulation systems in nuclear reactors, fuel cells, and thermoelectric converters. Their capacity to endure severe thermal gradients enhances energy efficiency and operational reliability in high-temperature environments.

- **Electronics Sector** [Mahamood et Akinlabi (2017)]

They are used as substrates and interconnects with tailored thermal expansion coefficients in microelectronic and heat dissipation systems. This ensures thermal compatibility and increases the performance and reliability of advanced electronic devices.

- **Defense Sector** [Chen et al. (2007)]

FGMs are incorporated into impact-resistant armors, laser protection coatings, and shock-absorbing structures. Their combination of high strength, low weight, and energy absorption capability offers superior protection in extreme conditions.

- **Automotive Sector** [Saleh et al. (2020)]

In automotive engineering, FGMs are found in brake discs, pistons, and engine components, providing graded wear resistance and heat tolerance. These properties improve braking performance, thermal stability, and the service life of parts.

- **Civil Engineering Sector** [Herrmann et Sobek (2017)]

FGMs are integrated into smart structures and vibration-damping systems for bridges and buildings. Their adaptability to dynamic and seismic loads enhances both safety and long-term structural integrity.

- **Tooling Sector** [Mahamood et Akinlabi (2017)]

They are used in cutting tools and forming dies with graded hardness and thermal shock resistance. This ensures superior wear resistance and performance in high-speed machining and precision manufacturing.

- **Marine Sector** [Mahamood et Akinlabi (2017)]

FGMs are applied in corrosion-resistant coatings and hull elements exposed to thermal and mechanical gradients. Their high resistance to seawater corrosion improves the durability and reliability of marine structures.

2.2. Sandwich composite structure

2.2.1. Definition and fundamental principles

A sandwich structure is a type of layered composite material consisting of two high-strength, stiff face sheets bonded to a lightweight, thick core. This architecture provides an excellent strength- and stiffness-to-weight ratio, rendering it highly effective for applications requiring optimized structural performance with minimized mass [Marshall (1982)]. The sandwich structure behaves like a beam with separated flanges. Under bending, the upper face sheet carries compressive stresses while the lower one carries tensile stresses; the core transmits shear between them. This synergy provides high flexural rigidity with minimal weight [Daniel et Ishai (2006)].

2.2.2. Advantages of sandwich structures

Sandwich structures offer a distinctive combination of mechanical and functional advantages, which makes them highly applicable for advanced engineering applications where weight reduction, strength, and energy efficiency are paramount. Their primary benefits include:

- **Superior weight-normalized strength and stiffness**

By separating stiff face sheets with a lightweight core, the bending stiffness of panel is significantly increased without substantially adding mass. This configuration enables sandwich panels to carry high loads while maintaining low weight, a critical requirement in aerospace, automotive, and other weight-sensitive industries.

- **Enhanced energy absorption**

The core material commonly foams or honeycomb provides excellent energy absorption capabilities under impact or crash scenarios. This characteristic makes sandwich structures ideal for applications demanding crashworthiness, such as vehicle safety components and protective aerospace or defense structures.

- **Resistance to local buckling**

The supportive core stabilizes the face sheets, effectively delaying or preventing local buckling that could otherwise undermine structural integrity. This stabilization allows the use of thinner face sheets without compromising overall performance, optimizing material usage.

- **Thermal and acoustic insulation**

Depending on the core composition, sandwich panels can deliver superior thermal insulation due to low thermal conductivity, as well as effective sound damping. These

properties are especially valuable in aircraft cabins, building envelopes, and energy-efficient transportation systems.

- **Damage tolerance and multi-layer protection**

The multi-layered nature of sandwich structures enables localized damage containment such as from impacts or fatigue without immediate catastrophic failure. This inherent redundancy enhances durability and reliability in demanding operational environments.

2.2.3. Composition of a Sandwich Structure

A sandwich structure is composed of three primary components:

2.2.3.1 Face sheets(skins)

The face sheets, also referred to as skins**,** constitute the outermost layers of a sandwich structure and are primarily responsible for providing high strength and bending stiffness. These layers are typically fabricated from high-performance materials such as:

- **Fiber-reinforced composites** (e.g., carbon fiber, glass fiber, Kevlar®)
- **Lightweight metals** (e.g., aluminum, titanium, steel)
- **Hybrid composites** combining different fibers or matrix systems

These face sheets bear the majority of the tensile and compressive stresses generated during bending and serve to shield the core from mechanical and environmental damage. Although relatively thin compared to the core, they are critical for mechanical integrity and performance of sandwich system.

Material selection for face sheets is guided by specific application requirements such as mechanical strength, durability, stiffness-to-weight ratio, corrosion resistance, and cost efficiency. For instance, carbon fiber or graphite-epoxy laminates are commonly used in aerospace because to their exceptional mechanical properties and low density, whereas fiberglass composites or aluminum may be favored in marine and civil structures for their corrosion resistance and affordability.

Face sheets can be manufactured as laminated composites with woven or unidirectional fibers embedded in polymer matrices, or as thin metallic sheets. These are bonded to the core either through structural adhesives or co-curing techniques in composite fabrication

2.2.3.2 Core

The core material in a sandwich structure is a lightweight, thick layer placed between the two face sheets to provide high bending stiffness and reduce overall density. Although the core usually has relatively low strength compared to the face sheets, its thickness significantly enhances the structural rigidity and shear resistance of the sandwich panel.

Different type of cores used in sandwich structures [Kausar et al. (2023)] are presented in figure 2.3.

- **Homogeneous Core Materials**

These are uniform-density materials used primarily for lightweight filling and basic structural support:

- ✓ Wood Cores

Examples : Balsa, plywood

Properties: Natural, low-cost, moderate strength-to-weight ratio.

Applications : Marine hulls, vintage aircraft wings.

- ✓ Foam Cores

Examples: PVC foam, polyurethane foam, syntactic foam.

Properties: Ultra-lightweight, excellent thermal/ acoustic insulation.

Applications: Surfboards, wind turbine blades, sandwich panels.

- **Structured Core Materials**

These features engineered cellular architectures for high strength and specialized functions:

- ✓ Honeycomb Cores

Materials: Aluminum, Nomex, thermoplastic.

Structure: Hexagonal cells mimicking bee honeycombs.

Advantages: Exceptional stiffness-to-weight ratio, impact resistance.

Uses: Aircraft floors, spacecraft panels, Formula 1 cars.

- ✓ Corrugated Cores

Design: Wave-like or triangular patterns.

Benefits: High shear strength, energy absorption.

Applications: Shipping containers, architectural cladding.

- ✓ Textile Cores

Types : 3D woven fabrics, spacer textiles.

Features : Flexibility, customizable porosity.

Examples : Composite reinforcements, medical implants.

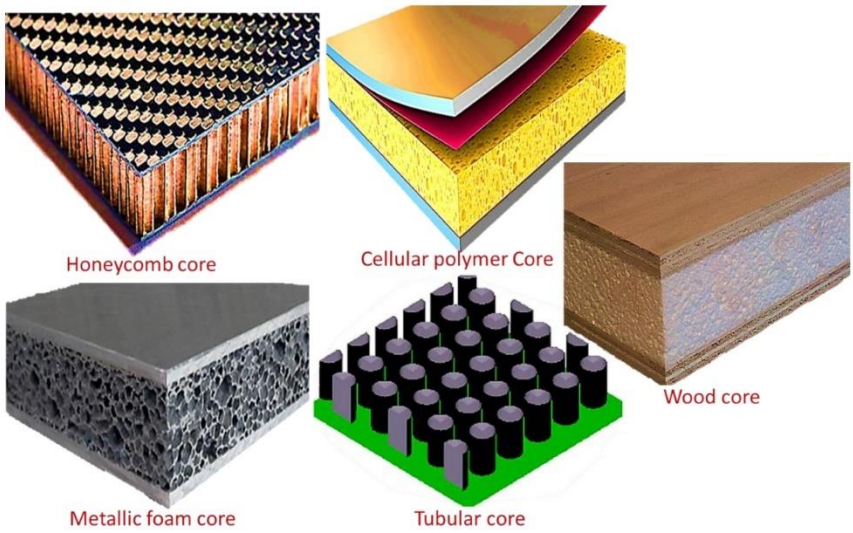


Figure 2.3 : Different sandwich core types [Kausar et al. (2023)].

2.2.3.3 Adhesives and interfaces

The adhesive layer in sandwich structures plays a critical role in bonding the face sheets (skins) to the core, ensuring effective load transfer and maintaining structural integrity. Because shear stresses change rapidly at the core–face sheet interface, the adhesive must withstand significant shear forces to prevent delamination. Adhesives must have high strength, durability, and resistance to environmental factors such as moisture, temperature fluctuations, UV exposure, and chemicals. They should also accommodate differences in thermal expansion between core and face sheets. Several types of adhesives are used in sandwich structures such as:

- **Epoxy Adhesives**

Epoxy adhesives are frequently applied in sandwich panel constructions owing to their superior mechanical strength, long-term durability, and robust environmental resistance. Their versatility allows effective bonding between dissimilar materials, making them ideal for demanding structural applications [Adhi et al. (2024), Pereira et Fernandes (2019)].

- **Polyurethane Adhesives**

These adhesives provide an optimal balance between mechanical strength and flexibility, making them well-suited for sandwich structures requiring limited deformability. They also exhibit reliable resistance to moisture ingress and thermal variations.

- **Modified Acrylics**

Characterized by their rapid curing capabilities and versatility in bonding dissimilar materials, these adhesives are commonly employed in applications demanding quick assembly and high production efficiency.

- **Film Adhesives**

These adhesives are supplied in film form and are primarily used to promote reliable bonding between the core and prepreg layers in sandwich structures. They are especially effective in achieving uniform adhesion within cellular core architectures.

2.2.4. Sandwich structure applications

The diverse industrial applications of sandwich structures are summarized below, highlighting their versatility in demanding engineering fields.

- **Aerospace**

FGMs find extensive applications in aerospace engineering for aircraft wings, fuselage panels, thermal insulation layers, and engine nacelles. Their high strength-to-weight ratio and capacity to withstand extreme temperature gradients make them ideal for heat shields and satellite panels. These materials contribute significantly to fuel efficiency and structural integrity.

- **Automotive**

In the automotive sector, FGMs are employed in car body panels, bumpers, battery casings for electric vehicles, dashboards, and crash energy absorbers. Their high impact resistance and vibration damping capabilities improve passenger safety while reducing overall vehicle weight, leading to enhanced performance and energy efficiency.

- **Marine**

Marine applications include the fabrication of boat hulls, decks, and offshore structures. The corrosion resistance and mechanical durability of FGMs under harsh marine environments ensure longer service life and reduced maintenance costs.

- **Civil Engineering**

FGMs are increasingly used in infrastructure components such as bridge decks, façade panels, and prefabricated wall systems. Their ability to tailor mechanical and thermal properties enhances structural performance and durability, especially under variable environmental conditions.

- **Defense**

In defense applications, FGMs serve in lightweight ballistic armor, protective shields, and high-impact-resistant panels. Their graded structure efficiently dissipates impact energy, providing superior protection without excessive weight.

- **Energy**

FGMs play a crucial role in renewable and nuclear energy systems. They are used in wind turbine blades, thermal barrier coatings, and heat-resistant components for nuclear reactors. Their ability to withstand high temperatures and thermal stresses improves the efficiency and safety of energy conversion systems.

- **Electronics**

In the electronics industry, FGMs are employed for lightweight casings, heat sinks, and substrates with excellent thermal conductivity. Their controlled gradation minimizes thermal mismatch and enhances device reliability.

- **Sports and Leisure**

Due to their combination of stiffness, low weight, and vibration absorption, FGMs are used in high-performance sports equipment such as bicycle frames, skis, surfboards, helmets, and racing boats, providing improved comfort and mechanical response.

- **Biomedical**

In biomedical engineering, FGMs are applied to prosthetic devices and orthopedic implants. Their composition can be designed to achieve the mechanical properties of natural bone, promoting better biocompatibility and reducing stress shielding effects.

2.3. Porosity in Sandwich Plates

A porous plate is a specialized component commonly used in Earth and Planetary Sciences to facilitate controlled fluid desaturation. It functions by establishing a pressure gradient across the plate, enabling the displacement of fluids within the tested samples.

2.3.1. Porosity definition and origin

Porosity refers to the presence of voids or pores within a material. In sandwich plates, porosity can arise either intentionally (engineered porosity for weight reduction or functionality) or unintentionally (due to manufacturing defects such as improper curing, incomplete resin infiltration, or gas entrapment).

In engineered porous cores, such as metal or polymeric foams, porosity is deliberately introduced to reduce density and increase specific strength. Conversely, random or non-uniform porosity due to fabrication errors can weaken structural performance [Jang et al. (2023)].

2.3.2. Effects of porosity on structure properties

Porosity significantly affects the mechanical behavior of sandwich structures:

- **Reduction in strength and stiffness**: Pores act as stress concentrators, weakening the core and interfacial bonding [Swaminathan et al. (2023)].

- **Degradation of fatigue and impact resistance**: Increased porosity leads to earlier initiation of cracks and reduced energy absorption under dynamic loading [Tammas-Williams et al. (2017)].
- **Thermal insulation and acoustic damping**: On the positive side, controlled porosity in cores can enhance thermal and acoustic properties[Zhang et al. (2023)].

Numerical and experimental investigations show that the type, size, and distribution of pores critically affect bending stiffness and natural frequencies.

2.4. Carbon

2.4.1. Electronic structure

Carbon, with atomic number 6, has an electronic structure of $1s^2 2s^2 2p^2$. This means that in the first energy level (shell), there are two electrons in the 1s orbital. The second energy level (shell) has two electrons in the 2s orbital and two electrons in the 2p orbitals. These four electrons in the outermost shell are called valence electrons, which are important for chemical bonding.

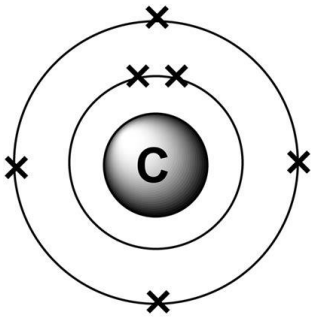


Figure 2.4 : Electronic Configuration of a Carbon Atom

2.4.2. Forms of carbon

Carbon exists in various allotropes, each exhibiting unique structural and physical properties. The most prominent include diamond, graphite, and fullerenes, while others encompass graphene, carbon nanotubes, and different forms of amorphous carbon [Elsa Garrido (2010)].

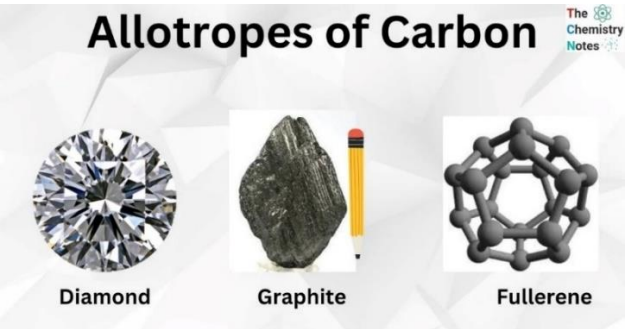


Figure 2.5 : Different Allotropes of Carbon

2.4.2.1 Graphite

Graphite exhibits a layered structure composed of stacked graphene sheets. Each sheet, or graphene plane, consists of carbon atoms in sp^2 hybridization, arranged in a hexagonal lattice with a unit cell parameter of 0.243 nm and C–C bond length of 0.142 nm. There are two known stacking configurations for graphene layers, resulting in two distinct crystalline forms of graphite.

The thermodynamically stable form is hexagonal graphite, where graphene layers are stacked regularly (see figure 2.10), with an interlayer spacing of 0.335 nm. The second form is rhombohedral graphite, a metastable phase of the hexagonal type. In this arrangement, each graphene layer is laterally shifted by one bond length with respect to the one below it, yet the interlayer spacing remains 0.335 nm.

In practice, graphite is rarely found as a single crystal. Although the growth of macroscopic graphite single crystals is possible, most commercial graphite, such as that used in pencils, is polycrystalline made up of randomly oriented hexagonal graphite crystallites.

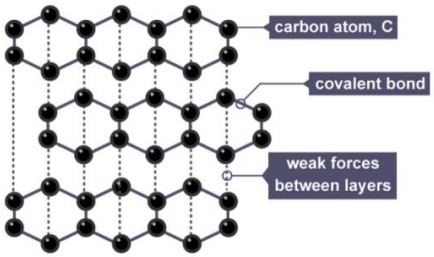


Figure 2.6 : Graphite structure

2.4.2.2 Diamond

Diamond possesses a face-centered cubic (FCC) crystal structure in which half of the tetrahedral sites are occupied (Figure 2.11). Each carbon atom is covalently bonded to four other carbon atoms in a regular tetrahedral arrangement, through sp^3 hybridized bonds. Unlike graphite, all valence electrons in diamond are engaged in strong covalent bonding, leaving no

free electrons. This highly rigid and tightly bonded three-dimensional lattice is what makes diamond the hardest known natural material.

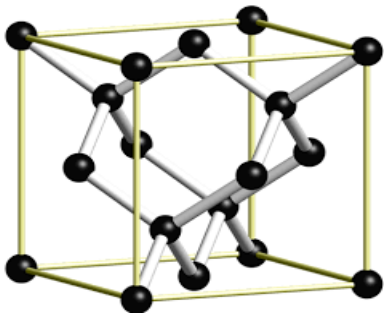


Figure 2.7 : Diamond structure

2.4.2.3 Fullerene

A fullerene is a carbon-based molecule that can take various shapes, including spherical, ellipsoidal, tubular (called nanotubes), or even ring-like structures. Structurally similar to graphite, fullerenes are composed of networks of hexagonal carbon rings, but also include pentagonal and occasionally heptagonal rings, which cause the carbon sheet to curve rather than remain flat.

The first discovered fullerene, known as C_{60}, consists of 12 pentagons and 20 hexagons, with each vertex representing a carbon atom and each edge a covalent bond. This geometry resembles a geodesic dome, which led to its name: "buckminsterfullerene", in honor of Buckminster Fuller, the architect of the geodesic dome. It is also known as "footballene", due to its similarity to a soccer ball.

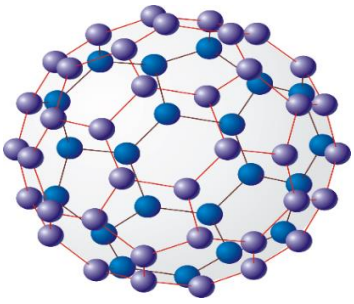


Figure 2.8 : Fullerene structure

2.5. Carbon nanotube

Carbon nanotubes (CNTs) are an allotropic form of carbon belonging to the fullerene family [David R. Lide, ed. (2005)]. Structurally, they consist of one or more graphene sheets rolled into seamless cylindrical tubes. These tubes may be either open-ended or capped with hemispherical fullerene-like structures. CNTs are typically classified into two categories:

single-walled carbon nanotubes (SWCNTs) and multi-walled carbon nanotubes (MWCNTs), depending on number of graphene layers forming the tube.

The discovery of CNTs is closely linked to the study of C_{60} fullerene synthesis conditions. In 1991, Sumio Iijima observed CNTs while investigating these synthesis processes. CNTs were thus defined as graphene sheets rolled into cylindrical structures (Figure 2.13). A single-walled carbon nanotube (SWCNT) specifically refers to tubular formation of a single graphene layer.

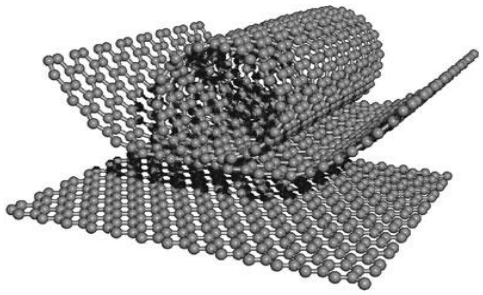


Figure 2.9 : Schematic of how graphene could roll up to form a carbon nanotube

2.5.1. Discovery of carbon nanotubes

In a 2006 editorial published in the journal Carbon, Marc Monthioux and Vladimir Kuznetsov addressed the intriguing yet often overlooked history of carbon nanotubes. Contrary to popular belief, the discovery of nanometer-scale tubular graphite structures is frequently—but inaccurately credited solely to Sumio Iijima (NEC) in 1991.

In reality, carbon nanotubes (CNTs) have existed for millennia. As early as the discovery of fire approximately 500,000 years ago, trace amounts of such nanostructures were formed in the soot generated by combustion. Under high temperatures, carbon molecules undergo fragmentation and reassembly into various configurations, occasionally giving rise to amorphous carbon droplets or even geodesic nanostructures.

The first documented observation of carbon nanotubes dates back to 1952, when Radushkevich and Lukyanovich published clear transmission electron microscopy (TEM) images of carbon tubes approximately 50 nm in diameter in the Journal of Physical Chemistry [Chung (2002)]. However, recognition of this discovery was limited because the paper was published in Russian. During the Cold War, Western scientists had restricted access to Soviet scientific literature, which was no longer systematically translated into English.

While CNTs were indeed produced long before 1991, it was the invention and advancement of the transmission electron microscope (TEM) that eventually enabled the direct visualization of these nanostructures.

In 1976, Oberlin, Endo, and Koyama published a paper demonstrating hollow carbon fibers at the nanometer scale, produced via chemical vapor deposition (CVD) methods.

Later, in 1981, a group of Soviet scientists conducted detailed structural and chemical characterizations of carbon nanoparticles synthesized through the thermo-catalytic disproportionation of carbon monoxide. Using TEM and X-ray diffraction, they concluded that their multi-walled carbon nanotube (MWCNT) structures were formed by rolling graphene sheets into cylinders. They also proposed two configurations for this rolling process: a circular "armchair" structure and a spiral "chiral" configuration.

Finally, in 1993, Sumio Iijima and Donald S. Bethune (IBM, California) independently succeeded in synthesizing single-walled carbon nanotubes (SWCNTs). While Iijima achieved this through gas-phase methods, Bethune used a co-vaporization process involving carbon and cobalt.

2.5.2. Carbon nanotube structure

There are three types of carbon nanotubes:

***Single-Walled Carbon Nanotube,* SWCNT**: It consists of a single graphene sheet rolled into a cylindrical shape. This is the simplest and thinnest form of carbon nanotubes (CNTs).

***Double-Walled Carbon Nanotube,* DWCNT**: It consists of two concentric carbon nanotubes. This configuration integrates the properties of both single-walled (SWCNT) and multi-walled (MWCNT) carbon nanotubes.

***Multi-Walled Carbon Nanotube,* MWCNT**: It consists of multiple concentric graphene layers rolled into nested tubes. This structure offers greater mechanical robustness but lower flexibility compared to single-walled carbon nanotubes (SWCNTs).

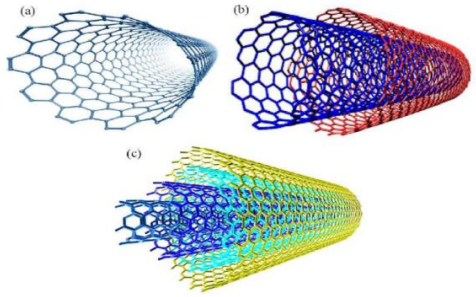


Figure 2.10 : Types of Carbon Nanotubes structure : a) SWCNT ; b) DWCNT ; c) MWCNT

2.5.3. Properties of carbon nanotubes

Carbon nanotubes (CNTs) exhibit exceptional and multifunctional properties that make them ideal for numerous engineering and scientific applications. Their properties can be categorized as mechanical, electrical, chemical, physical, and optical.

2.5.3.1 Mechanical properties

Carbon nanotubes exhibit remarkable mechanical properties due to their strong carbon–carbon (C–C) covalent bonds. To effectively integrate CNTs into engineering applications, it is essential to study their mechanical behavior, including both elastic and inelastic responses, as well as tensile and fracture strength.

Treacy investigated the elastic behavior of single-walled carbon nanotubes (SWCNTs) to analyze their intrinsic vibration amplitudes under a transmission electron microscope (TEM), revealing a Young's modulus of approximately 1.05 TPa.

Wong's research group measured the Young's modulus of multi-walled CNTs (MWCNTs) using an atomic force microscope (AFM)**.** By analyzing the lateral deflection of the nanotubes as they interacted with the AFM cantilever, they reported a value of 1.26 TPa, slightly higher than that of SWCNTs and significantly higher than conventional carbon fibers (230 GPa)**.**

Furthermore, the tensile strength of both SWCNTs and MWCNTs is estimated around 150 GPa, which is far superior to that of traditional materials like carbon fibers, steel, wood, or epoxy resins. Combined with their low density (1.9 g/cm³ for some MWCNTs), CNTs are considered excellent candidates for use in high-performance structural composites.

2.5.3.2 Electrical properties

The electrical behavior of carbon nanotubes is primarily determined by their chirality.

- Only armchair (n = m) CNTs are truly metallic, while others are semiconducting.
- The bandgap of semiconducting CNTs varies based on their diameter and chiral angle.
- For CNTs where n − m = 3j (with *j* being a non-zero integer), the bandgap is small, and thermal excitation at room temperature allows them to behave as conductors.

Techniques have been developed to separate CNTs based on their electrical type (metallic vs. semiconducting) to enable targeted applications.

Experimental two- or four-probe measurements on MWCNTs show electrical conductivities ranging from 10^4 to 10^7 S/m at room temperature lower than silver (6.3×10^7 S/m), the most conductive metal, due to CNT geometry and measurement challenges.

Notably, superconductivity has also been observed in some CNTs at cryogenic temperatures.

2.5.3.3 Chemical properties

Nanotubes are hollow structures that can be filled with other chemical compounds, making them closed containers on a nanometric scale. Carbon nanotubes are relatively unreactive, and chemical modification of their surface often involves highly reactive species (strong oxidizers, strong reducers, radical species). This is why nanotube grafting chemistry based on non-

covalent interactions has developed strongly in recent years (adsorption of surfactants, winding of polymers, DNA and adsorption of pyrenes, etc.) [Hirsch (2002)].

2.5.3.4 Physical properties

Their exceptional stiffness combined with high deformability endows them with superior energy absorption capabilities, exceeding those of conventional materials like Kevlar and spider silk. These properties make them ideal candidates for integration into advanced, lightweight protective systems such as bumpers and ballistic vests.

2.5.3.5 Optical properties

The blackest material ever conceived by man is a carpet of vertically arranged nanotubes, created by Rice University researchers working with Professor Pulickel Ajayan, with a reflection index of 0.045%, it is thirty times darker than carbon, enabling it to absorb 99.955% of the light it receives. This albedo is three times than that of nickel-phosphorus alloy, reputed to be the darkest material. material. These inventions could be of interest to the military, communications, energy (especially solar), observation, dyes, etc.

2.5.4. Synthesis of Carbon Nanotubes

Currently, carbon nanotubes (CNTs) are primarily synthesized using three key techniques: arc discharge, laser ablation of graphite, and chemical vapor deposition (CVD). In the arc discharge and laser ablation methods, graphite is vaporized either through electrical discharge or laser energy, with CNTs forming in the gas phase and then collected. All three methods rely on metal catalysts such as iron, cobalt, or nickel to facilitate CNT formation [Nanowerk (2025)].

- ***CVD process***

The Chemical Vapor Deposition (CVD) method is currently considered the most promising technique for CNT production, as it enables large-scale synthesis under controlled conditions and at relatively low cost. In this process, a metal catalyst typically iron is exposed to carbon-containing gases such as hydrogen or carbon monoxide within a high-temperature furnace, promoting the growth of carbon nanotubes on the catalyst surface. The CVD technique can be either purely catalytic or enhanced by plasma assistance. The plasma-assisted variant operates at moderately lower temperatures (typically 200–500°C) compared to the conventional catalytic CVD process, which can reach up to 750°C. This approach is particularly suited for generating vertically aligned, "lawn-like" growth of carbon nanotubes.

- ***Purification***

Although advancements in synthesis techniques have allowed the production of high-purity carbon nanotubes (CNTs), the formation of impurities such as metal-encapsulated nanoparticles, catalyst residues at the nanotube tips, and amorphous carbon remains unavoidable due to the essential role of metal catalysts in CNT growth.

These residual nanoparticles and structural defects introduced during synthesis can significantly alter the physical and chemical properties of the resulting CNTs. Therefore, post-synthesis purification processes, such as acid treatments and ultrasonic dispersion, are necessary to remove these impurities and ensure the quality and performance of the final product.

2.5.5. Carbon nanotube applications

Carbon nanotubes (CNTs) are used in various advanced applications, including electronics, aerospace structures, energy storage, composite materials, thermal management, environmental applications and emerging fields thanks to their excellent mechanical, electrical, and thermal properties. The main application domains can be summarized as follow:

- **Electronics**

CNTs enable advanced electronics through exceptional electrical properties. They are used in high-frequency transistors, flexible displays, and nano-sensors, allowing for smaller, faster devices that surpass conventional material limitations.

- **Composite Materials**

CNTs reinforce polymers to create lightweight, high-strength composites for aerospace and automotive industries. They enhance mechanical properties while adding functionality like electrical conductivity for smart materials.

- **Environmental Applications**

CNTs purify water and air through high adsorption capacity and catalytic activity. They effectively remove contaminants and enable sensitive environmental monitoring sensors for sustainable remediation.

- **Energy Storage**

CNTs improve batteries and supercapacitors by enhancing electrode conductivity and stability. They enable higher energy density, faster charging, and longer cycle life in advanced energy storage systems.

- **Thermal Management**

CNTs excel at heat dissipation in electronics due to exceptional thermal conductivity. They are used in thermal interface materials, heat sinks, and cooling systems for efficient thermal management.

- **Emerging Fields**

CNTs drive innovation in smart textiles, wearable health monitors, and biomedical applications. Their unique properties enable advanced drug delivery, biosensors, and neural interfaces for next-generation technologies.

Chapter 3 Plate theory

Objective

This chapter is dedicated to the presentation of different plate theories, their assumptions, and displacement fields. It begins by the theory of plates including shear effects including Classical Plate Theory (CPT), followed by the First-Order Shear deformation theory (FSDT). In addition, other Higher-order Shear Deformation Theories (HSDT) have been investigated in details. Furthermore, Refined Plate Theory (RPT), Quasi-3D theory, and Layered approach are provided which offer enhanced accuracy in predicting the mechanical behavior of advanced composite and sandwich structures. Then, two theories of plates including scale effects are discussed, the Local and Non-Local Elasticity theories.

3.1. Theory of plates including shear effects

The development of plate theories necessitates the adoption of specific assumptions that serve as reasonable simplifications of real structural behavior. Various theoretical models in the literature are distinguished primarily in their treatment of transverse shear deformation. To enhance the accuracy of displacement field representation through the plate thickness, several advanced plate theories have been proposed and will be examined in this chapter.

3.1.1. Theory of thin plates

For thin plates, where shear deformation is negligible compared to bending, simplified models like the Classical Plate Theory (CPT), introduced by Kirchhoff in 1850, are commonly used. This theory describes the stress and strain in terms of transverse displacement of mid-surface and is valid when the thickness is assumed to be small compared to the other dimensions of the plate $\left(\frac{h}{L} < \frac{1}{20}\right)$ (high slenderness ratio).

3.1.1.1 Classic plate theory (CPT)

Since this model adopts the Love-Kirchhoff plane stress assumption, transverse shear deformations are neglected. The theory is formulated based on linear distribution of displacements through the plate thickness [Reissner et Stavsky (1961), Yang et al. (1966)] and assumes that the normal to the mid-surface remains straight and perpendicular to the mid-plane after deformation (Figure 3.1). It states the following hypotheses [Kirchhoff (1850)]:

- ✓ There is no in-plane deformation of the plate mid-surface, which remains neutral during bending.
- ✓ Straight lines normal to the mid-surface remain straight and normal after deformation.
- ✓ Deflection of the mid-surface is small compared to the plate thickness.
- ✓ Normal applied stresses on planes parallel to the plate surfaces can be neglected.

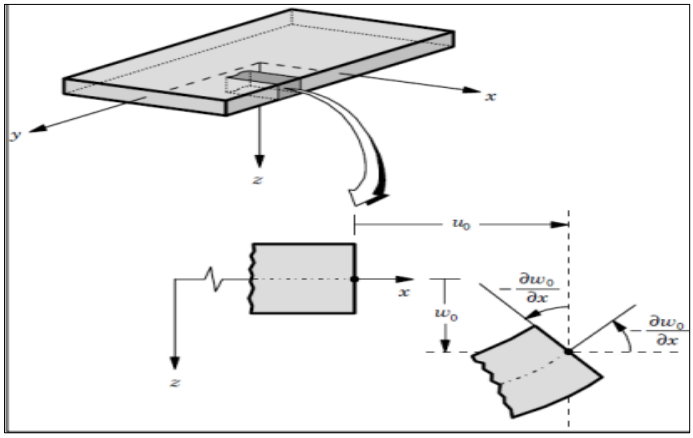


Figure 3.1: Love Kirchhoff plate kinematics (CPT) [Reddy (2003)].

The displacement field components within the framework of thin plate theory are defined as follows:

$$u(x,y,z,t) = u_0(x,y,t) - z\frac{\partial w_0}{\partial x} \tag{3.1}$$

$$v(x,y,z,t) = v_0(x,y,t) - z\frac{\partial w_0}{\partial y} \tag{3.2}$$

$$w(x,y,z,t) = w_0(x,y,t) \tag{3.3}$$

Where (u_0, v_0, w_0) denote the displacement components at the mid-surface of plate($z = 0$). Due to the neglect of transverse shear effects, Classical Plate Theory yields inaccurate predictions for thick plates, especially those made of advanced composite materials. To overcome this limitation, the First-order Shear Deformation Theory was initially introduced.

3.1.2. Theory of thick plates

When dealing with moderately thick to thick plates, it is crucial to incorporate transverse shear deformation and rotary inertia effects to ensure accurate representation of their dynamic response. The Classical Love-Kirchhoff Plate Theory neglects these factors, resulting in inaccurate predictions for thick plates. To address this limitation, refined theories were introduced by several researchers. Reissner was among the first to propose a thick plate theory in 1945, incorporating transverse shear effects through the inclusion of an additional term in the strain energy expression. Subsequently, Mindlin (1951) developed a First-order Shear Deformation Theory, which included shear deformation along with a shear correction factor. In the literature, plate models based on these first-order shear assumptions are commonly referred to as Mindlin, Reissner-Mindlin, or Hencky-Mindlin plate theories.

3.1.2.1 First-order shear deformation theory (FSDT)

Two similar, though not identical, theories were proposed by Eric Reissner in 1945 and Raymond Mindlin (1951)]. Both were developed for the analysis of thick plates, where the normal to the mid-surface remains straight but not required necessarily perpendicular to mid-surface after deformation.

The main distinction lies in the fact that theory of Reissner does not assume a plane stress condition, allowing for thickness variation during deformation (Figure 3.2). The Mindlin-Reissner theory follows Mindlin assumptions and is therefore more accurately referred to as Mindlin plate theory. This model is also known as the First-order Shear Deformation Theory, as it assumes a linear distribution of displacement through the thickness of plate.

Mindlin theory is applicable in cases where the thickness-to-length ratio of the plate exceeds 1/20. It is built upon the following assumptions:

- ✓ The normal stress σ_{zz} is negligible compared to σ_{xx} and σ_{yy}.
- ✓ The transverse shear strain is considered to be zero $\epsilon_{zz} = 0$.
- ✓ Points initially located along the normal to the mid-plane may not remain on the same normal after deformation.
- ✓ The influence of rotary inertia is additionally incorporated into the formulation.

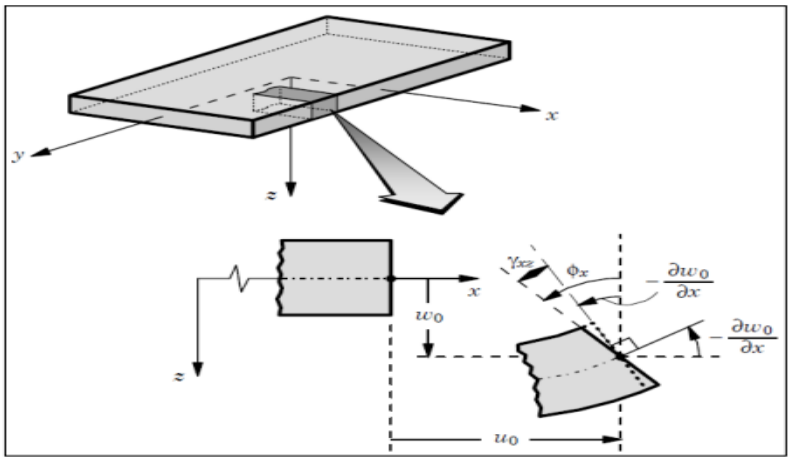


Figure 3.2 : Reissner-Mindlin plate kinematics (FSDT) [Reddy (2003)].

The displacement field of the First-order Shear Deformation Theory is given by:

$$u = u_0(x, y, t) + z\theta_y(x, y, t) \tag{3.4}$$

$$v = v_0(x, y, t) - z\theta_x(x, y, t) \tag{3.5}$$

$$w = w_0(x, y, t) \tag{3.6}$$

This theory utilizes three displacement components defined on the mid-surface $(u_0, v_0 \; and \; w_0)$ and two rotational variables $(\theta_x \; and \; \theta_y)$ to describe the deformation. The rotational components correspond to the transverse rotations around the x and y axes, respectively.

3.1.3. Higher-order shear deformation theory (HSDTs)

In Classical Plate Theory, the distribution of displacements through the thickness is taken to be linear. First-order shear deformation theory considers uniform transverse shear strain across the thickness. In contrast, Higher-order Shear Deformation Theory (HSDT) adopts nonlinear displacement field through the thickness, allowing a parabolic variation of transverse shear strains and stresses. As a result, it eliminates the need for shear correction factors. Several Higher-order Shear Deformation theories have been proposed by [P. M. Naghdi, s. d. , Reddy (1984), Thai et al. (2012), Reddy (2006), Iyengar et al. (1974), Murty (1977), Murty (1986),

Krishna Murty (1987)]. These theories generally employ a Taylor series expansion of displacement field through the plate thickness, typically expressed in the following form:

$$u_i(x,y,z) = u_0(x,y) + z\emptyset_i^{(1)}(x,y) + z^2\emptyset_i^{(2)}(x,y) + \cdots + z^j\emptyset_i^{(j)}(x,y) \tag{3.7}$$

where j denotes the order of approximation used in the model. In the Kirchhoff-Love theory, $j = 0$. The Reissner-Mindlin theory is a First-order Shear Deformation Theory characterized by $j = 1$ concerning the in-plane displacements and $j = 0$ concerning the transverse displacement. According to Reddy (1990) and Mallikarjuna et Kant (1993), the development of these higher-order theories is based on the following assumptions:

- ✓ Displacements are assumed to be small relative to the plate thickness.
- ✓ Cross-sections that are initially plane and perpendicular to the mid-surface do not necessarily remain plane and perpendicular after deformation.
- ✓ Axial strain in the transverse (thickness) direction is not negligible.
- ✓ Normal stress acting in the transverse direction is generally considered non-negligible.

Higher-order shear deformation theories are founded on the formulations proposed by [Reissner (1945), Mindlin (1951), and Thai et al. (2012)]. The associated displacement field is generally is typically expressed in the following form:

$$u(x,y,z) = u_0(x,y) - z\frac{\partial w_0(x,y)}{\partial x} + f(z)\theta_x(x,y) \tag{3.8}$$

$$v(x,y,z) = v_0(x,y) - z\frac{\partial w_0(x,y)}{\partial y} + f(z)\theta_y(x,y) \tag{3.9}$$

$$w(x,y,z) = w_0(x,y) \tag{3.10}$$

$f(z)$ is the transverse shear shape function that characterizes the specific shear deformation theory. It is noted that the classical plate theory corresponds to the case $f(z) = 0$, while the First-order Shear Deformation Theory is recovered by choosing $f(z) = z$.

Reddy proposed a Third-order Shear Deformation Theory [Reddy (2003)] , which can be derived by adopting the following expression:

$$f(z) = z\left(1 - \frac{4z^2}{3h^2}\right) \tag{3.11}$$

In this model, the in-plane displacement field is cubic through the thickness, and the transverse shear stress distribution is parabolic, and the boundary conditions applied on the free surfaces are satisfied. As a result, a good approximation can be obtained for the transverse shear stresses are evaluated with respect to the three-dimensional elasticity solution.

Touratier (1991) proposed the Sinusoidal Shear Deformation Theory (SSDT), which employs a sinusoidal trigonometric function to model the distribution of transverse shear stress

across the plate thickness. This approach differs from other higher-order theories that typically rely on polynomial functions. The shear function is defined as follows:

$$f(z) = \frac{h}{\pi}\sin\left(\frac{\pi z}{h}\right) \tag{3.12}$$

An exponential version of the Higher-order Shear Deformation Theory, known as the Exponential Shear Deformation Theory (ESDT), was developed by Karama et al. (2003) by adopting the following shear shape function:

$$f(z) = ze^{-2\left(\frac{z}{h}\right)^2} \tag{3.13}$$

Other Higher-order Shear Deformation Theories have been derived using various transverse shear shape functions. Table 3.1 presents the different shear functions that characterize each theory.

Table 3.1 : Different shear functions formula

Theory	**Shear Function $f(z)$**
Third-Order Shear Deformation Theory TSDT [Reddy (2003)]	$f(z) = z\left(1 - \frac{4z^2}{3h^2}\right)$
Sinusoidal Shear Deformation Theory SSDT [Touratier (1991)]	$f(z) = \frac{h}{\pi}\sin\left(\frac{\pi z}{h}\right)$
Exponential Shear Deformation Theory ESDT [Karama et al. (2003)]	$f(z) = ze^{-2\left(\frac{z}{h}\right)^2}$
Reissner [Reissner (1975)]	$f(z) = \frac{5}{4}z\left(1 - \frac{4z^2}{3h^2}\right)$
Soldatos [Soldatos et Timarci (1993)]	$f(z) = h\sinh\left(\frac{z}{h}\right) - z\cosh\left(\frac{1}{2}\right)$
Mantari [Mantari et al. (2012)]	$f(z) = \sin\left(\frac{\pi z}{h}\right)e^{m\cos\left(\frac{\pi z}{h}\right)} + m\left(\frac{\pi z}{h}\right)$
Ait Atmane [Ait Atmane et al. (2010)]	$f(z) = \frac{\cosh\left(\frac{\pi}{2}\right)}{\left[\cosh\left(\frac{\pi}{2}\right) - 1\right]}z - \frac{\left(\frac{h}{\pi}\right)sinh\left(\frac{\pi z}{h}\right)}{\left[\cosh\left(\frac{\pi}{2}\right) - 1\right]}$
Elmeiche [El Meiche et al. (2011)]	$f(z) = \frac{\left(\frac{h}{\pi}\right)sinh\left(\frac{\pi z}{h}\right)}{\cosh\left[\left(\frac{\pi}{2}\right) - 1\right]} - z$
Aydogdu [Aydogdu (2009)]	$f(z) = z\alpha^{\frac{-2\left(\frac{z}{h}\right)^2}{\ln(\alpha)}}$
Nguyen [Nguyen et al. (2007)]	$f(z) = sinh^{-1}\left(\frac{3z}{h}\right) - z\left(\frac{6}{h\sqrt{13}}\right)$

3.1.4. Refined Plate Theory (RPT)

To simplify the formulation of Higher-order Shear Deformation Theories, Shimpi (2002) proposed a refined model for isotropic plates, termed the Refined Plate Theory (RPT) [Rameshchandra P. Shimpi (2012)]. This theory presents several key advantages, including the removal of shear correction factors while maintaining governing equations, boundary conditions, and moment expressions similar to those of the Classical Plate Theory (CPT). The accuracy of RPT has been validated in studies on static bending and buckling of composite plates by Kim et al. (2009) and Ait Atmane et al. (2010). Subsequent applications include the buckling behavior of orthotropic plates analyzed by Thai et Kim (2011) and the free vibration of laminated and sandwich plates by L. Hadji, H. A. Atmane, A. Tounsi, I. Mechab & E. A. Adda Bedia (2011).

In the refined plate theory, the displacement field is defined as follows:

$$u(x,y,z) = u_0(x,y) - z\frac{\partial w_b(x,y)}{\partial x} + f(z)\frac{\partial w_s(x,y)}{\partial x} \tag{3.14}$$

$$v(x,y,z) = v_0(x,y) - z\frac{\partial w_b(x,y)}{\partial y} + f(z)\frac{\partial w_s(x,y)}{\partial y} \tag{3.15}$$

$$w(x,y,z) = w_b(x,y) + w_s(x,y) \tag{3.16}$$

where, w_b and w_s denote the bending-related and shear-related components of the transverse displacement, respectively.

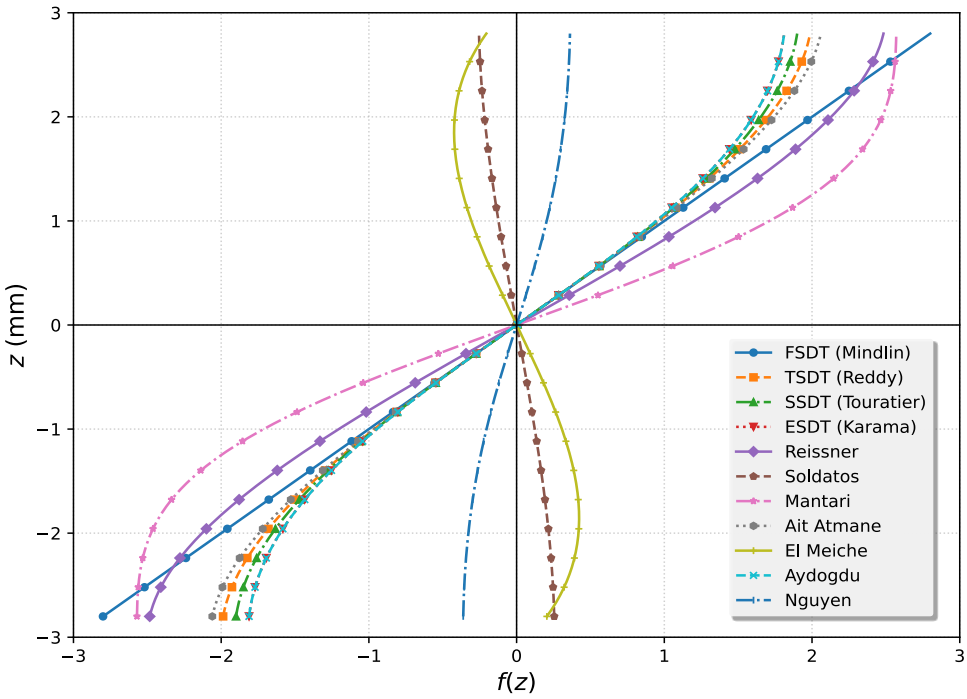


Figure 3.3 : Comparison of transverse shear shape function of the different models

3.1.5. Quasi-3D Theory

It should be emphasized that the classical and some Higher-order Plate theories typically disregard the effect due to thickness stretching (i.e., $\varepsilon_z = 0$) by assuming uniform transverse displacement across the thickness. While this simplification may be acceptable for thin plates, it leads to inaccuracies in the modeling of moderately thick and thick plates, where thickness stretching becomes significant and must be properly addressed. Quasi-3D shear deformation theories, which represent an advanced class of Higher-order Shear Deformation Theories, overcome this limitation by incorporating more refined variation considering both in-plane and transverse displacement variations through the thickness. Consequently, these models simultaneously capture transverse shear deformation and normal stretching effects with improved accuracy [Thai et Kim (2013)]. In the quasi-3D theory, the displacement field expressed as:

$$u(x,y,z) = u_0(x,y) - z\frac{\partial w_0(x,y)}{\partial x} + f(z)\varphi_x(x,y) \tag{3.17}$$

$$v(x,y,z) = v_0(x,y) - z\frac{\partial w_b(x,y)}{\partial y} + f(z)\frac{\partial w_s(x,y)}{\partial y} \tag{3.18}$$

$$w(x,y,z) = w_0(x,y) + g(z)\varphi_z(x,y) \tag{3.19}$$

Where $u_0, v_0, w_0, \varphi_x, \varphi_y$ and φ_z represent the six unknown displacement components associated with the midplane of plate. Further assumptions are stated as follows:

$w_0(x,y) = w_b(x,y) + w_s(x,y)$, $g(z) = \frac{df(z)}{dz}$, $\varphi_x = \frac{\partial w_s}{\partial x}$ and $\varphi_y = \frac{\partial w_s}{\partial y}$

φ_z represents an additional displacement that accounts concerning the effect of normal stress (thickness stretching), while $f(z)$ and $g(z)$ are transverse shear shape functions.

3.1.6. Layered approach

3.1.6.1 Discrete-layer models

Discrete layer models, also referred to as layer-wise or equivalent single-layer approaches, are commonly used to model laminated composite structures. In these models, the composite is divided into a series of distinct layers, each represented by a plate or finite element with its own specific material properties. Mechanical characteristics such as stiffness and strength may vary from one layer to another to account for differences in composition, fiber orientation, and other microstructural features.

3.1.6.2 Zigzag models

Zig-zag models, also referred to as laminated models or multilayer shear deformation theories, are widely employed to simulate mechanical behavior of laminated composite

structures. These models are formulated based on the decomposition of laminate into a sequence of individual layers, each considered as a homogeneous material with distinct mechanical properties (e.g., stiffness, density, fiber orientation).

A key feature of zig-zag models is that the displacement field is enriched with piecewise linear or nonlinear functions that introduce discontinuities in the derivatives of the in-plane displacements, while preserving displacement continuity across layer interfaces, as illustrated in figure 3.4. This approach enables offering a more precise representation of the interlaminar stress distribution, especially at the interfaces between layers with contrasting properties.

The kinematics in zig-zag theories are formulated such that the continuity conditions at the interfaces are satisfied a priori, and the formulation remains independent of the number of layers [Berreur, Louis (2002)].

Zig-zag theories offer a computationally efficient alternative to full layerwise models, balancing accuracy and complexity. They are particularly effective for moderately laminated structures and are often used in the analysis of sandwich panels, fiber-reinforced laminates, and functionally graded layered composites, where capturing the zig-zag nature of displacement fields is essential for predicting delamination and interfacial stresses.

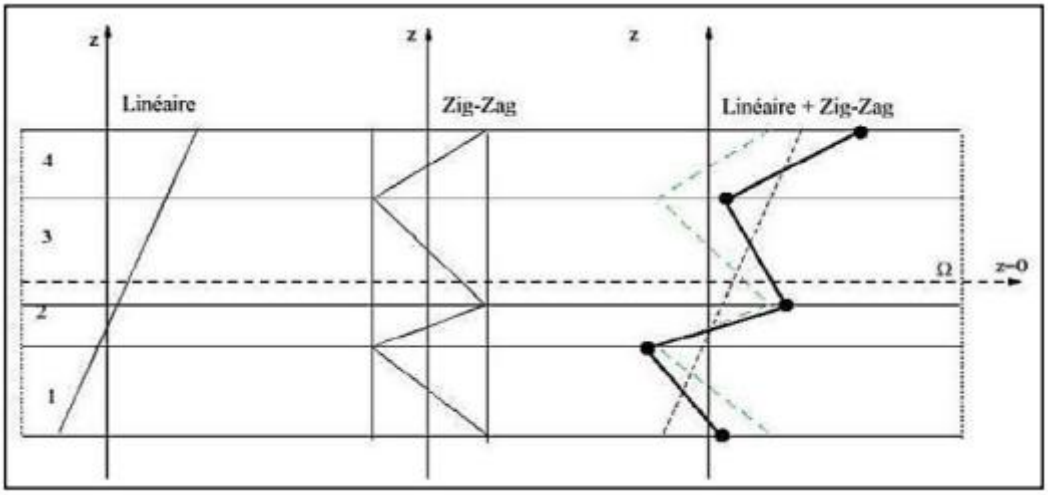


Figure 3.4 : Schematic representation of the zig-zag displacement field of first order zig-zag models [D. Baptiste, R. O. Polit, R. A. Chabot, E. M. Boussu, and J. F. Caron (2004)]

Chapter 4 P-version of Finite Element Method

Objective

This chapter focuses on the presentation of the Finite Element Method (FEM). It begins with a brief historical overview of the FEM, highlighting its development and significance in computational mechanics. The subsequent sections discuss the advantages and limitations of the p-version, providing insights into its distinctive features. A comparative analysis between the p- and h-versions is then presented to demonstrate the superior accuracy of the p-version when dealing with problems exhibiting smooth solution profiles. The chapter also details the numerical implementation of the p-version approach, emphasizing the use of Legendre and shifted Legendre polynomials as fundamental basis functions. Additionally, it introduces the concept of hierarchical interpolation functions and their application to both one-dimensional and two-dimensional elements, with comprehensive explanations of polynomial spaces, as well as quadrilateral and triangular p-elements.

4.1. Brief history of the p-version of the finite element method

The development of the *p*-version of the Finite Element Method (p-FEM) began in the 1970. A. Szabó (1986) introduced the use of variable-order (mixed) elements for 3D problems as an efficient means of adding degrees of freedom in high-gradient regions, using edge variables instead of additional nodes. They also introduced the fundamental concept of hierarchical p-refinement**.**

Later, Peano [A.G. Peano (1975), Peano (1976)] proposed hierarchical interpolation functions for straight-sided triangular elements, allowing construction of elements of arbitrarily high order, where each added degree of freedom corresponded to a higher-order derivative.

I.N. Katz, A.G. Peano and M.P. Rossow (1978) extended this approach by introducing the reference element to improve computational efficiency, along with precomputed arrays, and suggested extracting embedded lower-order solutions from high-order approximations.

O.C. Zienkiewicz, D.W. Kelly, J.P. de S, R. Gago and 1. Babuska (1981) later revisited their early interpolation schemes and developed hierarchical quadrilateral elements**,** highlighting benefits such as well-conditioned stiffness matrices, ease of compatibility enforcement**,** and implementation of error estimators**.**

A rigorous mathematical foundation for the p-method was presented by Babuska et al.(1981) , who proved convergence guarantees and established an a priori estimate showing that the p-method can achieve twice the convergence rate of the h-method in problems with singularities.

In a more comprehensive effort, Szabo et Actis (1996) authored a comprehensive book dedicated to the p-method, covering theoretical developments and applications in 1D and 2D problems, including electrostatics, potential flow, and the formulation of plate and shell elements**.**

4.2. Advantages of the p-version

The advantages of the *p*-version of FEM are [Belalia (2011)]:

- ✓ It offers higher accuracy and faster convergence than the h-version. The convergence rate is sometimes exponential and sometimes algebraic, but it is consistently superior to that of the h-method.
- ✓ The solution quality is less sensitive to element distortion, allowing the use of flattened elements or elements with high aspect ratios without significantly compromising accuracy.

- ✓ The p-version avoids numerical locking caused by the incompressibility of certain materials. However, when the Poisson's ratio approaches 0.5, higher polynomial degrees are required to achieve asymptotic convergence.
- ✓ Because the p-method uses a hierarchical formulation of displacement fields, the stiffness matrix at a given polynomial degree includes those of lower degrees, enabling the computation of a sequence of solutions economically, rather than only one as in the h-version.
- ✓ Mesh generation is simplified, as only a small number of macro-elements are required to model the structure, significantly reducing the effort in model preparation.

4.3. Limitations of the p-version

- ✓ The p-version is particularly suitable for detailed analysis of moderately complex structures, where the number of singularities is limited. In such cases, the method benefits from its high convergence rate, providing high-quality stress fields with relatively few degrees of freedom, which allows for accurate local analysis.
- ✓ However, for global structural analysis, especially in mechanical components with multiple geometric details, the p-version may become less efficient. Mesh generation with structured high-order elements can be very challenging, leading to a large number of elements, making the h-version more practical in such cases.
- ✓ For problems containing an infinite number of singularities, the p-version does not offer better convergence than the h-version.
- ✓ For the same number of degrees of freedom, the stiffness matrix in the p-version tends to be denser, resulting in higher memory requirements and longer computation times. However, with the use of appropriate solvers and numerical strategies, the accuracy gains of the p-version can outweigh the increase in computational cost [Carnevali et al. (1993)].

4.4. Comparison between version-p and -h

Two approaches are available to improve the accuracy of the finite element approximation. The most common approach is to refine the finite element mesh while maintaining the degree of the elements. This is known as the 'version-h' Finite Element Method.

The second method involves keeping the mesh size constant while allowing the degree of approximation of polynomial functions to tend to infinity [Peano (1976), Babuska et al. (1981)].

This approach is regarded as a better known as the *p*-version of the Finite Element Method, or the hierarchical finite element method (HFEM). Table 4.1 illustrates the comparison between the -h and -p versions according to several aspects discussed above.

Table 4.1 : Comparison between -h and -p versions of FEM

Aspect	***h*-Version FEM**	***p*-Version FEM (Hierarchical FEM)**
Refinement strategy	Refines the mesh (reduces element size h)	Increases the polynomial degree p while keeping the mesh fixed
Common terminology	Classical finite element method	Also called Hierarchical Finite Element Method (HFEM)
Condition of matrices	May be less well-conditioned	Produces better-conditioned matrices
Mesh modification	Requires mesh refinement	No need to remesh; easily implemented in adaptive analysis [(Peano et al. 1979), Papadrakakis et Babilis (1994)]
Accuracy with a single element	Limited	A single p-element can give accurate results for simple structures
Degrees of freedom required	Requires many DOFs for high accuracy	Fewer DOFs can achieve comparable accuracy [Houmat (1997), Houmat (2000), Houmat (2001), Houmat (2001), Houmat (2004)]
Locking issues	Sensitive to incompressibility locking	Can overcome locking problems [Zienkiewicz, O.C., and Taylor, R.L. (1994)]

4.5. Mesh adaptation

In order to improve the accuracy of finite element solution to a linear elasticity problem, the discretization parameters must be modified. This may be accomplished by refining the mesh, increasing the degree of interpolation used on the elements, or both simultaneously. Different procedures are available for refining finite element solutions. Broadly speaking, these can be classified into two categories:

- ✓ The -h refinement uses the same class of elements, but changes their size by enlarging or reducing it in certain places. This allows for maximum economy in finding the desired solution.

- ✓ The p-refinement strategy consists of keeping the element size constant and enhancing the approximation by increasing the polynomial order, often hierarchically.
- ✓ For solving a physical problem using FEM, an engineer must make a series of assumptions and approximations to transform a real object into a numerical model. The resulting discretization, which is defined by a mesh and the degree to which the elements are approximated, then provides an approximate solution. Based on the above, we look for the element's displacement field and the corresponding vibration equation.
- ✓ Each element has a continuous displacement field, expressed by approximation functions and displacements at selected points within the element. These points are often the nodes at the vertices. According to the simplest approximation function in linear form, the element displacement field u is expressed as follows [Cook, R.D., Malkus, D.S., and Plesha, M.E. (1989)]:

$$\{u\} = \sum_{i=1}^{n} N_i d_i = [N_i]\{d_i\} \tag{4.1}$$

where i denotes the vertex node number, $[N_i]$ comprises the shape functions of the first-order element, $\{d_i\}$ is the vector of unknown nodal displacements, and n is the number of vertex nodes. Using the Lagrange equation applied to energies (deformation and kinetic), the free vibration equation obtained by finite element is [Belalia (2011)]:

$$\left[[K_{ii}] - \omega^2[M_{ii}]\right]\{d_i\} = 0 \tag{4.2}$$

where $[K_{ii}]$ and $[M_{ii}]$ are the elementary stiffness and mass matrices.

4.6. Numerical implementation of the p-version approach

4.6.1. Legendre polynomials

The orthogonal Legendre polynomials $P_i(\xi)$ defined over the interval $[-1, +1]$, are given by:

$$\begin{cases} P_0(\xi) = 1 \\ P_n(\xi) = \dfrac{1}{2^n n!}\dfrac{d^n}{dx^n}[(x^2-1)^n] \quad n = 1, 2, 3, \ldots \end{cases} \tag{4.3}$$

They are solutions of the following differential equation for $n = 1, 2, \ldots$:

$$(1 - x^2)y'' - 2xy' + n(n+1)y = 0 \tag{4.4}$$

4.6.2. Shifted Legendre polynomials

The shape functions used are derived from shifted Legendre polynomials [Abramowitz, M., Stegun, I.A. (1965)] . These polynomials form a set of functions analogous to the standard Legendre polynomials, but are defined over a general interval $[a, b]$:

$$P_n^*(\xi) = P_n\left(\frac{2\xi - a - b}{b - a}\right) \tag{4.5}$$

These polynomials are orthogonal on the interval $[a, b]$.

Unlike standard Legendre polynomials defined over the interval $[-1,1]$, shifted Legendre polynomials are defined over the interval $[0,1]$. Accordingly, equation 4.5 becomes:

$$P_n^*(\xi) = P_n(2\xi - 1) \tag{4.6}$$

These polynomials have the following properties

- Orthogonality

$$\int_0^1 P_n^*(\xi)P_m^*(\xi)dx = \begin{cases} 0 & si\ n \neq m \\ \dfrac{1}{2n+1} & si\ n = m \end{cases} \tag{4.7}$$

- Recurrence formula

$$P_{n+1}^*(\xi) = \frac{1}{n+1}[(-2n - 1 + (4n + 2)\xi)P_n^*(\xi) - nP_{n-1}^*(\xi)], \quad n = 1,2, \ldots \tag{4.8}$$

- Normalization

$$P_n^*(1) = 1 \tag{4.9}$$

- Bounding property

Figure 4.1 displays the graph of the shifted Legendre polynomial $P_n^*(\xi)$, for $n = 1, 2, \ldots 7$ over the interval $\xi \in [0,1]$, $\forall\, n$:

$$|P_n^*(\xi)| \leq 1 \ \text{ for all } 0 \leq \xi \leq 1 \tag{4.10}$$

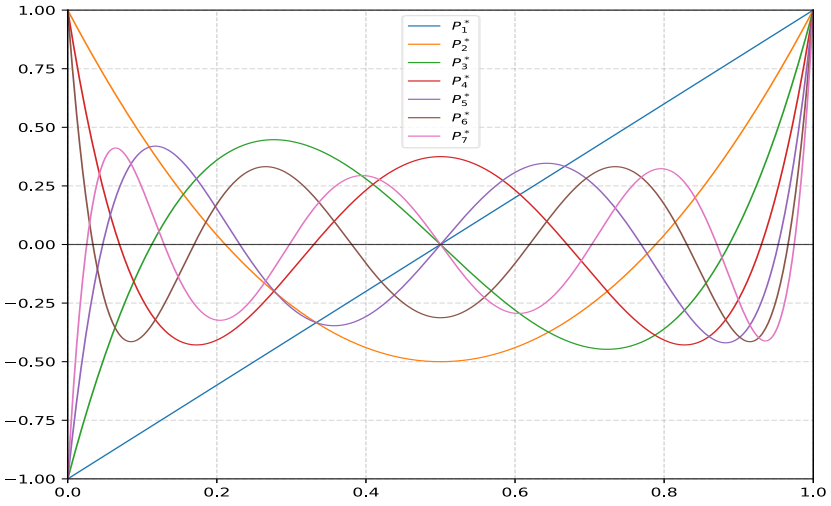


Figure 4.1 : Shifted Legendre Polynomial.

4.6.3. *p*-version and hierarchical interpolation functions

Since the early development of the Finite Element Method, high-order interpolation has been tested with varying degrees of success. These early attempts laid the foundation for what

would later become known as the p-version of FEM. However, it was not until the introduction of a hierarchical formulation [A.G. Peano (1975)] that its full potential could be effectively realized.

Driven by the work of several research groups [Babuška et Suri (1990), Szabó (1991), Zienkiewicz, O.C., and Taylor, R.L. (1994)], hierarchical approach matured during the mid-1980 and has since been adopted in commercial engineering software such as Pro/MECHANICA, StressCheck, and ANSYS.

A finite element-based approximation of the form:

$$\{u_h\} = \sum_{i=1}^{n} N_i a_i \tag{4.11}$$

is considered hierarchical when the increase of the degree from n to $n+1$ does not modify the lower-order shape functions N_i for $i = 1, \dots, n$.

Among the key advantages of the p-version with hierarchical formulation are:

- ✓ It allows the use of an industrial-grade mesh, where the element size remains unchanged throughout the analysis.
- ✓ It produces solutions that are less sensitive to numerical errors.
- ✓ It generally maintains a favorable convergence rate.
- ✓ It provides an economical error indicator, which is essential for implementing automated computation procedures.

4.6.3.1 One-dimensional elements

According to the characteristics of the displaced Legendre polynomials, we can obtain the hierarchical shape functions of a one-dimensional element (Figure 4.2)

$$N_1 = 1 - \xi \tag{4.12.1}$$

$$N_2 = \xi \tag{4.12.2}$$

$$N_{i+1}(\xi) = \sqrt{2i-1} \int_0^{\xi} P_{i-1}^{*}(t)dt \quad i \geq 2 \tag{4.12.3}$$

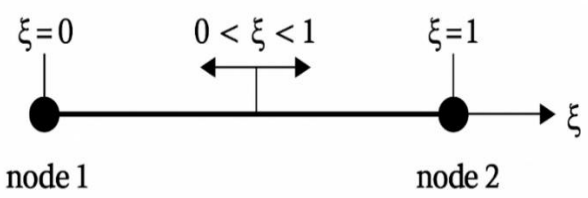


Figure 4.2 : One-dimensional element.

In a one-dimensional p-element, N_1 and N_2 represent the nodal (external) shape functions corresponding to the two end nodes of the element.

Shape functions N_i, with $i = 3,4, ...$, are internal shape functions. These are referred to as hierarchical because the set of shape functions of polynomial degree p inherently includes all those of lower degrees: $p-1, p-2, \ldots$, down to 1.

The nodal shape functions ensure displacement continuity between adjacent elements by connecting shared nodes.

The hierarchical internal functions enrich the element's displacement field, allowing for higher-order accuracy without altering the mesh.

Figure 4.3 illustrates the hierarchical structure regarding the stiffness matrix corresponding to a polynomial degree of $p = 3$, showing how the lower-degree functions are embedded. Figure 4.4 presents the first six internal hierarchical shape functions of one-dimensional finite element.

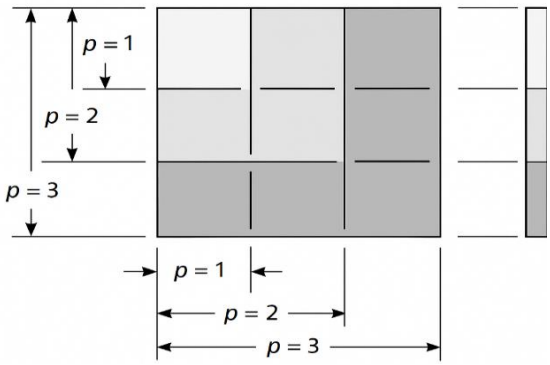


Figure 4.3 : Hierarchical structure of a stiffness matrix corresponding to polynomial degree $p = 3$.

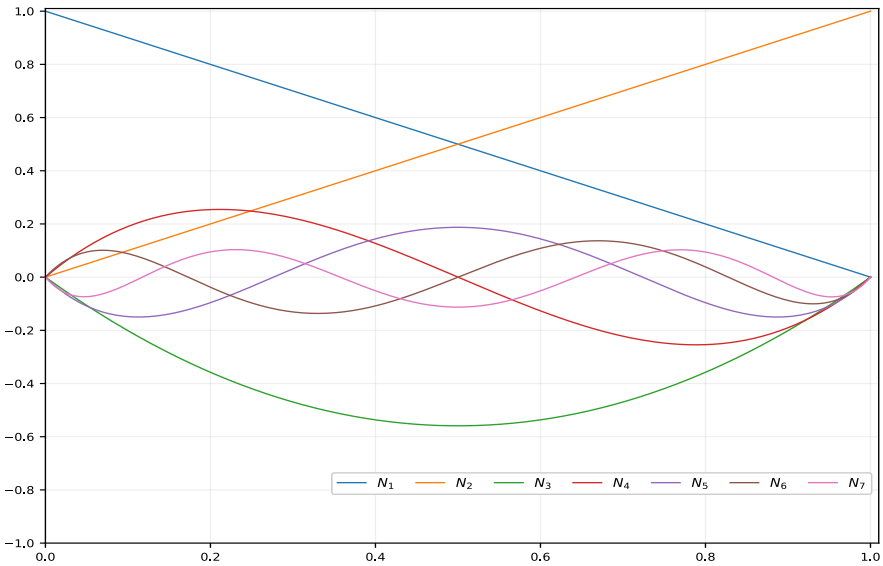


Figure 4.4 : Hierarchical shape functions.

4.6.3.2 Two-dimensional p-elements

a) Polynomial spaces

For a square domain $\Pi = \{0 \leq \xi, \eta \leq 1\}$, there exist three families of polynomial spaces as defined by [Zienkiewicz, O.C., and Taylor, R.L. (1994)]:

- Space $S^p(\Omega)$ or Serendipity family (Figure 4.5):

It corresponds to the set of all monomials $\xi^i \eta^j$, with $i, j = 0,1, \ldots, p$ and $i + j = 0,1, \ldots, p$. In addition:

- If $p = 1$, the monomial $\xi\eta$ is included.
- If $p \geq 2$, the monomials $\xi^p \eta$ and $\xi \eta^p$ are also included.

These additional monomials do not increase the polynomial degree along the edges of the reference element, ensuring compatibility with boundary interpolation.

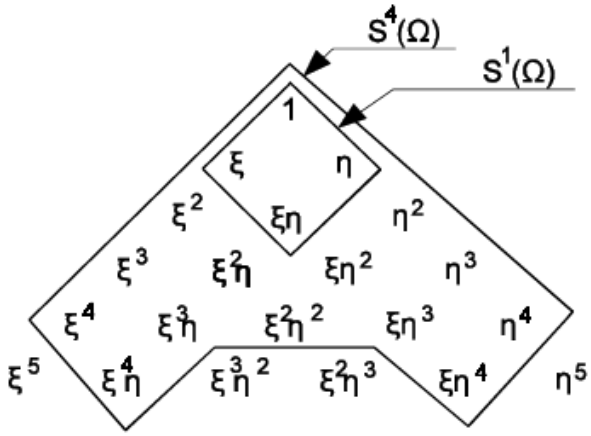


Figure 4.5 : "Serendipity" family

- Space $S^{p,q}(\Omega)$ or Lagrange family (Figure 4.6):

It corresponds to the set of all monomials $\xi^i \eta^j$, where $i = 0,1, \ldots, p$ and $j = 0,1, \ldots, q$.

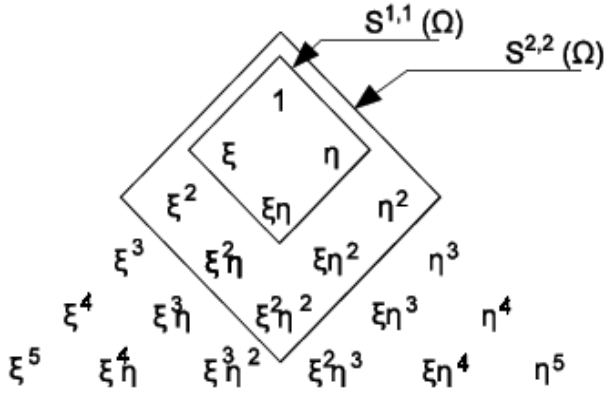


Figure 4.6 : "Lagrange" family

- Space $\tilde{S}^{p,q}(\Omega)$ or mixed family:

It is composed of all monomials common to $S^p(\Omega)$ and to $S^{p,q}(\Omega)$; formally $\tilde{S}^{p,q}(\Omega) = S^p(\Omega) \cap S^{p,q}(\Omega)$.

b) Quadrilateral p-element

A quadrilateral element has four corner nodes, four edges, and a face (Figure 4.7). Its shape functions are constructed by combining the one-dimensional shape functions in the two reference directions ξ and η, and are categorized into three groups, corresponding to the geometry of the element:

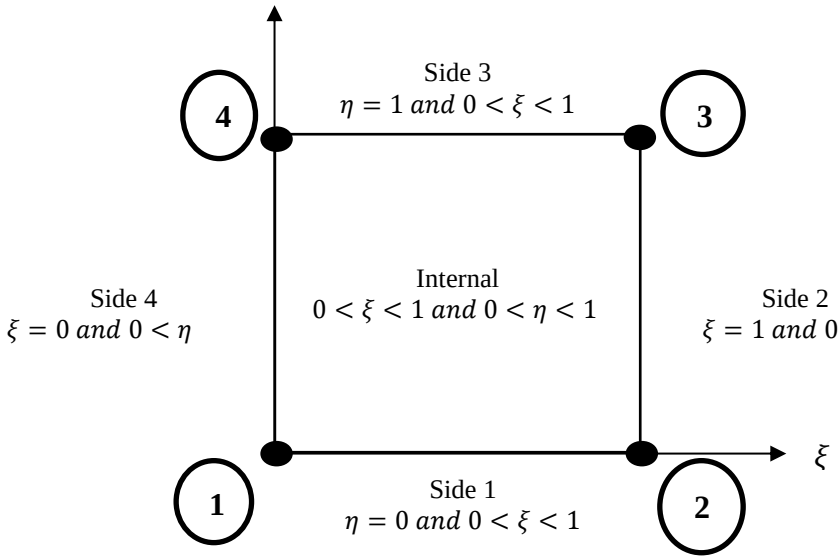


Figure 4.7 : Two-dimensional quadrilateral element

✓ Four shape functions of vertex

There are four bilinear shape functions that coincide with those of the standard four-node quadrilateral element. The corresponding degrees of freedom are the nodal displacements.

$$\text{Node 1}: \quad N^{n1}(\xi,\eta) = N_1(\xi)N_1(\eta) \tag{4.13.1}$$

$$\text{Node 2}: \quad N^{n2}(\xi,\eta) = N_2(\xi)N_1(\eta) \tag{4.13.2}$$

$$\text{Node 3}: \quad N^{n3}(\xi,\eta) = N_2(\xi)N_2(\eta) \tag{4.13.3}$$

$$\text{Node 4}: \quad N^{n4}(\xi,\eta) = N_1(\xi)N_2(\eta) \tag{4.13.4}$$

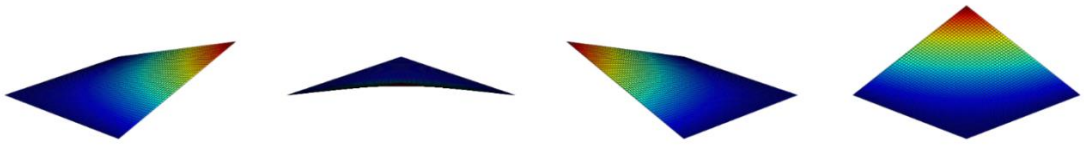


Figure 4.8 : Quadratic functions of the nodes.

✓ $(p-1)$ hierarchical shape functions defined on each side

$$\text{Side 1:} \quad N^{Side\ 1}(\xi,\eta) = N_1(\eta)N_{i+2}(\xi) \tag{4.14.1}$$

$$\text{Side 2:} \quad N^{Side\ 2}(\xi,\eta) = N_2(\xi)N_{i+2}(\eta) \tag{4.14.2}$$

Side 3: $N^{Side\ 3}(\xi,\eta) = N_2(\eta)N_{i+2}(\xi)$ (4.14.3)

Side 4: $N^{Side\ 4}(\xi,\eta) = N_1(\xi)N_{i+2}(\eta)$ (4.14.4)

With, $i = 1, \dots, p$

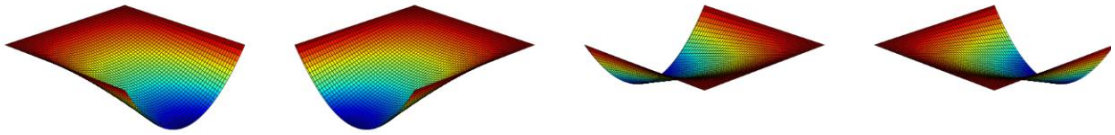


Figure 4.9 : Quadratic functions of the sides.

✓ $(p-1)^2$ internal hierarchical shape functions

$$N^{int}(\xi,\eta) = N_{i+2}(\xi)N_{j+2}(\eta) \quad (4.15)$$

With, $i,j = 1, \dots, p$; $i + j = 2, \dots, p$

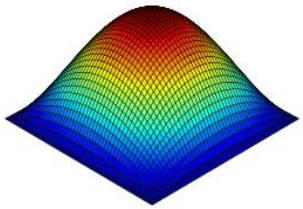


Figure 4.10 : Quadratic internal shape function.

The set of hierarchical shape functions for the quadrilateral element is presented in Figure 4.8.

c) Triangular p-element

The properties of shifted Legendre polynomials allow for the construction of hierarchical shape functions over a triangular domain defined on the interval [0,1] (see Figure 4.9)

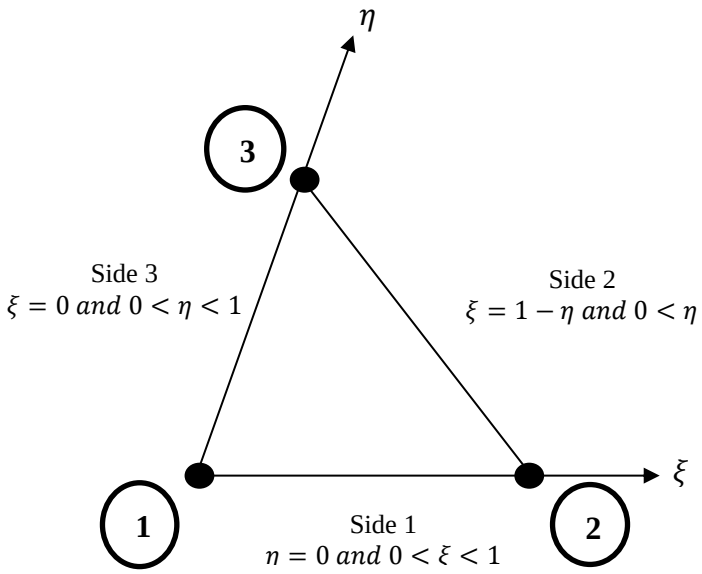


Figure 4.11 : Triangular p-element

Hierarchical shape functions can be classified into three categories:

- ✓ Three shape functions of vertex

Node 1 : $N^{n1}(\xi,\eta) = 1 - \xi - \eta$ (4.16.1)

Node 2 : $N^{n2}(\xi,\eta) = \xi$ (4.16.2)

Node 3 : $N^{n3}(\xi,\eta) = \eta$ (4.16.3)

- ✓ $(p-1)$ hierarchical shape functions defined on each side

Side 1: $N^{Side\ 1}(\xi,\eta) = \xi(1-\xi-\eta)P_i^*(\xi)$ (4.17.1)

Side 2: $N^{Side\ 2}(\xi,\eta) = \xi\eta P_i^*(\eta)$ (4.17.2)

Side 3: $N^{Side\ 3}(\xi,\eta) = \eta(1-\xi-\eta)P_i^*(\eta)$ (4.17.3)

With, $i = 1, \dots, p-2$

- ✓ $\frac{(p-1)(p-2)}{2}$ internal hierarchical shape functions

$$N^{int}(\xi,\eta) = \xi\eta(1-\xi-\eta)P_i^*(\xi)P_j^*(\eta) \quad (4.18)$$

With, $i = 0, \dots, p-3$; $j = p-i-3$

Chapter 5 Finite element formulation based on FSDT

Objective

In this chapter, the formulation of the problem using the Finite Element Method based on FSDT is presented. Starting with modeling the FGM sandwich plate. The second section, theoretical formulation is given including displacement fields, strain–displacement relations, stress–strain relations following by a detailed analysis is made of the introduction of the transverse shear correction factor in the formulation of thick plates. Then, the kinetic and strain energy of FGM sandwich plate and the equation of motion are given. In the last part, the numerical modeling approach based on rectangular p-elements, emphasizing the use of hierarchical shape functions for approximating displacement fields, along with the formulation of element mass and stiffness matrices essential for solving the governing equations. This framework forms the basis for analyzing the mechanical response of FG-CNT reinforced porous sandwich plates.

Moreover, this chapter presents the mathematical relations for incorporating the effects of porosity and carbon nanotubes (CNTs) reinforcement into the finite element modeling of FGM sandwich structures. Initially, it explores five distinct configurations of functionally graded materials (FGMs) affected by different porosity distributions (Imperfect I…, V). Subsequently, it describes the material properties of CNTs and provides their corresponding formulations for two reinforcement schemes, where the facesheets and the core are reinforced with various types of CNT distributions.

5.1. FGM sandwich plate model

Figure 5.1 shows rectangular sandwich plate made of FGM with a uniform thickness. It is positioned within a three-dimensional rectangular coordinate system (X, Y, Z). The top and bottom face sheets of sandwich plates are located at $z = \pm h/2$, with the bottom, two interface layers, and the top represented as $h_0,\ h_1,\ h_2, and\ h_3$ respectively ($h_0 = -h/2,\ h_3 = h/2$). The effective material properties of FGM layers, comprising, mass density $\rho^{(i)}(z)$, Poisson's ratio $\nu^{(i)}(z)$, and Young's modulus $E^{(i)}(z)$ are assumed to vary through the thickness following a power-law distribution, as presented by (Belalia 2017).

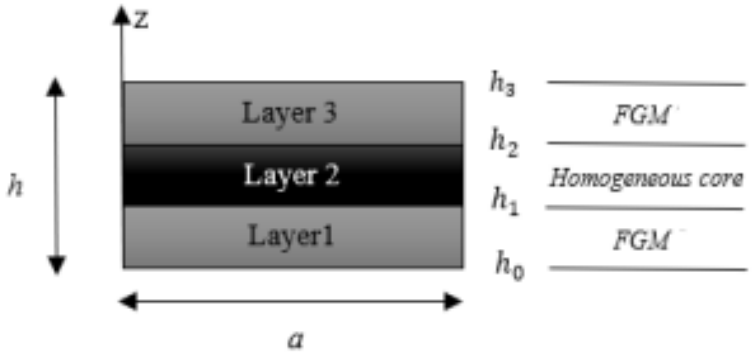


Figure 5.1: FGM plate model

$$E^{(i)}(z) = (E_c - E_m)V^{(i)}(z) + E_m \tag{5.1.1}$$

$$\nu^{(i)}(z) = (\nu_c - \nu_m)V^{(i)}(z) + \nu_c \tag{5.1.2}$$

$$\rho^{(i)}(z) = (\rho_c - \rho_m)V^{(i)}(z) + \rho_m \tag{5.1.3}$$

where (c) denotes ceramic and (m) refers to metal, respectively. $V^{(i)}(z)$ represents the volume fraction of the FGM sandwich for the i layer (with $i = 1,2,3$), and is taken to follow

$$V^{(1)}(z) = \left(\frac{z-h_0}{h_1-h_0}\right)^{n_1} \ , z \in [\,h_0, h_1] \tag{5.2.1}$$

$$V^{(2)}(z) = 1\ , \qquad z \in [\,h_1, h_2] \tag{5.2.2}$$

$$V^{(3)}(z) = \left(\frac{z-h_3}{h_2-h_3}\right)^{n_2} \ , z \in [\,h_2, h_3] \tag{5.2.3}$$

where n_1 and n_2 denote the volume fraction exponents of the bottom and top layers, respectively, $(0 \le n_1, n_2 \le +\infty)$.

5.2. Theoretical formulation

5.2.1. Displacement fields

In the first-order theory, the displacement field is expressed as (Mindlin 1951)]:

$$u = u_0(x, y, t) + z\theta_y(x, y, t) \tag{5.3.1}$$

$$v = v_0(x, y, t) - z\theta_x(x, y, t) \tag{5.3.2}$$

$$w = w_0(x, y, t) \tag{5.3.3}$$

This theory utilizes three displacement fields on the mid-surface ($u_0, v_0\ and\ w_0$ along with two rotational variables ($\theta_x\ and\ \theta_y$) to characterize the deformation. The rotational components correspond to transverse rotations perpendicular to the midplane in the directions of the x- and y-axes, respectively. The resulting displacement field is associated with deformations expressed in the form described [Bentrar et al. (2023)].

5.2.2. Strain–Displacement relations

The strain tensor is formulated using the partial derivatives of the displacement fields as follows:

$$\varepsilon_{ij} = \frac{1}{2}\left(\frac{\partial u_i}{\partial x_j} + \frac{\partial u_j}{\partial x_i}\right) \quad (i, j = 1, 2, 3) \tag{5.4}$$

where $u_1 = u, u_2 = v, u_3 = w, x_1 = x, x_2 = y, x_3 = z$

The correlation between strains and displacements, and curvatures–displacements based on linear elasticity theory for plates and under the assumptions of the FSDT, while neglecting ε_{zz} component (plane strain assumption), is given as follows:

$$\varepsilon_{xx} = \frac{\partial u}{\partial x} \tag{5.5}$$

$$\varepsilon_{yy} = \frac{\partial v}{\partial y} \tag{5.6}$$

$$\gamma_{xy} = \frac{\partial u}{\partial y} + \frac{\partial v}{\partial x} \tag{5.7}$$

$$\gamma_{xz} = \theta_y + \frac{\partial w}{\partial x} \tag{5.8}$$

$$\gamma_{yz} = -\theta_x + \frac{\partial w}{\partial y} \tag{5.9}$$

$$\chi_x = \frac{\partial \theta_y}{\partial x} \tag{5.10}$$

$$\chi_y = -\frac{\partial \theta_x}{\partial y} \tag{5.11}$$

$$\chi_{xy} = \frac{\partial \theta_y}{\partial y} - \frac{\partial \theta_x}{\partial x} \tag{5.12}$$

In vector form, these equations can be written:

$$\begin{Bmatrix} \varepsilon_{xx} \\ \varepsilon_{yy} \\ \gamma_{xy} \\ \gamma_{xz} \\ \gamma_{yz} \end{Bmatrix} = \begin{Bmatrix} 0 \\ 0 \\ 0 \\ \theta_y + \dfrac{\partial w}{\partial x} \\ -\theta_x + \dfrac{\partial w}{\partial y} \end{Bmatrix} + z \begin{Bmatrix} \dfrac{\partial \theta_y}{\partial x} \\ \dfrac{-\partial \theta_x}{\partial y} \\ \dfrac{\partial \theta_y}{\partial y} - \dfrac{\partial \theta_x}{\partial x} \\ 0 \\ 0 \end{Bmatrix} \tag{5.13}$$

It is evident to note that the strains ε_{xx}, ε_{yy} and γ_{xy} change linearly across the thickness of the plate, whereas shear strains γ_{xz} and γ_{yz} remain constant.

5.2.3. Stress–Strain relations

In accordance with Hooke's law, the linear elastic relationship between stresses and strains can be written in condensed form:

$$\{\sigma\} = [C]\{\varepsilon\} \tag{5.14}$$

Or in matrix form:

$$\begin{Bmatrix} \sigma_{xx} \\ \sigma_{yy} \\ \tau_{xy} \\ \tau_{xz} \\ \tau_{yz} \end{Bmatrix}^i = \begin{bmatrix} C_{11}^{(i)} & C_{12}^{(i)} & 0 & 0 & 0 \\ C_{12}^{(i)} & C_{22}^{(i)} & 0 & 0 & 0 \\ 0 & 0 & C_{66}^{(i)} & 0 & 0 \\ 0 & 0 & 0 & C_{44}^{(i)} & 0 \\ 0 & 0 & 0 & 0 & C_{55}^{(i)} \end{bmatrix}^i \begin{Bmatrix} \varepsilon_{xx} \\ \varepsilon_{yy} \\ \gamma_{xy} \\ \gamma_{xz} \\ \gamma_{yz} \end{Bmatrix}^i \tag{5.15}$$

Where $(\sigma_{xx}, \sigma_{yy}, \tau_{xy}, \tau_{xz}, \tau_{yz})$ and $(\varepsilon_{xx}, \varepsilon_{yy}, \gamma_{xy}, \gamma_{xz}, \gamma_{yz})$ denote the stress and strain components, respectively. The elasticity constants $C_{jk}^{(i)}$ are defined in terms of the effective material properties namely, the Young's modulus and Poisson's ratio, are expressed as follows:

$$C_{11}^{(i)} = C_{22}^{(i)} = \frac{E^{(i)}(z)}{1 - \left(\nu^{(i)}(z)\right)^2} \tag{5.16.1}$$

$$C_{12}^{(i)} = \nu^{(i)}(z) C_{11}^{(i)} \tag{5.16.2}$$

$$C_{44}^{(i)} = C_{55}^{(i)} = C_{66}^{(i)} = \frac{E^{(i)}(z)}{2\left(1 + \left(\nu^{(i)}(z)\right)\right)} \tag{5.16.3}$$

The stiffness coefficients corresponding to CNT-reinforced core are defined as [Dat et al. (2022)]

$$C_{11}^C = \frac{E_{11}}{1 - \nu_{12}\nu_{21}}, C_{22}^C = \frac{E_{22}}{1 - \nu_{12}\nu_{21}}, C_{12}^C = \frac{\nu_{21} E_{22}}{1 - \nu_{12}\nu_{21}} \tag{5.17.1}$$

$$C_{44}^C = G_{23}, C_{55}^C = G_{13}, C_{55}^C = G_{12} \tag{5.17.2}$$

5.2.4. Transverse shear correction factors

Mindlin (1951) showed that, for an isotropic plate, the shear correction factor depends on Poisson's ratio and can range from $k = 0.76$ for $\nu = 0$ to $k = 0.91$ for $\nu = 0.5$. Following Mindlin suggestion, the shear correction factor is given by the following cubic equation [Liew, K.M., Wang, C.M., Xiang, Y., and Kitipornchai, S. (1998)]

$$k^3 - 8k^2 + \frac{8(2-\nu)k}{1-\nu} + \frac{8}{1-\nu} = 0 \tag{5.18}$$

For example, when $\nu = 0.3$, the shear correction factor is $k = 0.86$, and when $\nu = 0.176$, it becomes $k = \frac{\pi^2}{12}$.

On the other hand, Reissner (1945) , who assumed a parabolic distribution of shear stress distribution across the plate thickness, showed that the corresponding shear correction factor takes the following value:

$$k = \frac{5}{6} \tag{5.19}$$

Based on exact three-dimensional analytical solution for the vibration of simply supported isotropic rectangular plates, Wittrick (1987) calibrated the shear correction factor in Mindlin's theory and proposed the following expression for it:

$$k = \frac{5}{6-\nu} \tag{5.20}$$

Wittrick's shear correction factor yields a value of 0.877 for Poisson's ratio ν = 0.3, which closely matches the value of 0.88 previously reported by Srinivas et Rao (1970) and Dawe (1978). It appears that Wittrick's correction factor is the most accurate to date, as it combines a simple analytical form with consideration of the Poisson's ratio effect.

5.2.5. Kinetic and Strain energy of FGM sandwich plate

The strain energy functional U of a moderately thick FG plate is given by:

$$U = \frac{1}{2}\int_V \{\sigma\}^T\{\varepsilon\}\, dV \tag{5.21}$$

Equation (5.21), when expressed in its expanded form, is written as follows:

$$U = \frac{1}{2}\iint \left[\left(A_{11}\varepsilon_{xx}^2 + A_{22}\varepsilon_{yy}^2 + 2A_{12}\varepsilon_{xx}\varepsilon_{yy} + A_{66}\gamma_{xy}^2\right) + \left(D_{11}\chi_x^2 + D_{22}\chi_y^2 + 2D_{12}\chi_x\chi_y + D_{66}\chi_{xy}^2\right) + \left(S_{44}\gamma_{xz}^2 + S_{55}\gamma_{yz}^2\right)\right]dxdy \tag{5.22}$$

The kinetic energy is described as

$$T = \iint \left[I_1 \left(\left(\frac{\partial u}{\partial t}\right)^2 + \left(\frac{\partial v}{\partial t}\right)^2 + \left(\frac{\partial w}{\partial t}\right)^2 \right) + I_3 \left(\left(\frac{\partial \theta_x}{\partial t}\right)^2 + \left(\frac{\partial \theta_y}{\partial t}\right)^2 \right) \right] dxdy \quad (5.23)$$

where A_{ij}, D_{ij}, and S_{ij} represent the extensional, bending, shear stiffness constants, and (I_1, I_3) are the inertia constants of the FGM plate. They are expressed, respectively, as

$$\left(A_{ij}, D_{ij}\right) = \int_{-h/2}^{h/2} C_{ij}\,(1, z^2) dz \;\; (i,j = 1,2,6) \quad (5.24.1)$$

$$\left(S_{ij}\right) = k \int_{-h/2}^{h/2} C_{ij}\, dz \;\; (i,j = 4,5) \quad (5.24.2)$$

$$(I_1, I_3) = \int_{-h/2}^{h/2} \rho(z)\,(1, z^2) dz \quad (5.24.3)$$

where k is a shear correction factor of FSDT ($k = 5/6$) [Szilard 2004].

5.2.6. Equation of motion

Using the Lagrangian function expressed as the difference between the kinetic energy and the strain energy, it is given by:

$$L = T - U \quad (5.25)$$

The above function allows deriving the equations of motion of plate by applying Lagrange's formula

$$\frac{\partial}{\partial t}\left(\frac{\partial T}{\partial \{\dot{q}_i\}}\right) - \left(\frac{\partial T}{\partial \{q_i\}}\right) + \frac{\partial V}{\partial \{q_i\}} = 0 \quad (5.26)$$

From equation (5.26), the mass and stiffness matrices are derived

$$\frac{\partial}{\partial t}\left(\frac{\partial T}{\partial \{\dot{q}_i\}}\right) - \left(\frac{\partial T}{\partial \{q_i\}}\right) = [M]\{\ddot{q}\} \quad (5.27.1)$$

$$\frac{\partial V}{\partial \{q_i\}} = [K]\{q\} \quad (5.27.2)$$

The following equation of motion is obtained

$$[K]\{Q\} + [M]\{\ddot{Q}\} = 0 \quad (5.28)$$

The substitution of $\{\ddot{Q}\} = -\omega^2\{Q\}$ into the above equation yields:

$$[-\omega^2 M + K]\{Q\} = 0 \quad (5.29)$$

where $\{Q\} = \left\{ Q_w \; Q_{\theta_x} \; Q_{\theta_y} \right\}$ is defined as the vector of generalized amplitudes.

5.3. Modeling using rectangular p-element

A four-node rectangular finite element, formulated based on the FSDT and incorporating three degrees of freedom by node, was employed to analyze the free vibration, static and dynamic behavior of the FGM sandwich plate.

5.3.1. Displacement field approximation and shape functions

With the p-FEM approach, the in-plane displacements (u, v) and out-of-plane displacements(w, θ_x, θ_y), are expressed as follows:

$$\begin{Bmatrix} u \\ v \end{Bmatrix} = \sum_{j=1}^{(p+1)^2} \bar{N}_j \, \bar{q}_j \tag{5.30}$$

where

$$\bar{N}_j = \begin{bmatrix} N(\xi,\eta) & 0 \\ 0 & N(\xi,\eta) \end{bmatrix}, \text{ and } \qquad \bar{q}_j = \begin{Bmatrix} \bar{q}_{2j-1} \\ \bar{q}_{2j} \end{Bmatrix} \tag{5.31}$$

and

$$\begin{Bmatrix} w \\ \theta_x \\ \theta_y \end{Bmatrix} = \sum_{j=1}^{(p+1)^2} N_j \, q_j \tag{5.32}$$

where

$$N_j = \begin{bmatrix} N(\xi,\eta) & 0 & 0 \\ 0 & N(\xi,\eta) & 0 \\ 0 & 0 & N(\xi,\eta) \end{bmatrix}, \text{ and } \qquad q_j = \begin{Bmatrix} q_{3j-2} \\ q_{3j-1} \\ q_{3j} \end{Bmatrix} \tag{5.33}$$

Where, p denotes the degree of the interpolation polynomial $\bar{q}_j$ is the vector of generalized in-plane displacements, q_j is the vector comprising generalized transverse displacements and rotations $N(\xi,\eta)$ associated with the shape functions of the rectangular finite *p*-element. In p-element, the shape functions are categorized into vertex, side, and internal functions to enable higher-order approximations, the shape functions employed in the present p-element formulation are defined as follows:

- ✓ Four shape functions of vertex

$$\text{Node 1}: \quad N^{n1}(\xi,\eta) = N_1(\xi)N_1(\eta) \tag{5.34.1}$$

$$\text{Node 2}: \quad N^{n2}(\xi,\eta) = N_2(\xi)N_1(\eta) \tag{5.34.2}$$

$$\text{Node 3}: \quad N^{n3}(\xi,\eta) = N_2(\xi)N_2(\eta) \tag{5.34.3}$$

$$\text{Node 4}: \quad N^{n4}(\xi,\eta) = N_1(\xi)N_2(\eta) \tag{5.34.4}$$

- ✓ $(p-1)$ hierarchical shape functions on each side

$$\text{Side 1}: \quad N^{Side\ 1}(\xi,\eta) = N_1(\eta)N_{i+2}(\xi) \tag{5.35.1}$$

$$\text{Side 2}: \quad N^{Side\ 2}(\xi,\eta) = N_2(\xi)N_{i+2}(\eta) \tag{5.35.2}$$

$$\text{Side 3}: \quad N^{Side\ 3}(\xi,\eta) = N_2(\eta)N_{i+2}(\xi) \tag{5.35.3}$$

$$\text{Side 4}: \quad N^{Side\ 4}(\xi,\eta) = N_1(\xi)N_{i+2}(\eta) \tag{5.35.4}$$

where, $i = 1, \ldots, p$

✓ $(p-1)^2$ internal hierarchical shape functions

$$N^{int}(\xi,\eta) = N_{i+2}(\xi)N_{j+2}(\eta) \tag{5.36}$$

where, $i,j = 1,\dots,p\ ;\ i+j = 2,\dots,p$

where $N_1(\xi)$, $N_1(\eta)$ represent the one-dimensional hierarchical shape functions and are expressed as

$$N_1(\xi) = 1-\xi,\ N_2(\xi) = \xi,\ N_{i+1}(\xi) = \sqrt{2i-1}\int_0^{\xi} P_{i-1}(\tau)\,d\tau\ ,\ i \geq 2 \tag{5.37.1}$$

$$N_1(\eta) = 1-\eta,\ N_2(\eta) = \eta,\ N_{i+1}(\eta) = \sqrt{2i-1}\int_0^{\eta} P_{i-1}(\tau)\,d\tau\ ,\ i \geq 2 \tag{5.37.2}$$

where $P_i(\tau)$ indicates the shifted Legendre polynomials, given by:

$$P_0(\tau) = 1,\ P_1(\tau) = 2\tau - 1 \tag{5.38.1}$$

$$P_{j+1}(\tau) = \frac{1}{j+1}\left[(-2j-1+(4j+2)j)P_j(\tau) - jP_{j-1}(\tau)\right],\ j = 1,2,\dots \tag{5.38.2}$$

5.3.2. Mass and Stiffness matrices

The element mass $[M]$, and element stiffness matrices $[K]$ are provided, respectively, as

$$[M] = \int_0^1\int_0^1 \begin{bmatrix} I_1N_iN_j & 0 & 0 \\ 0 & I_3N_iN_j & 0 \\ 0 & 0 & I_3N_iN_j \end{bmatrix} abd\xi d\eta \tag{5.39}$$

$$[K] = \int_0^1\int_0^1 \begin{bmatrix} S_{44}\frac{\partial N_i}{\partial \xi}\frac{\partial N_j}{\partial \xi} + S_{55}\frac{\partial N_i}{\partial \eta}\frac{\partial N_j}{\partial \eta}, & -S_{44}\frac{\partial N_i}{\partial \eta}N_j, & S_{55}\frac{\partial N_i}{\partial \xi}N_j \\ -S_{44}N_i\frac{\partial N_j}{\partial \eta}, & D_{66}\frac{\partial N_i}{\partial \xi}\frac{\partial N_j}{\partial \xi} + D_{22}\frac{\partial N_i}{\partial \eta}\frac{\partial N_j}{\partial \eta} + S_{44}N_iN_j, & -D_{12}\frac{\partial N_i}{\partial \eta}\frac{\partial N_j}{\partial \xi} - D_{66}\frac{\partial N_i}{\partial \xi}\frac{\partial N_j}{\partial \eta} \\ S_{55}N_i\frac{\partial N_j}{\partial \xi}, & -D_{12}\frac{\partial N_i}{\partial \xi}\frac{\partial N_j}{\partial \eta} - D_{66}\frac{\partial N_i}{\partial \eta}\frac{\partial N_j}{\partial \xi}, & D_{66}\frac{\partial N_i}{\partial \eta}\frac{\partial N_j}{\partial \eta} + D_{11}\frac{\partial N_i}{\partial \xi}\frac{\partial N_j}{\partial \xi} + S_{55}N_iN_j \end{bmatrix} abd\xi d\eta \tag{5.40}$$

Where the local-to-global coordinate transformation is defined by the corresponding matrix [Belalia (2017)]

$$\begin{Bmatrix}\xi\\ \eta\\ \zeta\end{Bmatrix} = \begin{bmatrix} 1/a & 0 & 0 \\ 0 & 1/b & 0 \\ 0 & 0 & 2/h \end{bmatrix}\begin{Bmatrix}x\\ y\\ z\end{Bmatrix} \tag{5.41}$$

5.4. Porous FGM sandwich plate reinforced with CNT

5.4.1. Porosity-dependent FG sandwich plates

Several schemes have been reported in the literature to describe porosity distribution for determining the constitutive material properties of porous FG plates, as presented in Figure 5.2.

In the current study, porosity is assumed to be independently distributed within each FG layer of the FGM sandwich plate. Five porosity distribution are considered [Bentrar et al. (2023)]:

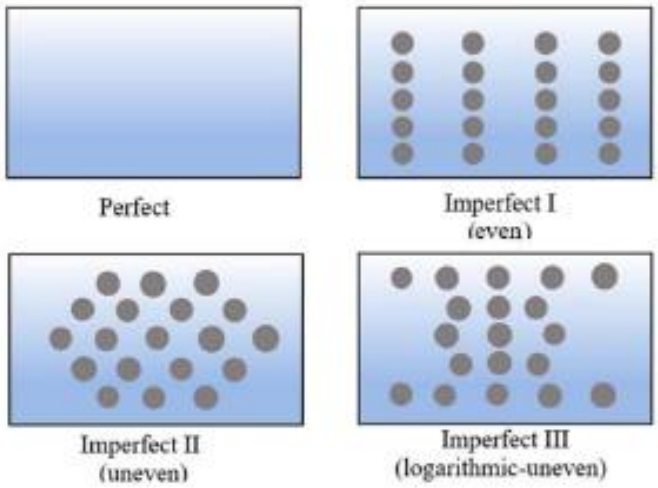


Figure 5.2 : Types of porosity distribution.

5.4.1.1 Imperfect I- FGM (even)

In this model, porosities are assumed to be uniformly distributed throughout the FGM sandwich layers, while the core remains free of porosity. Referred to as the Imperfect I model, the overall material properties $P^{(l)}$ of each FGM layer l ($l = 1, 2, 3$) are defined as:

$$\begin{cases} P^1(z) = P_m + (P_c - P_m)V^{(1)}(z) - \dfrac{e_1}{2}(P_c + P_m) \\ P^2(z) = P_m + (P_c - P_m)V^{(2)}(z) \\ P^3(z) = P_m + (P_c - P_m)V^{(3)}(z) - \dfrac{e_2}{2}(P_c + P_m) \end{cases} \tag{5.32}$$

P_m and P_c denote material properties of the metal and ceramic constituents, respectively, while e represents porosity coefficient ($e << 1$). For a non-porous FGM sandwich plate, the porosity parameters are taken as $e_1 = e_2 = e = 0$.

5.4.1.2 Imperfect II- FGM (uneven)

Porosity within the FG sandwich plate can exhibit a gradual variation across its thickness, as shown below

$$\begin{cases} P^1(z) = P_m + (P_c - P_m)V^{(1)}(z) - \dfrac{e_1}{2}(P_c + P_m)\left[1 - \dfrac{|2z - (h_0 + h_1)|}{h_1 - h_0}\right] \\ P^2(z) = P_m + (P_c - P_m)V^{(2)}(z) \\ P^3(z) = P_m + (P_c - P_m)V^{(3)}(z) - \dfrac{e_2}{2}(P_c + P_m)\left[1 - \dfrac{|2z - (h_3 + h_2)|}{h_3 - h_2}\right] \end{cases} \tag{5.33}$$

5.4.1.3 Imperfect III- FGM (logarithmic-uneven)

The third porosity distribution model is employed a logarithmic function, which is defined as

$$\begin{cases} P^1(z) = P_m + (P_c - P_m)V^{(1)}(z) - \log\left(1 + \frac{e_1}{2}\right)(P_c + P_m)\left[1 - \frac{|2z - (h_0 + h_1)|}{h_1 - h_0}\right] \\ P^2(z) = P_m + (P_c - P_m)V^{(2)}(z) \\ P^3(z) = P_m + (P_c - P_m)V^{(3)}(z) - \log\left(1 + \frac{e_2}{2}\right)(P_c + P_m)\left[1 - \frac{|2z - (h_3 + h_2)|}{h_3 - h_2}\right] \end{cases} \quad (5.34)$$

5.4.1.4 Imperfect IV-FGM (linear-uneven)

This porosity model assumes that the porosity density varies linearly through the FGM layers, reaching its minimum at the outer surfaces of the sandwich plate and its maximum at the interfaces between layers.

$$\begin{cases} P^1(z) = P_m + (P_c - P_m)V^{(1)}(z) - \frac{e_1}{2}(P_c + P_m)\left[1 - \frac{z - h_1}{h_0 - h_1}\right] \\ P^2(z) = P_m + (P_c - P_m)V^{(2)}(z) \\ P^3(z) = P_m + (P_c - P_m)V^{(3)}(z) - \frac{e_2}{2}(P_c + P_m)\left[1 - \frac{z + h_3}{h_2 - h_3}\right] \end{cases} \quad (5.35)$$

5.4.1.5 Imperfect V-FGM (sinusoidal -uneven)

The fifth porosity distribution model is defined by a sinusoidal function and is mathematically expressed as follows.

$$\begin{cases} P^1(z) = P_m + (P_c - P_m)V^{(1)}(z) - \frac{e_1}{2}\sin\left(\frac{\pi}{4} + \frac{zh}{2}\right)(P_c + P_m)\left[1 - \frac{|2z - (h_0 + h_1)|}{h_1 - h_0}\right] \\ P^2(z) = P_m + (P_c - P_m)V^{(2)}(z) \\ P^3(z) = P_m + (P_c - P_m)V^{(3)}(z) - \frac{e_2}{2}\sin\left(\frac{\pi}{4} + \frac{zh}{2}\right)(P_c + P_m)\left[1 - \frac{|2z - (h_3 + h_2)|}{h_3 - h_2}\right] \end{cases} \quad (5.36)$$

5.5. Material properties of CNTs

As illustrated in figures 5.3 and 5.4, the structure under consideration is a composite plate of uniform thickness, composed of three non-homogeneous material layers, defined within a cartesian coordinate system (x, y, z). The plate has length ‘a’, width ‘b’, and total thickness ‘h’. The bottom and top surfaces of the sandwich plate are positioned at $z = \pm h/2$, respectively. The multilayer configuration comprises three elastic layers, designated as layers 1, 2, and 3, arranged from bottom to top. Their corresponding thickness positions are given as $h_0 = -h/2, h_1, h_2, and\ h_3 = h/2$.

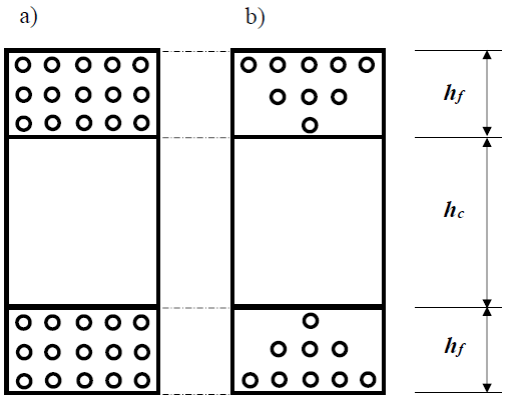


Figure 5.3 : Geometries of face-sheets reinforced sandwich plate: a) Uniform distribution, b) FG-CNT distribution.

As shown in figure 5.3, the face-sheet layers are assumed to be reinforced with carbon nanotubes (CNTs) exhibiting two distinct through-thickness distribution patterns. The uniformly distributed CNT (UD-CNT) configuration represents a constant CNT volume fraction throughout the thickness, whereas the functionally graded CNT (FG-CNT) configuration involves a variable CNT volume fraction that changes along the thickness direction. In both reinforcement schemes, the CNT distribution is considered homogeneous in the in-plane directions, with variation occurring exclusively through the thickness.

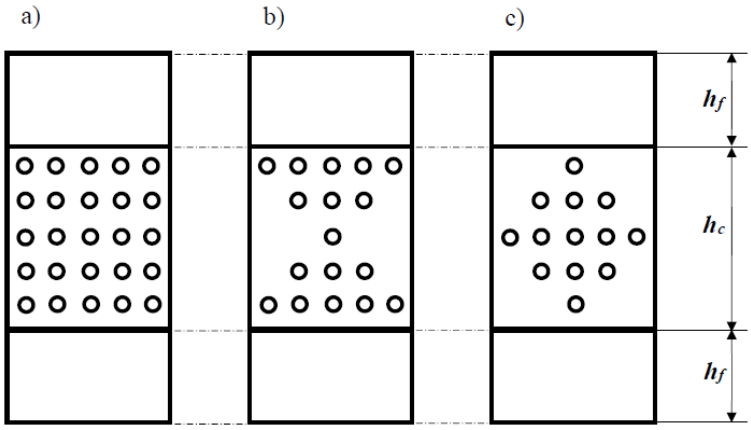


Figure 5.4 : Geometries of core reinforced sandwich plate: a) Uniform distribution, b) FG-X distribution, c) FG-O distribution.

For the core layer as presented in figure 5.4, three types of carbon nanotube (CNT) distribution models are investigated: the uniform distribution model (UD-CNT), the functionally graded X-direction model (FG-X), and the functionally graded O-direction model (FG-O). The material characteristics of the carbon nanotube-reinforced composite (CNTRC), composed of CNTs embedded in an isotropic polymer matrix, are evaluated using the rule of mixtures, as outlined by Draoui et al. (2019). In this analysis, CNT efficiency parameters

(η_1, η_2, η_3) are introduced to account for the scale-dependent reinforcement effects. The mechanical properties of CNTRC layer, such as Young's modulus and shear modulus, are calculated using the following expressions

$$E_{11} = \eta_1 V_{CNT} E_{11}^{CNT} + V_m E^m \tag{5.37}$$

$$\frac{\eta_2}{E_{22}} = \frac{V_{CNT}^*}{E_{22}^{CNT}} + \frac{V^m}{E_{22}^m} \tag{5.38}$$

$$\frac{\eta_3}{G_{12}} = \frac{V_{CNT}}{G_{12}^{CNT}} + \frac{V^m}{G^m} \tag{5.39}$$

$$G_{13} = G_{12} \tag{5.40}$$

$$G_{23} = 1.2\, G_{12} \tag{5.41}$$

where $E_{11}^{CNT}, E_{22}^{CNT} and\ G_{12}$ represent Young's modulus and shear modulus of CNTs, in the given order. E^m and G^m refer to Young's modulus and shear modulus of the polymer matrix and are illustrated in Table 5.1. V_{CNT} and V^m denote the volume fractions of CNTs and matrix, respectively. These volume fractions satisfy the following relation:

$$V_{CNT} + V^m = 1 \tag{5.42}$$

The material properties, including mass density (ρ) and Poisson's ratio (ν), are given as follows:

$$\nu_{12} = V_{CNT}^* \nu_{12}^{CNT} + V_m \nu^m \tag{5.43}$$

$$\nu_{21} = \frac{E_{22}}{E_{11}} \nu_{12} \tag{5.44}$$

$$\rho = V_{CNT} \rho^{CNT} + V_m \rho^m \tag{5.45}$$

The volume fraction exponent in the two sandwich plates is defined as a function characterizing the distribution of aligned carbon nanotubes across the thickness direction.

- ✓ For a sandwich plate reinforced with top and bottom face sheets, the reinforcement is applied on both external layers to enhance structural performance

Face sheet UD-CNT
$$V_{CNT}(z) = \begin{cases} V_{CNT}^* & z \in [\, h_0, h_1] \\ 0 & z \in [\, h_1, h_2] \\ V_{CNT}^* & z \in [\, h_2, h_3] \end{cases} \tag{5.46.1}$$

Face sheet FG-CNT
$$V_{CNT}(z) = \begin{cases} \left(\frac{z-h_1}{h_0-h_1}\right) 2V_{CNT}^* & z \in [\, h_0, h_1] \\ 0 & z \in [\, h_1, h_2] \\ \left(\frac{h_2-z}{h_2-h_3}\right) 2V_{CNT}^* & z \in [\, h_2, h_3] \end{cases} \tag{5.54.2}$$

- ✓ For a sandwich plate with a reinforced core

Core UD-CNT
$$V_{CNT}(z) = \begin{cases} 0 & z \in [h_0, h_1] \\ V_{CNT}^* & z \in [h_1, h_2] \\ 0 & z \in [h_2, h_3] \end{cases} \quad (5.47.1)$$

Core FG-X CNT
$$V_{CNT}(z) = \begin{cases} 0 & z \in [h_0, h_1] \\ 4\frac{|z|}{h_c} V_{CNT}^* & z \in [h_1, h_2] \\ 0 & z \in [h_2, h_3] \end{cases} \quad (5.55.2)$$

Core FG-O CNT
$$V_{CNT}(z) = \begin{cases} 0 & z \in [h_0, h_1] \\ \left(2 - 4\frac{|z|}{h_c}\right) V_{CNT}^* & z \in [h_1, h_2] \\ 0 & z \in [h_2, h_3] \end{cases} \quad (5.55.3)$$

Where V_{CNT}^* denotes the specified volume fraction of CNTs, which is calculated using the expression:

$$V_{CNT}^* = \frac{W_{CNT}}{W_{CNT} + \frac{\rho^{CNT}}{\rho^m} - \frac{\rho^{CNT}}{\rho^m} W_{CNT}} \quad (5.48)$$

Where W_{CNT} represents the mass fraction of CNTs in the nanocomposite plate. In the present study, the efficiency parameters of CNTs (η) associated with the specified volume fraction η are adopted based on the works [Draoui et al. (2019), Bidgoli et Arefi (2023)], and are illustrated in Table 5.2.

Table 5.1 : Mechanical properties of CNTs and matrix materials

Material	$E_{11}(GPa)$	$E_{22}(GPa)$	$G_{12}(GPa)$	ν_{12}	$\rho(kg/m^3)$
CNTs	5646.6	7080	1944.5	0.175	1400
PmPV(M2)	2.1	2.1	0.7835	0.34	1150

Table 5.2: CNT efficiency parameter

V_{CNT}^*	**0.12**	**0.17**	**0.28**
η_1	0.137	0.142	0.141
η_2	1.002	1.626	1.585
η_3	0.715	1.138	1.109

Chapter 6 Programming Techniques

Objective

This chapter presents the implementation of the mathematical formulas obtained above in calculation codes written in Fortran 90 language. The developed code is used to determine frequencies, modes, central deflection and dynamic response of rectangular sandwich FGM plates with porosity reinforced with CNTs. A description includes the software and hardware used, flowchart, subroutines, data file and output file.

6.1. Software and hardware used

The programming was carried out using FORTRAN, a language whose name originates from *The IBM Mathematical Formula Translating System*. It is a general-purpose imperative language, specifically optimized for numerical and scientific computations. FORTRAN was developed by IBM in the 1950 in California, USA, and has undergone many versions over time.

- In this study, **FORTRAN90** is used. It is a scientific programming language that is particularly well suited for the finite element method.
- The commercial software **MATLAB** is an interactive scientific programming system for numerical computation and graphical visualization. It is based on a matrix representation of data, from which its name **Matrix Laboratory** is derived. In this study, MATLAB is additionally employed to perform **symbolic calculations** of shape functions and their derivatives.
- **Origin 9.5** was employed for **plotting curves** and **graphical visualization** of the results.
- Additionally, **Python 3.13** was used to **visualize the functions**.

The computations were performed on a PC featuring a Core i5 processor (2.40 GHz) and 8 GB of RAM.

6.2. Flowchart of the program

Figure 6.1 presents the various steps involved in the developed program.

6.3. Program description

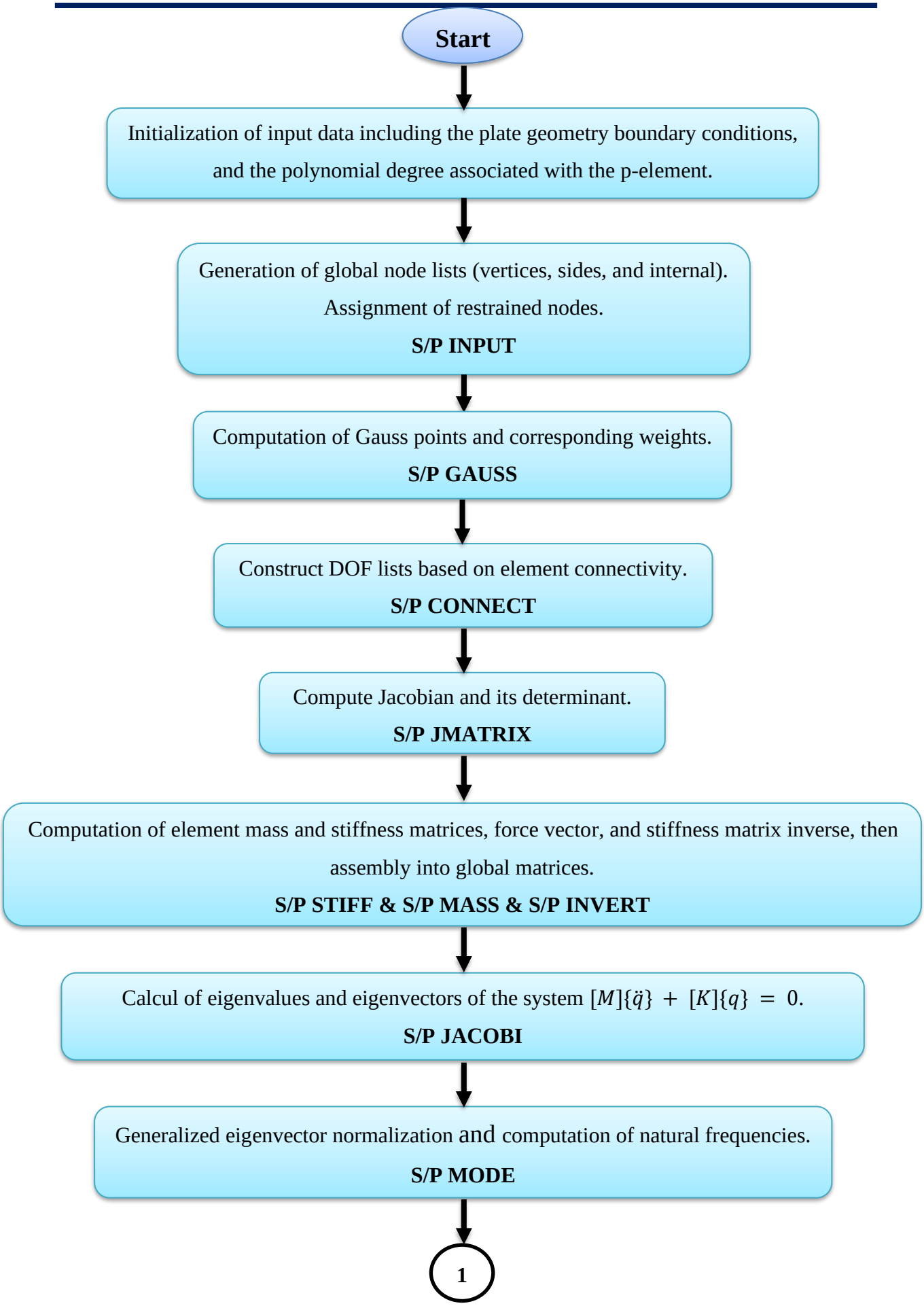
6.3.1. Data file

The data file (S/P INPUT) contains all the necessary information for running the program, including element parameters, physical properties, geometrical data, and loading Conditions (Static and Dynamic)

6.3.1.1 Element parameters

The p-element parameters stored in the data file include:

- NTE: Total number of elements.
- NTN: Total number of nodes.
- NTC: Total number of sides.
- NNR: Number of restrained nodes.
- NCR: Number of restrained sides.
- LL(J) : Element connectivity.


Start
Initialization of input data including the plate geometry boundary conditions, and the polynomial degree associated with the p-element.
Generation of global node lists (vertices, sides, and internal). Assignment of restrained nodes.
S/P INPUT
Computation of Gauss points and corresponding weights.
S/P GAUSS
Construct DOF lists based on element connectivity.
S/P CONNECT
Compute Jacobian and its determinant.
S/P JMATRIX
Computation of element mass and stiffness matrices, force vector, and stiffness matrix inverse, then assembly into global matrices.
S/P STIFF & S/P MASS & S/P INVERT
Calcul of eigenvalues and eigenvectors of the system $[M]\{\ddot{q}\} + [K]\{q\} = 0$.
S/P JACOBI
Generalized eigenvector normalization and computation of natural frequencies.
S/P MODE
1

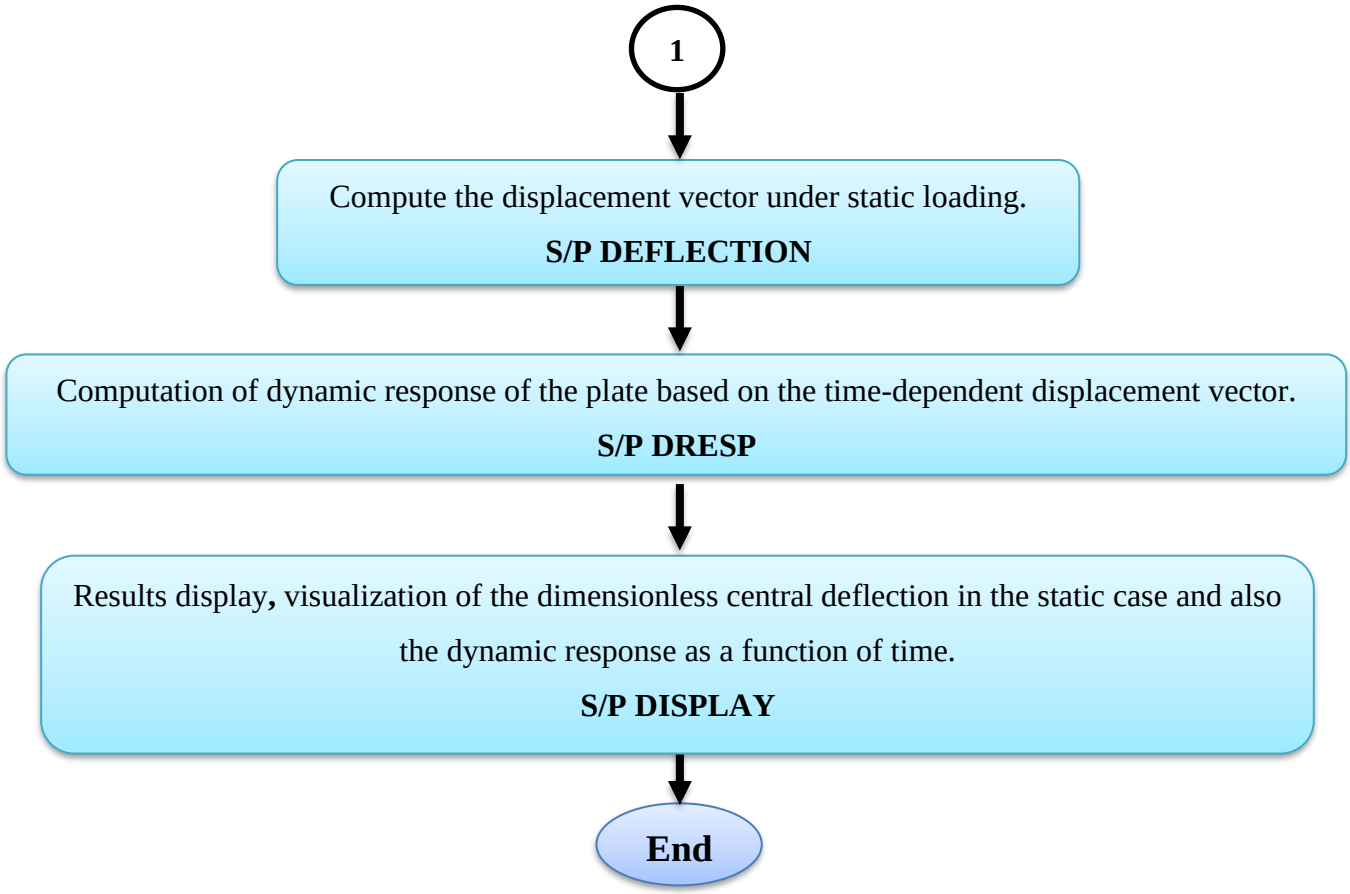


Figure 6.1: Flowchart of the program.

- LNR : Restricted nodes.
- LCR : Restricted sides.
- NMH: Degree of p-element polynomial.
- NMODE : Specific mode number.
- NND: Number of nodes where displacements are calculated.
- NNC: Number of nodes loaded.

6.3.1.2 Physical parameters

The program incorporates the following physical parameters for analysis:

- PRm: Poisson's ratio of the metal.
- PRc: Poisson's ratio of the ceramic.
- SC: Shear correction factor.
- Em: Young's modulus of the metal.
- Ec: Young's modulus of the ceramic.
- ROm: Surface mass density of the metal.
- ROc: Surface mass density of the ceramic.

- EN1: Volume fraction (bottom layer).
- EN2: volume fraction (top layer).
- XCI1: Porosity coefficient (bottom layer).
- XCI2: Porosity coefficient (top layer).

6.3.1.3 Geometric parameters

The geometric parameters of plate are presented as follows:

- H : Plate thickness.
- X(i), Y(i): Coordinates of the nodes located at vertices of the elements.

6.3.1.4 Loading Conditions (Static and Dynamic)

- ILOAD : Type of load.
- C_0: Value of applied load.
- DR : Damping coefficient.
- DT : Time increment.

6.3.1.5 Boundary conditions

To facilitate the resolution of generalized eigenvalue problem, it is crucial to consider the boundary conditions. Solving the system of equations only requires to substitute prescribed (zero) displacements at boundary nodes directly into the system equations. The quadrilateral p-element, as illustrated in Figure 6.2, consists of four corner nodes and four edges. Each node possesses three degrees of freedom

- w: The displacement along the **z-axis.**
- θ_x: The rotation of the cross-section around the **x-axis.**
- θ_y: The rotation of the cross-section around the **y-axis.**

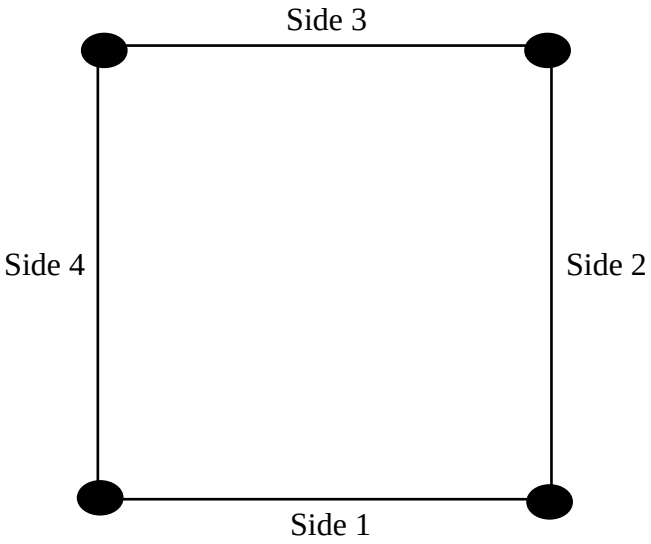


Figure 6.2 : Numbering of nodes and sides of the p-element.

Table 6.1 : Node boundary conditions

Node	u	v	w	θ_x	θ_y
1	1 or 0	1 or 0	1 or 0	1 or 0	1 or 0
2	1 or 0	1 or 0	1 or 0	1 or 0	1 or 0
3	1 or 0	1 or 0	1 or 0	1 or 0	1 or 0
4	1 or 0	1 or 0	1 or 0	1 or 0	1 or 0

Table 6.2 : Side boundary conditions

Side	u	v	w	θ_x	θ_y
1	1 or 0	1 or 0	1 or 0	1 or 0	1 or 0
2	1 or 0	1 or 0	1 or 0	1 or 0	1 or 0
3	1 or 0	1 or 0	1 or 0	1 or 0	1 or 0
4	1 or 0	1 or 0	1 or 0	1 or 0	1 or 0

6.3.2. Programming

The computational program developed in this study enables the analysis of linear free vibration, static, and dynamic analysis of FGM sandwich plates utilizing quadrilateral p-element. This approach facilitates the determination of natural frequencies and corresponding eigenvectors, central deflection in both static and dynamic response. The flowchart presented in figure 6.1 outlines the main subroutines and key development stages of the program. The following subroutines are considered fundamental for executing the computational procedure:

6.3.2.1 Subroutine PROMAT

In the formulation of FG-CNTR porous sandwich plate, the elasticity constants provided in Equations Chapter 5 depend on the effective material properties. The corresponding constants are computed in the subroutine PROMAT using numerical integration.

6.3.2.2 Subroutine JMATRIX

The JMATRIX subroutine computes both the determinant and the constituents of the Jacobian matrix, which are essential for evaluating the element stiffness and mass matrices.

6.3.2.3 Subroutine GAUSS

Using Gauss–Legendre quadrature, the integrals involved in the computation of the element stiffness and mass matrices are evaluated numerically due to the impossibility of obtaining analytical solutions. The GAUSS subroutine computes the Gauss points and their corresponding weights required for numerical integration.

6.3.2.4 Subroutine CONNECT

Once the node and side connectivity are verified, the CONNECT subroutine assigns the degree of freedom (DOF) lists in accordance with the hierarchical structure. These DOF lists were previously defined through the S/P INPUT process.

6.3.2.5 Subroutines STIFF & MASS & INVERT

On the basis of the components of the element matrices derived from Lagrange equation in the chapter V, as well as the formulation of the rectangular p-element described in Section V.3, the corresponding element stiffness and mass matrices are computed within the STIFF and MASS subroutines. Additionally, for static analysis, the inverse of global stiffness matrix is calculated using the subroutine INVERT.

6.3.2.6 Subroutine JACOBI

For describing the behavior of a structure, it is essential to determine its natural frequencies, vibration modes, and associated eigenvectors. Various numerical methods can be employed for computing these characteristics. In this study, the Jacobi method is used in order to calculate the mode shapes and natural frequencies.

- ✓ ***Method principle*** [Belalia (2011)]

The Jacobi method, developed by the German mathematician Karl Jacobi, is an iterative technique used to solve the generalized eigenvalue problem $[A]\{X_i\} = \lambda_i\{B\}\{X_i\}$.
For our problem, this method is employed to solve the following equation:

$$[K] - \lambda_i.[M] = \{X_i\} \tag{6.1}$$

A fundamental condition for applying this method is that the stiffness matrix $[K]$ and the mass matrix $[M]$ must be symmetric and positive definite.

The stiffness $[K]$ and mass$[M]$ matrices are progressively transformed into diagonal matrices through successive transformations.

$$\begin{aligned}
&[K^1] = [K] && [M^1] = [M] \\
&[K^2] = [T]_1^T\,[K]_1\,[T]_1 && [M^2] = [T]_1^T\,[M]_1\,[T]_1 \\
&[K^3] = [T]_2^T\,[K]_2\,[T]_2 && [M^3] = [T]_2^T\,[M]_2\,[T]_2 \\
&\ldots. && \ldots. \\
&\ldots. && \ldots. \\
&[K^{k+1}] = [T]_k^T\,[K]_k\,[T]_k && [M^{k+1}] = [T]_k^T\,[M]_k\,[T]_k \\
&\qquad [K^{k\to\infty}] = [K^d] && \qquad [M^{k\to\infty}] = [M^d]
\end{aligned} \tag{6.2}$$

Through successive transformations, the matrices $[K]$ and $[M]$converge towards diagonal matrices $[K^d]$; $[M^d]$ as $k \to \infty$. The eigenvalues and eigenvectors can then be evaluated from these diagonal matrices as follows:

$$[\lambda] = [K^d][M^d]^{-1} \iff [\lambda]_i = {[K]_{ii}^d}/{[M]_{ii}^d}$$
$$[X][T^1][T^2][T^3] \ldots\ldots [T^K][T^{k+1}] \begin{bmatrix} \ddots & & 0 \\ & \frac{1}{\sqrt{[M]_{ii}^d}} & \\ 0 & & \ddots \end{bmatrix} \tag{6.3}$$

6.3.2.7 Subroutine SORT

The SORT subroutine serves to arrange the eigenvalues and eigenvectors in ascending order.

6.3.2.8 Subroutine GFUNCT

The hierarchical shape functions associated with the quadrilateral p-element are formulated based on shifted orthogonal Legendre polynomials. Within the computational program developed, the subroutine GFUNCT is responsible for evaluating the shape functions and their partial derivatives taken with respect to the local coordinates (ξ, η).

6.3.2.9 Subroutine MODE

To compute the natural frequencies in the context of free vibration, all required expressions are formulated and implemented within the **MODE** subroutine.

6.3.2.10 Subroutine DEFLECTION

The computation of the central deflection is carried out within the DEFLECTION subroutine, where all the necessary expressions for load integration and vector of deflections are implemented.

6.3.2.11 Subroutine DRESP

This subroutine is employed to compute the dynamic response analysis of the plate over a specified time interval.

6.3.2.12 Subroutine LOADF

The LOADF subroutine is used to give the type of load applied to the structure.

6.3.2.13 Subroutine DISPLAY

This subroutine displays the dynamic response computed at the selected node and also shows the dimensionless central deflection for the static analysis.

6.3.3. Output file

The output file contains the parameters computed by the developed program, including:

- NEQB: The number of equations in the system.
- NMH: Degree of p-element polynomial.
- NMODE : Specific mode number.
- CENTER DEFLECTION: Dimensionless central deflection ($\overline{w}$) for static analysis.
- T: The **time** (in seconds) at each step of the dynamic analysis.
- *w*: The **central deflection** at the selected node at that instant.

Chapter 7 Static and dynamic analysis of porous FGM sandwich plate reinforced CNT

Objective

This chapter offers a comprehensive investigation of the static and dynamic behaviors of functionally graded porous sandwich plates reinforced carbon nanotubes (CNTs), using the p-version of the Finite Element Method. The study aims to demonstrate the accuracy and efficiency of the developed numerical formulation when applied to complex multilayered and functionally graded structures. The first part of chapter focuses on the static analysis, where the quadrilateral p-element is employed to determine the central deflection of the plate subjected to a constant transverse loading. The finite element solution procedure is first presented, followed by a convergence and comparison study to validate the proposed element.

The second part of chapter is dedicated to the dynamic analysis of the same structures. An analytical solution based on the Classical Plate Theory (CPT) is first developed to describe the dynamic behavior of FGM plates. In parallel, the p-version FEM formulation is extended to dynamic problems using the First-order Shear Deformation Theory (FSDT) and the mode superposition approach, ensuring both computational precision and consideration of shear effects. Finally, a detailed parametric investigation has been carried out to analyze the influences of CNT reinforcement, porosity, boundary conditions, geometric of plate and gradient index on both static and dynamic response of porous FG-CNTR sandwich plate.

7.1. Static analysis

7.1.1. Numerical solution procedure

The static behavior is analyzed for a FGM sandwich plate composed of porous face sheets and a core reinforced with carbon nanotubes (CNTs). The plate is subjected to a constant distributed transverse mechanical load denoted by $q(x,y) = C_0$. In the case of linear static analysis, the equilibrium condition governing the system can be expressed as:

$$[K]\{q_j\} = \{P\} \tag{7.1}$$

where $[K]$ is the global stiffness matrix, $\{q_j\}$ represents the vector containing the generalized transverse displacement and rotation terms as described in the Eq. (5.33), and $\{P\}$ is the load vector, respectively.

The load vector is represented in terms of the shape functions as follows.

$$\{P\} = \int_0^1 \int_0^1 [N]\, C_0\, abd\xi d\eta \tag{7.2}$$

7.1.2. Convergence analysis and validation modeling

7.1.2.1 Validation free vibration

This section provides several numerical examples to demonstrate the accuracy and validity of the *p*-version FEM in predicting the bending and free vibration of FGM sandwich plates. The analyses are performed using rectangular *p*-elements with polynomial order of $p = 9$. Ten configurations of simply supported FGM sandwich plates presented in this study are summarized in table 7.1, while the corresponding material properties are listed in table 7.2.

Table 7.1 : FGM sandwich plate

Thickness	**1-0-1**	**1-1-1**	**1-2-1**	**1-3-1**	**1-4-1**	**1-6-1**	**1-8-1**	**2-1-2**	**2-2-1**	**2-1-1**
$\mathbf{h_0}$	-h/2	-h/2	-h/2	-h/2	-h/2	-h/2	-h/2	-h/2	-h/2	-h/2
$\mathbf{h_1}$	0	-h/6	-h/4	-3h/10	-h/3	-3h/8	-2h/5	-h/10	-h/10	0
$\mathbf{h_2}$	0	h/6	h/4	3h/10	h/3	3h/8	2h/5	h/10	3h/10	h/4
$\mathbf{h_3}$	h /2	h/2	h/2	h/2	h/2	h/2	h/2	h/2	h/2	h/2

Table 7.2 : Material properties of FGM components

Material		**Properties**		
		$E\ (GPa)$	ν	$\rho\ (kg/m3)$
Metal	Aluminum (Al)	70.00	0.3	2707
	Stainless steel SUS304	2707	0.3177	8166
	Ti-6Al-4V	105.7	0.29	4429
Ceramic	Alumina (Al_2O_3)	380	0.3	3800
	Zirconia (ZrO_2)	151	0.3	3000

Tables 7.3 and 7.4 present a comparative analysis of fundamental frequencies of six FGM sandwich plates with homogeneous ceramic cores made of different metal–ceramic combinations, for both cases with and without porosity. The obtained results show a very matches well with those reported in the literature, confirming the validity and reliability of the proposed model. By progressively increasing the polynomial order from 2 to 9, the desired level of accuracy in the numerical results for simply supported configurations is achieved. A clear trend of rapid convergence is observed as the polynomial order increases, with stable and accurate results obtained from $p = 6$ onwards. This behavior highlights the efficiency, stability, and robustness of the developed p-version FEM in accurately predicting the free vibration characteristics of FGM sandwich plates. The fundamental frequencies can be obtained using the following relation: $\left(\Omega = \omega \frac{a^2}{h}\sqrt{\frac{\rho_0}{E_0}}\right)$ (where $\rho_0 = 1\ Kg/m^3\ and\ E_0 = 1$ GPa).

Table 7.3 : Convergence and comparison of fundamental frequencies of FGM sandwich plates with existing theories

n	Methods	p	1-0-1	1-1-1	1-2-1	2-1-2	2-2-1	2-1-1
0	**Present**	**2**	**1.93283**	**1.93283**	**1.93283**	**1.93283**	**1.93283**	**1.93283**
		4	**1.82470**	**1.82470**	**1.82470**	**1.82470**	**1.82470**	**1.82470**
		6	**1.82442**	**1.82442**	**1.82442**	**1.82442**	**1.82442**	**1.82442**
		9	**1.82442**	**1.82442**	**1.82442**	**1.82442**	**1.82442**	**1.82442**
	FSDT[Belalia (2017)]		1.82442	1.82442	1.82442	1.82442	1.82442	1.82442
	TSDT[El Meiche et al. (2011)]		1.82445	1.82445	1.82445	1.82445	1.82445	1.82445
0.5	**Present**	**2**	**1.52837**	**1.60809**	**1.66709**	**1.57066**	**1.64303**	**1.60105**
		4	**1.44191**	**1.51719**	**1.57298**	**1.48182**	**1.55025**	**1.51058**
		6	**1.44167**	**1.51695**	**1.57274**	**1.48159**	**1.55001**	**1.51035**
		9	**1.44167**	**1.51695**	**1.57274**	**1.48159**	**1.55001**	**1.51035**
	FSDT[Belalia (2017)]		1.44167	1.51695	1.57274	1 .48159	1.54958	1.50981
	TSDT[El Meiche et al. (2011)]		1.44424	1.51922	1.57451	1.48408	1.55199	1.51253
1	**Present**	**2**	**1.31531**	**1.43234**	**1.52388**	**1.37575**	**1.49032**	**1.42765**
		4	**1.24051**	**1.35093**	**1.43745**	**1.29749**	**1.40576**	**1.34658**
		6	**1.24032**	**1.35072**	**1.43722**	**1.29729**	**1.40554**	**1.34637**
		9	**1.24032**	**1.35072**	**1.43722**	**1.29729**	**1.40554**	**1.34637**
	FSDT[Belalia (2017)]		1.24032	1.35072	1.43722	1.29729	1.40446	1.34500
	TSDT[El Meiche et al. (2011)]		1.24320	1.35333	1.43934	1.30011	1.40789	1.34888
5	**Present**	**2**	**0.99965**	**1.10538**	**1.24286**	**1.03836**	**1.21424**	**1.13666**
		4	**0.94271**	**1.04200**	**1.17177**	**0.97886**	**1.14485**	**1.07173**
		6	**0.94256**	**1.04183**	**1.17159**	**0.97870**	**1.14466**	**1.07156**
		9	**0.94256**	**1.04183**	**1.17159**	**0.97870**	**1.14466**	**1.07156**
	FSDT[Belalia (2017)]		0.94256	1.04183	1.17159	0.97870	1.14118	1.06754
	TSDT[El Meiche et al. (2011)]		0.94598	1.04466	1.17397	0.98184	1.14731	1.07432

Table 7.4 : Comparison of fundamental frequencies of a simply supported FGM sandwich plate with various porosity distributions ($a/h = 10$, n = 2 and $a/b = 1$)

Porosity	e	Methods	1-0-1	1-1-1	1-2-1	2-1-2	2-2-1	2-1-1
Perfect	0	**Present**	**1.05855**	**1.18591**	**1.30040**	**1.11965**	**1.26544**	**1.19236**
		FSDT[Bentrar et al. (2023)]	1.05855	1.18591	1.30040	1.11965	1.26310	1.18951
		HSDT[Daikh et Zenkour (2019c)]	1.06155	1.18847	1.30244	1.12248	1.24391	1.16529
Imperfect I	0.1	**Present**	**0.98007**	**1.11856**	**1.24758**	**1.04477**	**1.21325**	**1.13338**
		FSDT[Bentrar et al. (2023)]	0.98007	1.11856	1.24758	1.04478	1.21010	1.12937
		HSDT[Daikh et Zenkour (2019c)]	0.98258	1.12071	1.24933	1.04712	1.18195	1.09355
	0.2	**Present**	**0.87684**	**1.04036**	**1.19014**	**0.95317**	**1.15526**	**1.06445**
		FSDT[Bentrar et al. (2023)]	0.87684	1.04036	1.19014	0.95317	1.15094	1.05860
		HSDT[Daikh et Zenkour (2019c)]	0.87867	1.04201	1.19156	0.95491	1.11054	1.00557
Imperfect II	0.1	**Present**	**1.02932**	**1.15520**	**1.27528**	**1.08732**	**1.24165**	**1.16748**
		FSDT[Bentrar et al. (2023)]	1.02932	1.15520	1.27528	1.08732	1.23895	1.16414
		HSDT[Daikh et Zenkour (2019c)]	1.03235	1.15768	1.27723	1.09008	1.21572	1.13481
	0.2	**Present**	**0.99729**	**1.12287**	**1.24953**	**1.05262**	**1.21711**	**1.14134**
		FSDT[Bentrar et al. (2023)]	0.99729	1.12290	1.24953	1.05262	1.21398	1.13740
		HSDT[Daikh et Zenkour (2019c)]	1.00033	1.12524	1.25140	1.05528	1.18609	1.10199
Imperfect III	0.1	**Present**	**1.03006**	**1.15597**	**1.27589**	**1.08813**	**1.24223**	**1.16791**
		FSDT[Bentrar et al. (2023)]	1.03006	1.15597	1.27589	1.08813	1.23954	1.16477
		HSDT[Daikh et Zenkour (2019c)]	1.03308	1.15844	1.27785	1.09089	1.21642	1.13558
	0.2	**Present**	**1.00044**	**1.12599**	**1.25198**	**1.05599**	**1.21945**	**1.14386**
		FSDT[Bentrar et al. (2023)]	1.00044	1.12599	1.25198	1.05599	1.21637	1.13998
		HSDT[Daikh et Zenkour (2019c)]	1.00347	1.12837	1.25386	1.05867	1.18894	1.10519
Imperfect IV	0.1	**Present**	**1.02189**	**1.15354**	**1.27464**	**1.08409**	**1.24646**	**1.17276**
		FSDT[Bentrar et al. (2023)]	1.02190	1.15354	1.27464	1.08408	1.24395	1.16975
		HSDT[Daikh et Zenkour (2019c)]	1.05559	1.17079	1.28422	1.10840	1.22699	1.15122
	0.2	**Present**	**1.03183**	**1.11937**	**1.24821**	**1.04571**	**1.22699**	**1.15230**
		FSDT[Bentrar et al. (2023)]	1.03187	1.11935	1.24820	1.04566	1.22430	1.14914
		HSDT[(Daikh et Zenkour 2019c)]	1.05213	1.15260	1.26581	1.09394	1.20966	1.13763

In the context of FGM sandwich plates reinforced with carbon nanotubes (CNTs), the free flexural vibration of CNT-reinforced sandwich plates subjected to thermal loading is analyzed and presented in table 7.5. The nondimensionalized frequency is expressed as: $\left(\Omega = \omega \frac{a^2}{h}\sqrt{\frac{\rho_H}{E_H}}\right)$, where E_H and ρ_H denote the Young's modulus and mass density of the homogeneous core, respectively. The core material is composed of Ti–6Al–4V titanium alloy,

and its mechanical properties are: $E_H = 122.56(1 - 4.586 \times 10^{-4}\,\mathrm{T})\mathrm{GPa}$, and $\rho_H = 4429 Kg/m^3$. A close agreement is observed between the present results and the data available in the literature, confirming the reliability of the proposed model. The effect of the CNT volume fraction (V^*_{CNT}) is also highlighted. As the temperature increases, the nondimensional frequency decreases, while it increases with higher CNT volume fractions, which is consistent with physical expectations.

Table 7.5 : Fundamental frequency comparison for a simply supported square sandwich plate (a/h=20, $h_c/h_f = 4$) with a homogeneous core.

Temperature	Refrences	$\mathbf{V^*_{CNT} = 0.12}$	$\mathbf{V^*_{CNT} = 0.17}$	$\mathbf{V^*_{CNT} = 0.28}$
300 K	**Present**	**4.6719**	**5.0579**	**5.6872**
	FSDT5[a]	4.6765	5.0639	5.6935
	HSDT13[a]	4.6518	5.0381	5.6422
	HSDT11A[a]	4.6508	5.0366	5.6394
	HSDT11B[a]	4.6803	5.0683	5.6980
	HSDT9[a]	4.6793	5.0669	5.6955
500 K	**Present**	**4.4796**	**4.8666**	**5.4969**
	FSDT5[a]	4.4776	4.8623	5.4982
	HSDT13[a]	4.4425	4.8244	5.4238
	HSDT11A[a]	4.4416	4.8232	5.4216
	HSDT11B[a]	4.4809	4.8658	5.5005
	HSDT9[a]	4.4801	4.8647	5.4985

[a]Natarajan et al. (2014)

7.1.2.2 Validation static analysis

The governing equations of motion, as derived in the previous section are simplified to the static equilibrium form by neglecting inertial terms. For validating the accuracy of the proposed formulation in static analysis, three configurations of FGM sandwich plates are considered.

The first case, presented in table 7.6, corresponds to FGM sandwich plates without porosity, serving as a reference configuration to assess the reliability of the present model. The second case, given in table 7.7, introduces the effect of porosity distributed within the face sheets, allowing the evaluation of its influence on the flexural stiffness and central deflection. The third case, summarized in table 7.8, examines CNT-reinforced sandwich plates, in which the face sheets are strengthened by carbon nanotubes to enhance the overall mechanical performance. A very good agreement is observed between the current results and those reported in the reference data from the literature, confirming the accuracy, efficiency, and reliability of

the proposed model in estimating the static response of FGM sandwich plates with, without porosity and CNT reinforcement.

The expressions of the nondimensional central deflection differ slightly according to the material configuration and distribution type. The following relations are therefore used for the three considered cases.

✓ **Cases 1 and 2**: Homogeneous and porous FGM sandwich plates

$$\bar{w} = \frac{10hE_0}{q_0 a^2} w\left(\frac{a}{2}, \frac{b}{2}\right) \tag{7.3}$$

✓ **Case 3:** CNT- reinforced facesheets sandwich plate

$$\bar{w} = \frac{100E_H}{q_0 h S^4} w\left(\frac{a}{2}, \frac{b}{2}\right) \tag{7.4}$$

(where $q_0 = 1\ MPa, S = a/h$).

Table 7.6 : Convergence and comparison of the nondimensional central deflection $\bar{w}$ for a simply supported perfect Al/ZrO_2 sandwich plate with different volume fraction (a/h = 10).

Schemes	References	n					
		0	0.5	1	2	5	10
1-1-1	**Present**	**0.1962**	**0.2556**	**0.2935**	**0.3350**	**0.3743**	**0.3886**
	Daikh et Zenkour (2019b)	0.1960	-	0.2919	0.3328	0.3713	0.3851
	Van Vinh et Huy (2022)	0.1959	-	0.2917	0.3326	0.3711	-
	Zenkour (2005)	0.1960	-	0.2919	0.3328	0.3712	0.3849
	Neves et al. (2012)	0.1961	0.2583	0.2949	0.3351	0.3729	0.3868
1-2-1	**Present**	**0.1962**	**0.2431**	**0. 2721**	**0. 3042**	**0.3369**	**0.3506**
	Daikh et Zenkour (2019b)	0.1960	-	0.2709	0.3026	0.3347	0.3481
	Van Vinh et Huy (2022)	0.1954		0.2700	0.3016	0.3337	-
	Zenkour (2005)	0.1960	-	0.2709	0.3026	0.3347	0.3411
	Neves et al. (2012)	0.1961	0.2460	0.2740	0.3053	0.3370	0.3503
2-2-1	**Present**	**0.1962**	**0. 2486**	**0.2807**	**0.3150**	**0.3472**	**0.3593**
	Daikh et Zenkour (2019b)	0.1960	–	0.2808	0.3161	0.3495	0.3620
	Van Vinh et Huy (2022)	0.1954	–	0.2910	0.3317	0.3702	–
	Zenkour (2005)	0.1960	–	0.2808	0.3161	0.3495	0.3491
	Neves et al. (2012)	0.1961	0.2519	0.2838	0.3053	0.3370	0.3503

Table 7.7 : Convergence and comparison of the nondimensional central deflection $\bar{w}$ for a simply supported porous Al/ZrO_2 sandwich plate ($a/h = 10, n = 2$).

Porosity	e	References	1–0–1	1–1–1	1–2–1	2–1–2	2–2–1
Perfect	0	**Present**	**0.3757**	**0.3350**	**0.3042**	**0.3547**	**0.3150**
		(Belarbi et al. 2022)	0.3723	0.3324	0.3023	0.3517	0.3211
		(Daikh et Zenkour 2019b)	0.3732	0.3328	0.3026	0.3522	0.3161
		FE-HSDT(Van Vinh et Huy 2022)]	0.3721	0.3317	0.3016	0.3511	0.3151
Imperfect I	0.1	**Present**	**0.4465**	**0.3883**	**0.3432**	**0.4168**	**0.3575**
		Belarbi et al. (2022)	0.4332	0.3775	0.3352	0.4046	0.3565
		Daikh et Zenkour (2019b)	0.4415	0.3840	0.3401	0.4120	0.3596
		FE-HSDT[Van Vinh et Huy (2022)]	0.4401	0.3828	0.3390	0.4107	0.3584
	0.2	**Present**	**0.5437**	**0.4573**	**0.3906**	**0.5002**	**0.4100**
		Belarbi et al. (2022)	0.5181	0.4371	0.3763	0.4766	0.4015
		Daikh et Zenkour (2019b)	0.5355	0.4507	0.3860	0.4924	0.4150
		FE-HSDT[Van Vinh et Huy (2022)]	0.5338	0.4493	0.3848	0.4909	0.4136
Imperfect III	0.1	**Present**	**0.4036**	**0.3564**	**0.3186**	**0.3796**	**0.3305**
		Belarbi et al. (2022)	0.4061	0.3521	0.3172	0.3740	0.3366
		Navier-PSDT(Daikh et Zenkour 2019b)]	0.4000	0.3552	0.3196	0.3775	0.3352
	0.2	**Present**	**0.4333**	**0.3787**	**0.3331**	**0.4059**	**0.3463**
		Belarbi et al. (2022)	0.4220	0.3732	0.3329	0.4001	0.3531
		Navier-PSDT[Daikh et Zenkour (2019b)]	0.4285	0.3789	0.3371	0.4044	0.3552

Table 7.8 : Convergence and comparative analysis of the dimensionless central deflection ($\overline{w}$) for a simply supported square sandwich plates with homogeneous core and CNT reinforced face-sheets

a/h	References	$\boldsymbol{h_H/h_f = 2}$		$\boldsymbol{h_H/h_f = 6}$	
		$V^*_{CNT} = 0.17$	$V^*_{CNT} = 0.28$	$V^*_{CNT} = 0.17$	$V^*_{CNT} = 0.28$
5	**Present**	**0.0773**	**0.0600**	**0.0540**	**0.0471**
	Singh et Sahoo (2021)	0.0708	0.0531	0.0522	0.0450
	HSDT13[a]	0.1036	0.0906	0.0533	0.0481
	HSDT11A[a]	0.1084	0.0945	0.0557	0.0502
	HSDT11B[a]	0.0813	0.0659	0.0504	0.0441
	HSDT9[a]	0.0847	0.0683	0.0526	0.0458
	TSDT7[a]	0.0744	0.0573	0.0523	0.0455
	FSDT5[a]	0.0773	0.0604	0.0538	0.0471
10	**Present**	**0.0656**	**0.0473**	**0.0480**	**0.0407**
	Singh et Sahoo (2021)	0.0627	0.0606	0.0467	0.0394
	HSDT13[a]	0.0738	0.0574	0.0470	0.0404
	HSDT11A[a]	0.0749	0.0583	0.0477	0.0410
	HSDT11B[a]	0.0658	0.0485	0.0461	0.0391
	HSDT9[a]	0.0668	0.0492	0.0468	0.0397
	TSDT7[a]	0.0637	0.0458	0.0467	0.0396
	FSDT5[a]	0.0645	0.0466	0.0471	0.0400

[a]Natarajan et al. (2014)

7.2. Dynamic analysis

7.2.1. Analytical solution for FGM plates

The analytical solution for central deflection of square FGM plate under a central dynamic load based on the Classical Plate Theory (CPT) is defined by the following equation:

$$w(a,a,t) = \frac{16C_0a^2}{\pi^4 D_f} \sum_{i=1,3,5\ldots}^{\infty} \sum_{j=1,3,5\ldots}^{\infty} \frac{1-\cos(\omega_{ij}t)}{(i^2+j^2)^2} \tag{7.5}$$

where

$$\omega_{ij} = \frac{\pi^2(i^2+j^2)}{4\,a^2}\sqrt{\frac{D_f}{I_0}} \tag{7.6}$$

$$D_f = \int_{\frac{-h}{2}}^{\frac{h}{2}} \frac{z^2 E(z)}{1-\nu^2}\,dz \tag{7.7.1}$$

and,

$$I_0 = \int_{\frac{-h}{2}}^{\frac{h}{2}} \rho(z)\,dz \tag{7.7.2}$$

The final expressions in terms of the flexural rigidity and the FGM plate's inertial coefficient is

$$D_f = \frac{(E_c - E_m)h^3}{1-\nu^2}\left\{\frac{1}{n+3} - \frac{1}{n+2} + \frac{1}{4(n+1)}\right\} + \frac{E_m h^3}{12(1-\nu^2)} \tag{7.8.1}$$

and,

$$I_0 = \frac{(\rho_c - \rho_m)h}{n+1} + \rho_m h \tag{7.8.2}$$

7.2.2. FEM solution

The mode superposition method is widely employed to reduce the number of unknown variables considered in dynamic solution analysis. It accurately approximates all types of loading employing piecewise linear or cubic functions over small time increments [Dong (2008)]. The equation governing dynamic force equilibrium can then be represented as a system of N_d second-order differential equations in the form given by

$$[K]q + [C]\,\frac{dq}{dt} + [M]\,\frac{d^2q}{dt^2} = p \tag{7.9}$$

$[M]$, $[K]$, and $[C]$ denote the mass, stiffness, and damping matrices, with damping coefficients estimated using eigenmode orthogonality.

$$[\Phi]^t\,[C]\,[\Phi] = diag(2\xi_1\omega_1, 2\xi_2\omega_2, \ldots, 2\xi_r\omega_r, \ldots, 2\xi_n\omega_n) \tag{7.10}$$

where ω_r , ξ_r are identified as the fundamental frequency and the related damping ratio, respectively, associated with mode r and $[\Phi]$ is the normalized modal matrix.

Prior to solving, the spatial functions are required to satisfy the mass and stiffness orthogonality conditions.

$$[\Phi]^t[M]\,[\Phi] = [I] \tag{7.11}$$

here $[I]$ forms a unit diagonal matrix.

From Eq. (7.10), it is clear that

$$[\Phi]^{-1} = [\Phi]^t[M] \tag{7.12}$$

With the substitution of Eq. (7.11) into Eq. (7.9), we obtain

$$[C] = [M]\,[\textstyle\sum_{r=1}^{n} 2\xi_r\omega_r[\Phi_r]\,[\Phi_r]^t]\,[M] \tag{7.13}$$

The mode superposition technique, introduced in the next section, converts a system of coupled equations into independent equations using modes. The primary step to solve via mode superposition is to compute and determine the natural fundamental frequencies and vibration modes that satisfy the equation

$$\big[[K] - \omega^2[M]\big][\Phi] = 0 \tag{7.14}$$

The vibration modes are considered to be normalized to give

$$[\Phi_r]^T[\,M]\,[\Phi_r] = 1 \quad , \; [\Phi_r]^T\,[K]\,[\Phi_r\,] = {\omega_r}^2 \, , \; [\Phi_r]^T\,[C]\,[\Phi_r] = \; 2\xi_r\omega_r \tag{7.15}$$

Implementing the coordinate transformation is a fundamental step in the mode superposition

$$\{q\} = [\Phi]\,\{\eta\} = \; \textstyle\sum_{r=1}^{n}[\Phi_r]\,\{\eta_r\} \tag{7.16}$$

where $\{\eta_r\}$ are referred to normal coordinates. With the substitution of Eq. (7.15) in Eq. (7.8) yields

$$\frac{d^2\eta_r}{dt^2} + 2\xi_r\omega_r\frac{d\eta_r}{dt} + \; {\omega_r}^2\eta_r = \gamma_r \tag{7.17}$$

where $$\gamma_r = [\Phi_r]^T\,p \tag{7.18}$$

The total response results from the superposition of initial condition and excitation effects, with the r-mode response combining both contributions. A simple and effective numerical method solves Eq. (7.15) using linear interpolation applied to the modal excitation and exact solution [Houmat A. (2022)].

7.2.3. Validation and Convergence

The forced response of simply supported square FGM sandwich plate with thickness-to-side ratio of $h/a = 0.01$ has been investigated using both the developed analytical model for FGM plates and a rectangular finite p-element with polynomial order of $p = 9$, subjected to a

constant load C_0. For validation purposes, a uniform load of $C_0 = 1000\text{N}$ is considered, and the case $n_1 = n_2 = n = 0$ is adopted to transform the FGM sandwich plate into an equivalent isotropic ceramic plate. The undamped central deflection response is presented in figure 7.1 for loading duration of $0.05\ s$ with a time step of $0.0005\ s$. The figure clearly shows an excellent concordance between the results derived from the FEM and the analytical solution. Minor discrepancies observed over time are likely due to differences between the two plate theories: the Mindlin theory based on the FSDT, which includes transverse shear deformation effects, and the Kirchhoff theory (CPT), which neglects them.

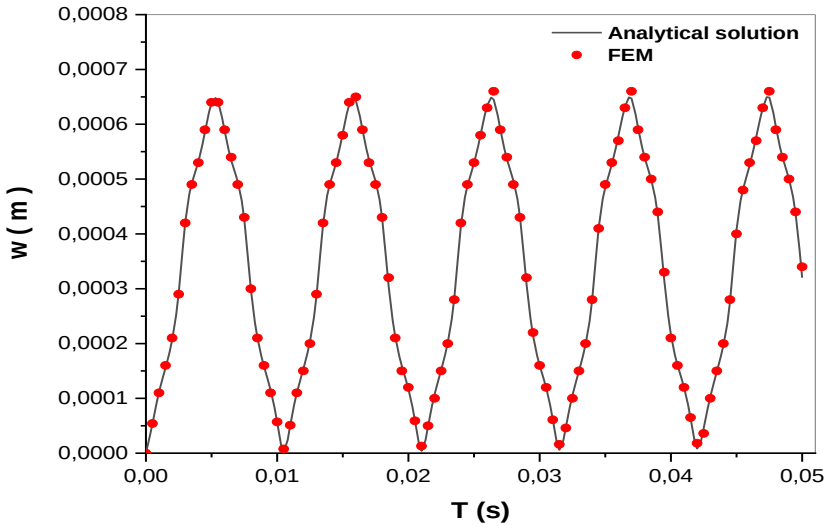


Figure 7.1 : Comparative analysis of the dynamic response of simply supported square FGM sandwich plate.

7.3. Parametric study

Following the validation of the proposed formulation against existing results, a comprehensive parametric study is undertaken to analyze the effects of different parameters on the static and dynamic responses of the porous FGM sandwich plate. In this parametric investigation, different material systems are employed for the static and dynamic analyses to better demonstrate the versatility of the proposed formulation. The static behavior is studied using an Al/ZrO_2 sandwich plate, while the dynamic analysis is performed for an $\text{Al}/\text{Al}_2\text{O}_3$ sandwich plate. This choice allows for evaluating the model accuracy under different material combinations and mechanical contrasts between the core and face sheets.

For simplification, it is assumed that the material gradation and porosity parameters are identical in both face sheets, i.e., ($n_1 = n_2 = n$, and $e_1 = e_2 = e$).

The effect of the volume fraction index n on the mechanical response of the FGM sandwich plate is first examined. This parameter controls the material gradation across the thickness and

therefore has a significant impact on both the stiffness and deformation behavior of the structure. Figure 7.2 illustrates the variation of the dimensionless central deflection ($\bar{w}$) of a reinforced sandwich plate without porosity as a function of the aspect ratio (a/h), for different values of the volume fraction exponent (n $=$ 0.5, 2, 5, and 10) and two CNT volume fractions ($V^*_{CNT} = 0.17$, and 0.28). Figure 7.3 depicts the dynamic response of a porous FGM sandwich plate subjected to a constant load $C_0 = 10\,000$ N. The results are presented for three values of the volume fraction exponent ($n = 0.5, 1,$ and 5) and for two types of porous FGM sandwich configurations, namely 1–2–1 and 1–8–1. From the graphs, in the static case the central deflection increases with the rise of the side-to-thickness ratio (a/h) and the volume fraction exponent (n). Similarly, in the dynamic analysis the amplitudes increase as the volume fraction exponent increases indicating greater flexibility of the plate over time.

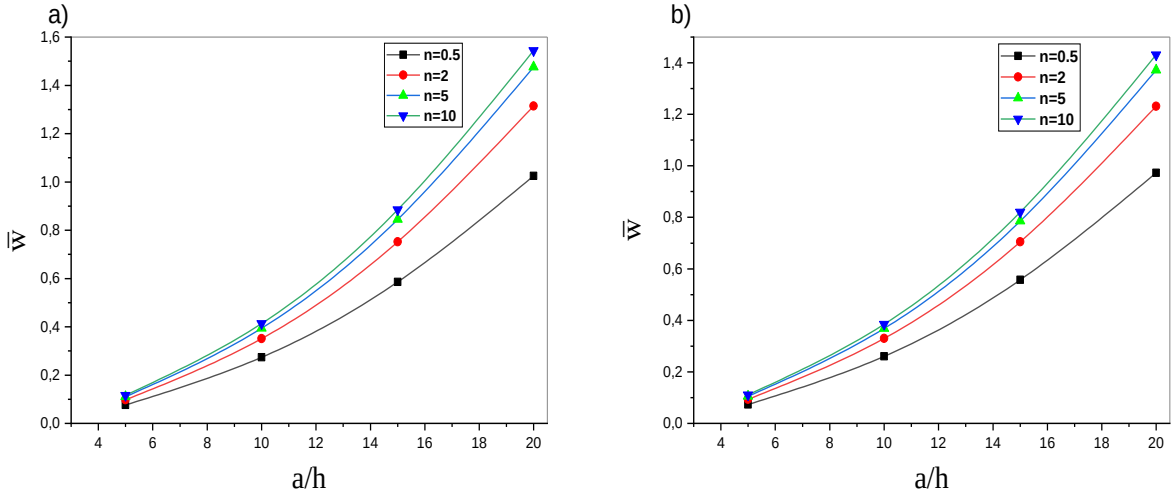


Figure 7.2 : Effect of volume fraction exponent on the dimensionless central deflection of simply supported FG-CNTR sandwich plate (UD; a/b=1; e=0; $h_H/h_f = 2$): a) $V^*_{CNT} = 0.17$, b) $V^*_{CNT} = 0.28$

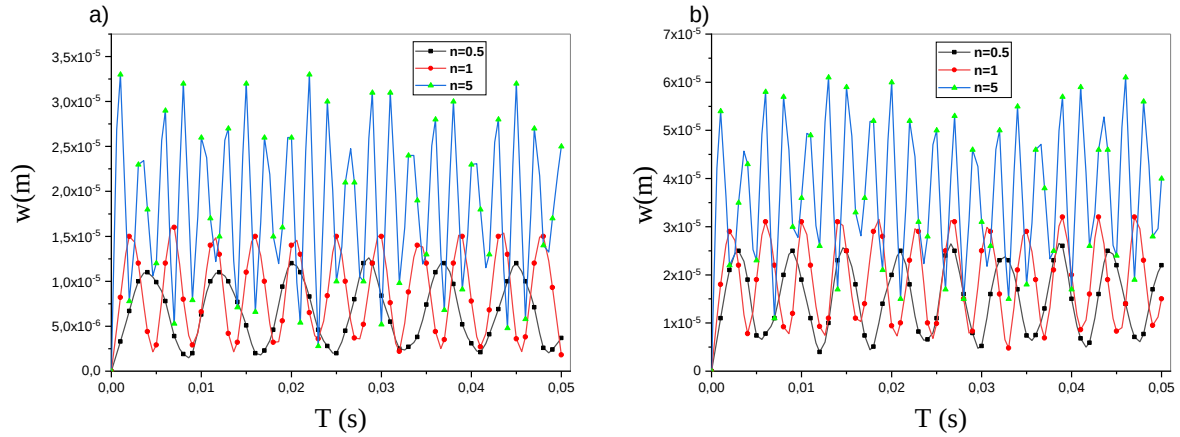


Figure 7.3 : Effect of volume fraction exponent on the dynamic response of simply supported FG-CNTR sandwich plate (UD; e=0.1; a/h=10; $V^*_{CNT} = 0.12$): a)1-2-1, b)1-8-1

To further investigate the effect of CNT distribution on the static and dynamic behavior of the structure, three types of core reinforcement are studied, including uniform, FG-X and FG-O distributions. The results obtained for $n = 2$ and $e = 0$. As shown figures 7.4 and 7.5 two configuration of plates are presented ($1-6-1$ and $1-8-1$). In the static analysis, the deflection increases with the increase of aspect ratio (a/h). For both static and dynamic analyses, it is evident that the FG-X distribution exhibits the highest deflection.

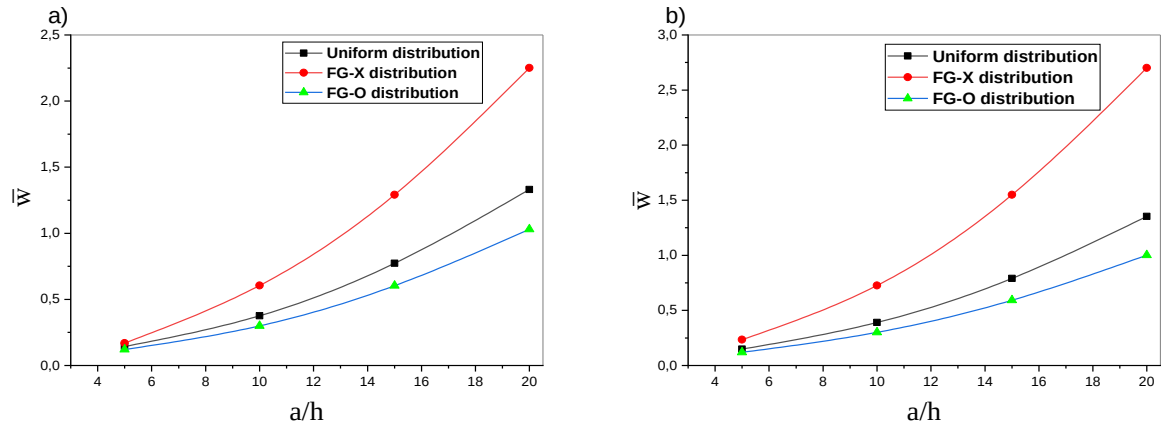


Figure 7.4 : Influence of CNT distribution on dimensionless central deflection of simply supported square FG-CNTR sandwich plate ($V^*_{CNT} = 0.17$): a) $1-6-1$, b) $1-8-1$

To clearly illustrate the influence of CNT distribution on the structural response and under the same condition, the dimensionless central deflection is evaluated for nine different FGM sandwich plate configurations while keeping the side-to-thickness ratio fixed at $a/h = 10$ considering three types of CNT distributions. As shown in the figure 7.6 the large value of the

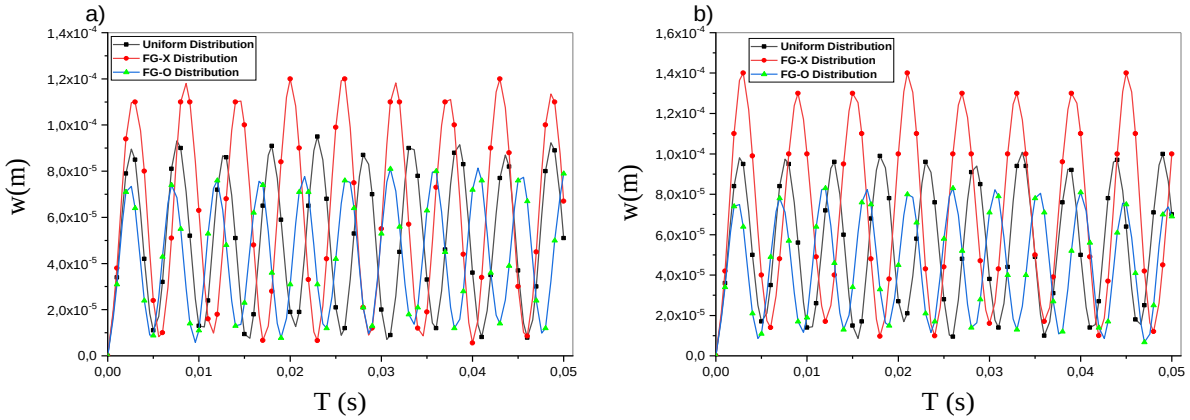


Figure 7.5 : Dynamic response of the sandwich FG-CNTR reinforced plate with different CNT distributions: ($V^*_{CNT} = 0.12; a/h = 10;\ C_0 = 10\ 000$ N): a) $1-6-1$, b) $1-8-1$

central deflection is observed for the $1-8-1$ plate with the FG-X model of CNT distribution. This behavior indicates that, for a core-to-facesheet thickness ratio $h_c/h_f = 8$, the deflection becomes significant due to the reduced stiffness of the CNT-reinforced FG-X core, which,

along with the loss of stiffness caused by face sheet porosity, contributes to the observed increase in central deflection.

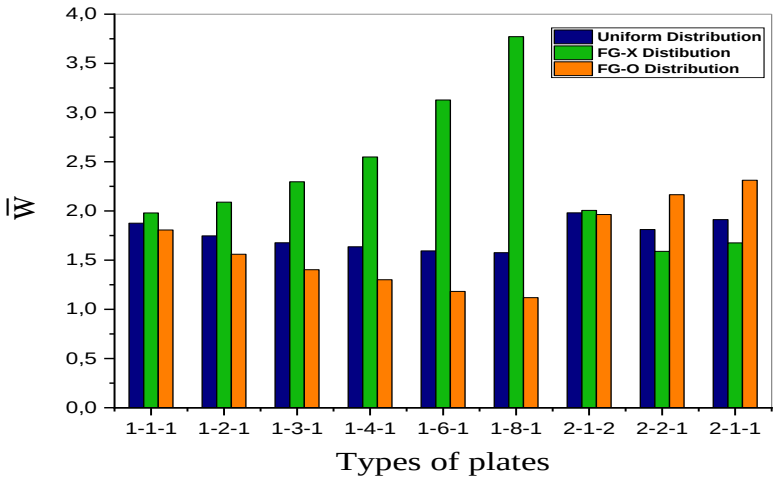


Figure 7.6 : The dimensionless central deflection of square FG-CNTR porous sandwich plate for different types of plates under various CNT distribution ($n = 2;\ e = 0.2;\ V^{*}_{CNT} = 0.17$)

The influence of the porosity coefficient on the static and dynamic responses, in terms of the undamped midpoint deflection of a porous FGM sandwich plate reinforced with CNTs, is illustrated in the figures 7.7 and 7.8 respectively. The study was conducted on a 1-2-1 sandwich plate with an even porosity model 'Imperfect 1', considering three CNT distribution types ('UD', 'FG-X', and 'FG-O') and three different porosity coefficients ($e = 0, 0.1, \text{and } 0.2$). It is observed that the deflection amplitude increases with the rise in the porosity coefficient, which can be attributed to the reduction in material stiffness caused by the presence of pores. Moreover, the FG-X core reinforced sandwich plate with $e = 0.2$ exhibits the highest dimensionless central deflection for the static response, as well as the greatest deflection amplitude in the dynamic analysis.

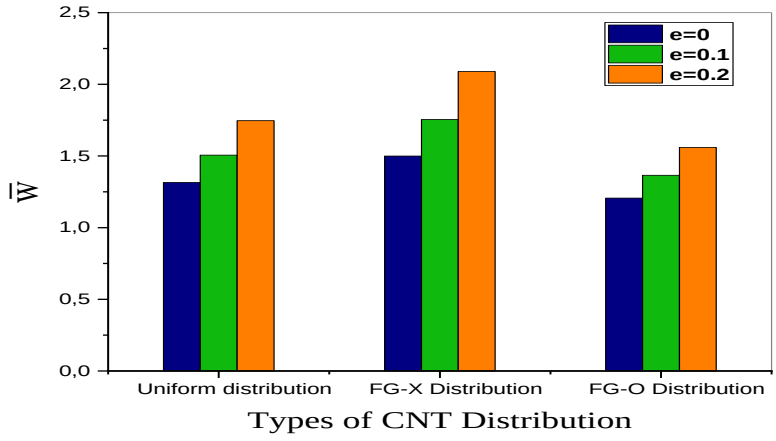


Figure 7.7 : Effect of CNT models on the dimensionless central deflection of FG-CNTR sandwich plate with varying porosity coefficient ($a/h = 10;\ n = 2;\ V^{*}_{CNT} = 0.17$)

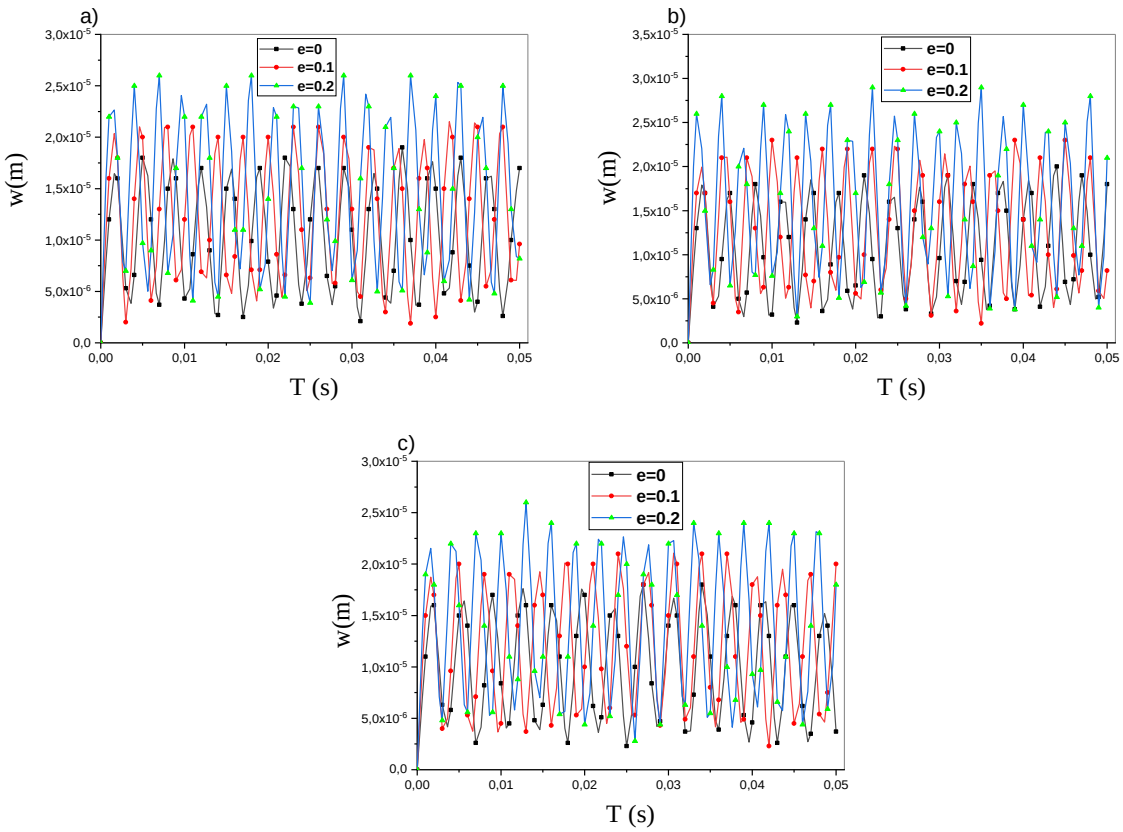


Figure 7.8 : Dynamic response of the sandwich FG-CNTR reinforced plate with different distribution of CNT (a/h=10; $C_0 = 8\ 000$ N): a) UD, b) FG X distribution, c) FG O distribution.

An investigation is conducted to examine the effect of the core-to-face sheet thickness ratio h_c/h_f, and the results obtained for $n = 2$ and Imperfect I model porosity. In the case of static behavior, the central deflection of the square FGM sandwich plate increases as the core-to-face sheet thickness ratio increases as shown figure 7.9, indicating a greater overall flexibility of the structure. For the dynamic analysis, a load of 10 000 N is applied, the undamped response of central deflection of the simply supported square FGM sandwich plate increases with the rise of the core-to-face sheet thickness ratio over time (Figure 7.10). This can be explained by the fact that increasing the core-to-face sheet thickness ratio reduces the overall stiffness of the sandwich structure, thereby allowing greater deformation in both the static response and dynamic excitation.

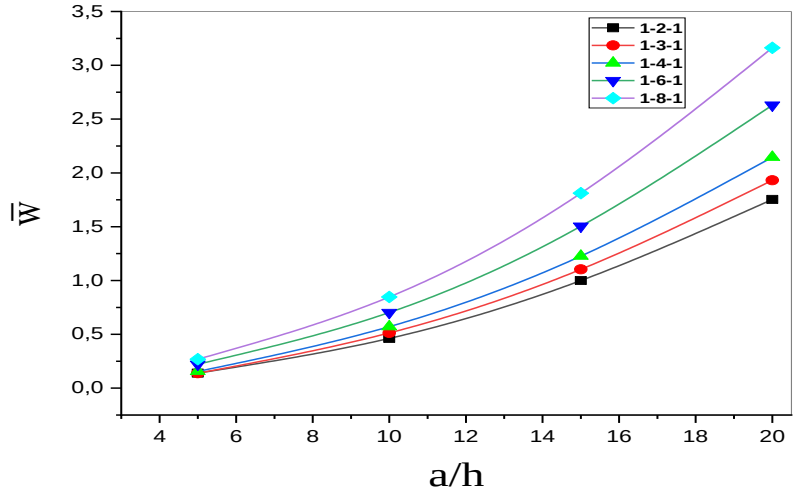


Figure 7.9 : Influence of core-to-face sheet thickness ratio h_c/h_f on dimensionless central deflection of simply supported square porous FG-CNTR sandwich plate (FG-X; $V^*_{CNT} = 0.17; e = 0.1$)

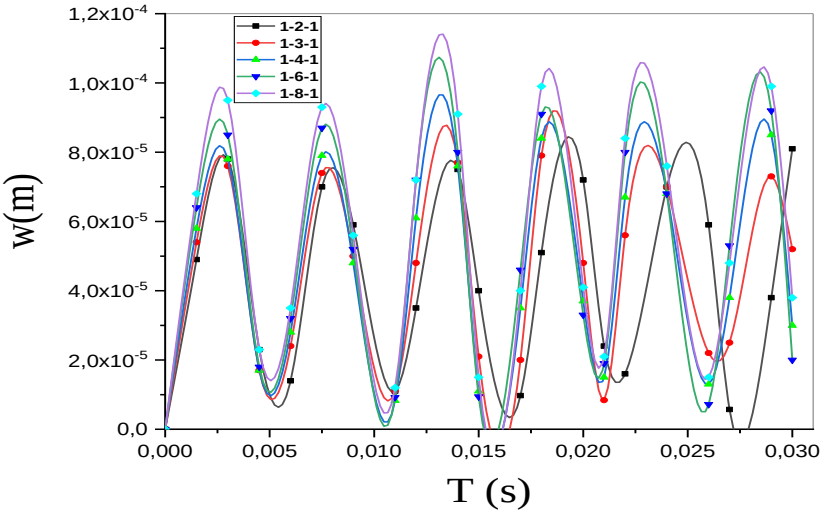


Figure 7.10 : Effect of core-to-face sheet thickness ratio h_c/h_f on the dynamic response of simply supported FGM sandwich plate (UD; $a/h = 20$; $V^*_{CNT} = 0.12$; $e = 0$).

To examine the effect of CNTs volume fraction on the dynamic response, the influence of different CNT volume fractions ($V^*_{CNT} = 0.12, 0.17$, and 0.28) was analyzed for two plate configurations ($1-6-1$ and $1-8-1$), as shown in figure 7.11. Under identical previous conditions, an increase in CNT volume fraction leads to a reduction in central deflection, indicating that CNT reinforcement effectively enhances the stiffness of the FGM sandwich structure and reduces its vibrational amplitude.

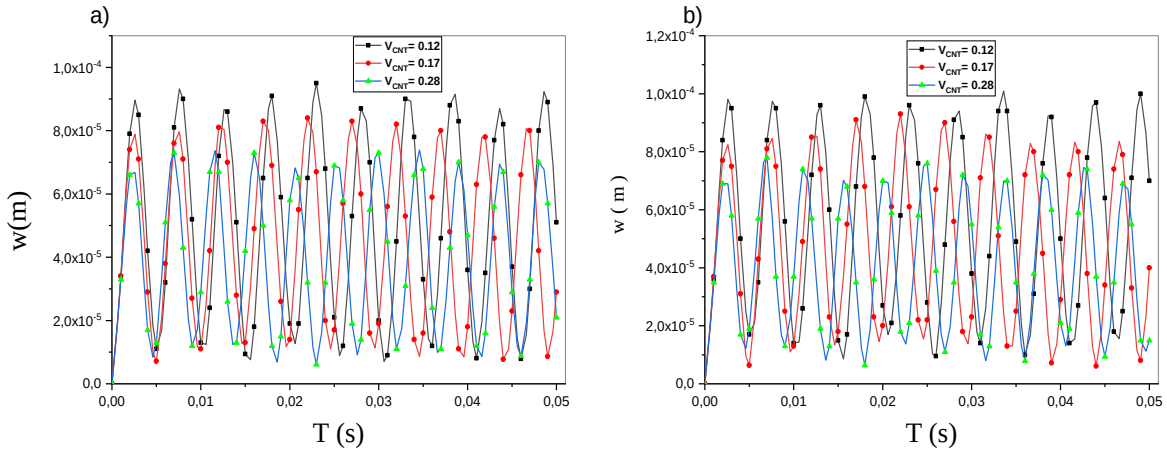


Figure 7.11 : Influence of CNT volume fraction on the undamped response of central deflection of the simply supported square FGM sandwich plate ($a/h = 20$): $a)1-6-1, b)1-8-1$

To examine the influence of mechanical loading on the dynamic response behavior, figure 7.12 illustrates the undamped central deflection of various FGM porous sandwich plates reinforced with CNTs ($1-1-1, 1-2-1$, and $1-8-1$) for a volume fraction exponent of ($n = 2$). The constant loads considered are $C_0 = 6\,000$ N, $8\,000$ N and $10\,000$ N. It is observed that the deflection amplitude increases with the magnitude of the applied load C_0 .

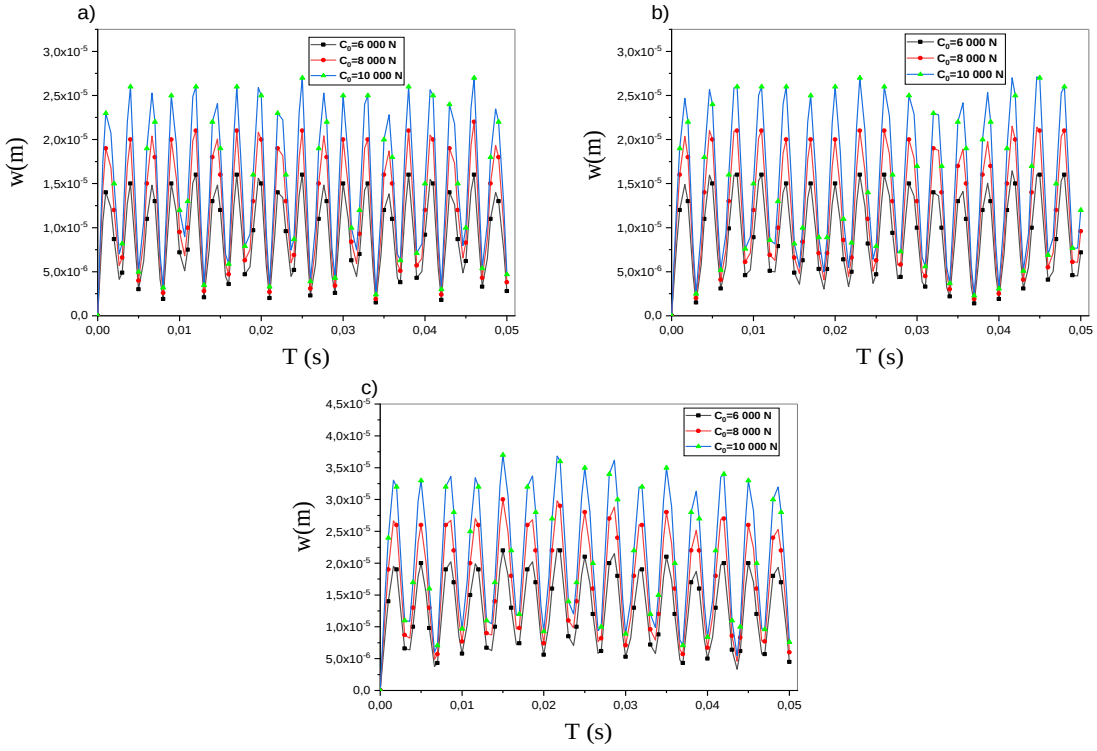


Figure 7.12 : Effect of mechanical loads on the dynamic response of the central deflection of simply supported FG-CNTR sandwich plate (UD; a/h = 10; $e = 0.1; V^*_{CNT} = 0.12$): $a)\ 1-1-1, b)1-2-1, c)1-8-1$.

As shown in figure 7.13, two types of FGM porous sandwich plates with CNT-reinforced cores, namely 1-2-1 and 1-8-1, are analyzed. The study is conducted for a volume fraction exponent of ($n = 5$), porosity coefficients ($e = 0.1$), and a CNT volume fraction $V_{CNT}^{*} = 0.12$) with uniform distribution, while considering different damping ratios ($\xi = 0, 0.1$, and 0.2). It is observed that the central deflection reaches its maximum when the damping ratio is low; in other words, the amplitude of vibration increases as the damping ratio decreases.

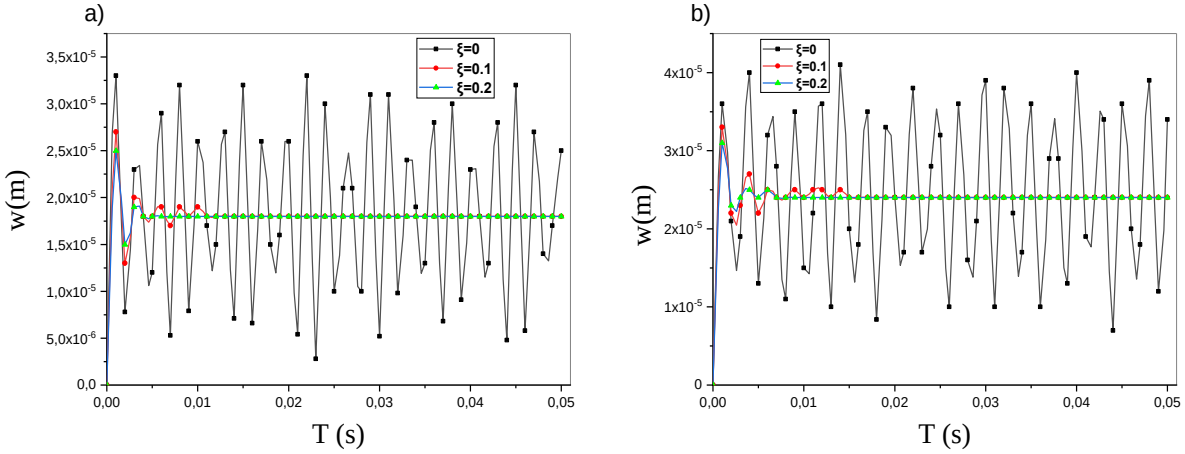


Figure 7.13 : Effect of damping coefficient on the dynamic response of simply supported FG-CNTR sandwich plate ($a/h = 10$; $C_0 = 8\,000$ N): $a) 1-2-1, b) 1-8-1$.

Figure 7.14 illustrates the effect of different porosity models (Perfect, Imperfect I,…,V) and CNT distributions (UD, FG-X, and FG-O) on the static response of the FG-CNTR sandwich plate. The analysis was performed for the 1–2–1 plate configuration. It can be observed that the Imperfect I porosity model with FG-X CNT distribution produces the largest deflection.

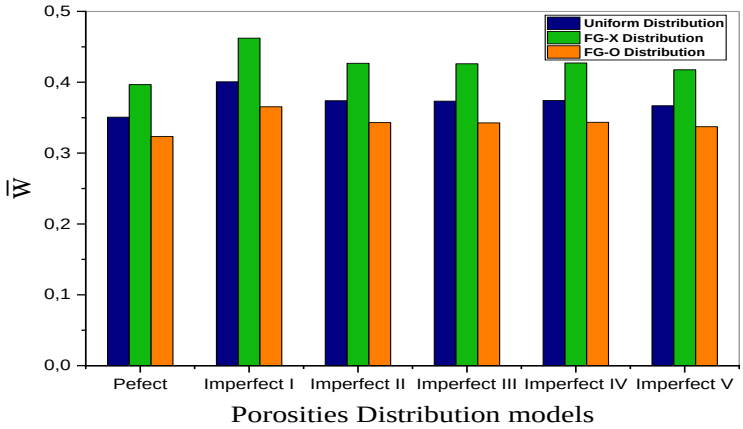


Figure 7.14 : Influence of CNT distribution on the dimensionless central deflection of FG-CNTR sandwich plate with different porosities models ($a/h = 10$; $n = 2$; $e = 0.1$; $V_{CNT}^{*} = 0.17$)

In the context of dynamic response, two types of square sandwich FGM plates: 1-8-1, which is symmetric, and 2-2-1, which is non-symmetric with uniform distribution of CNT are studied, where $e = 0.1$, and $C_0 = 8000$ N. It is observed from the graph presented in figure 7.15 that the Imperfect I model, which represents the even porosity distribution, can be clearly distinguished from the others, while the curves of the uneven porosity models (Imperfect II–V) overlap and cannot be easily distinguished.

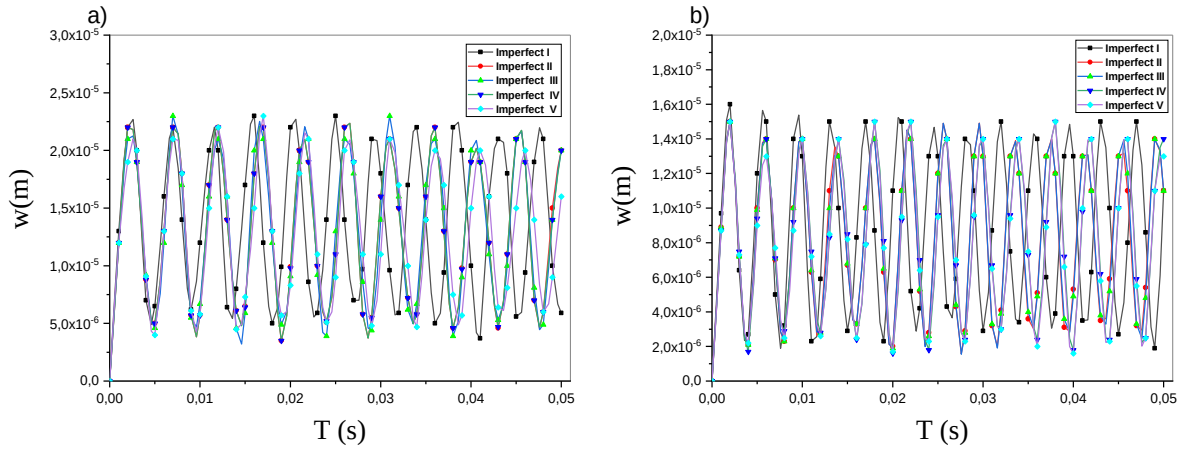


Figure 7.15 : The dynamic behavior of simply supported FG-CNTR sandwich plate ($n = 1;\ a/b = 1;\ a/h = 10$): a) $1-8-1, b)\ 2-2-1$

In all the previous analyses, the simply supported boundary condition was adopted. In this section, various boundary conditions are examined to emphasize their importance and influence on the static and dynamic behavior of the structure. Three cases are considered: fully simply supported (SSSS), fully clamped (CCCC), and clamped at two opposite edges while simply supported along the others (CSCS).

For the static analysis, two separate studies are conducted. The first investigates the effect of boundary conditions on the dimensionless central deflection by varying the a/h ratio, as shown in the figure 7.16, while the second examines the influence of the same boundary conditions for different plate as illustrated in figure 7.17 to explain clearly the important role of use different configuration of sandwich FGM plate. From the graphs, the highest value of dimensionless central deflection is observed for the SSSS symmetric plate (2-1-2), while the lowest deflection amplitude occurs for the non-symmetric CCCC plate (2-2-1). This confirms the significant influence of both the selected FGM sandwich plate configuration and the applied boundary conditions. The CCCC plate exhibits greater rigidity because the clamped edges restrain both rotations and transverse displacements, thereby providing higher stiffness against bending. After analyzing the static behavior, attention is now focused on the dynamic response

of the FG-CNTR sandwich plate to investigate how different boundary conditions influence the undamped response of the central deflection over time, for this study three distributions of CNT: UD, FG-O, and FG-X are presented in figure 7.18. The maximum central deflection is obtained for the SSSS boundary condition with the FG-X CNT distribution, whereas the CCCC configuration exhibits the lowest deflection amplitude.

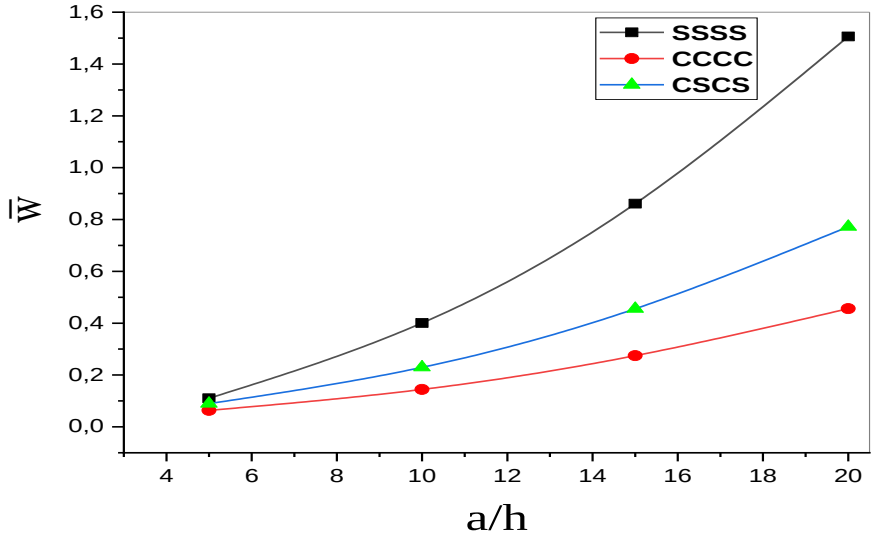


Figure 7.16 : Influence of boundary conditions on the dimensionless central deflection of square FG-CNTR (1–2–1) sandwich plate (UD; $n = 2;\ e = 0.1;\ V^*_{CNT} = 0.17$)

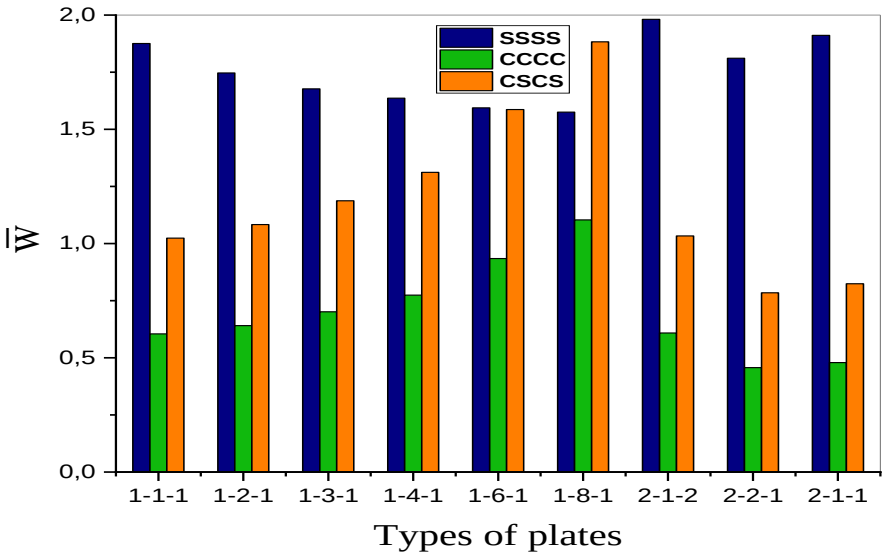


Figure 7.17 : The dimensionless central deflection of FG-CNTR porous sandwich plate for different configurations of plates under various boundary conditions (UD; n = 2; e = 0.1; $V^*_{CNT} = 0.17$)

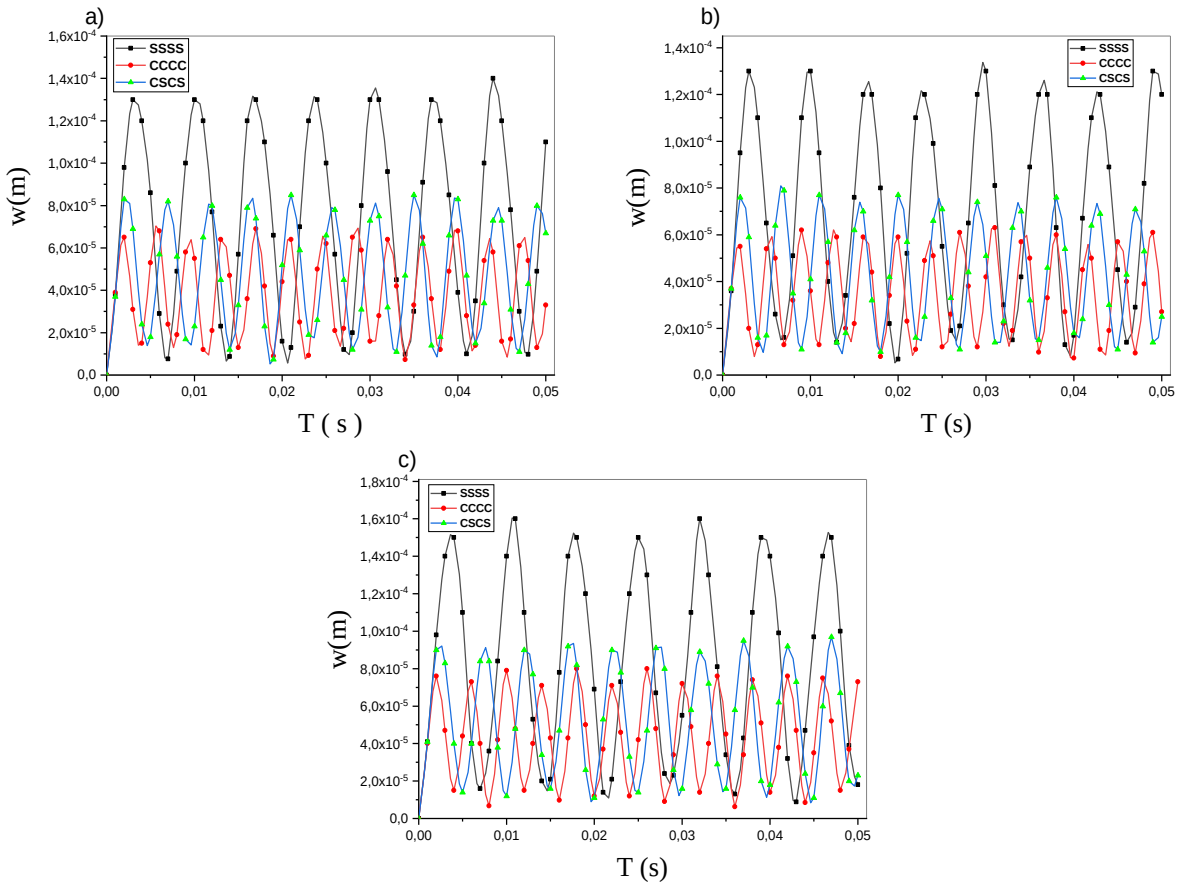


Figure 7.18 : Influence of boundary conditions on the undamped response of the central deflection of square FG-CNTR sandwich plate ($a/h = 10; C_0 = 10\,000$ N, $n = 5$; $e = 0.1$): a) UD, b) FG-O distribution, c) FG-X distribution.

Specifically, a porous FGM sandwich plate with a CNT-reinforced core is analyzed under the conditions $n = 2$, porosity model Imperfect I with $e = 0.2$, CNT volume fraction $V^*_{CNT} = 0.17$, and applied load $C_0 = 8\,000$ N. Figures 7.19 and 7.20 illustrate the influence of geometric parameters namely, the thickness-to-length ratio (h/a) and the length-to-width ratio (a/b) on the undamped central deflection response. It is observed that the amplitude of the central deflection decreases as both (h/a) and (a/b) increase. This behavior highlights the significant role of geometric configuration: increasing the plate thickness or reducing its aspect ratio enhances its global stiffness, thereby reducing the overall deflection amplitude.

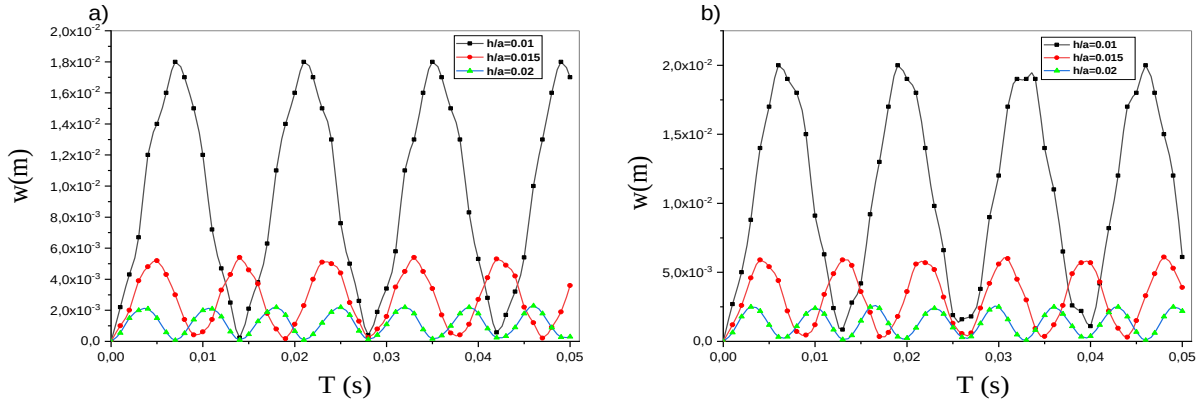


Figure 7.19 : Influence of ratio h/a on the dynamic response of simply supported FG-CNTR sandwich plate (UD; $a/b = 1$): a) $1-2-1$, b) $1-8-1$

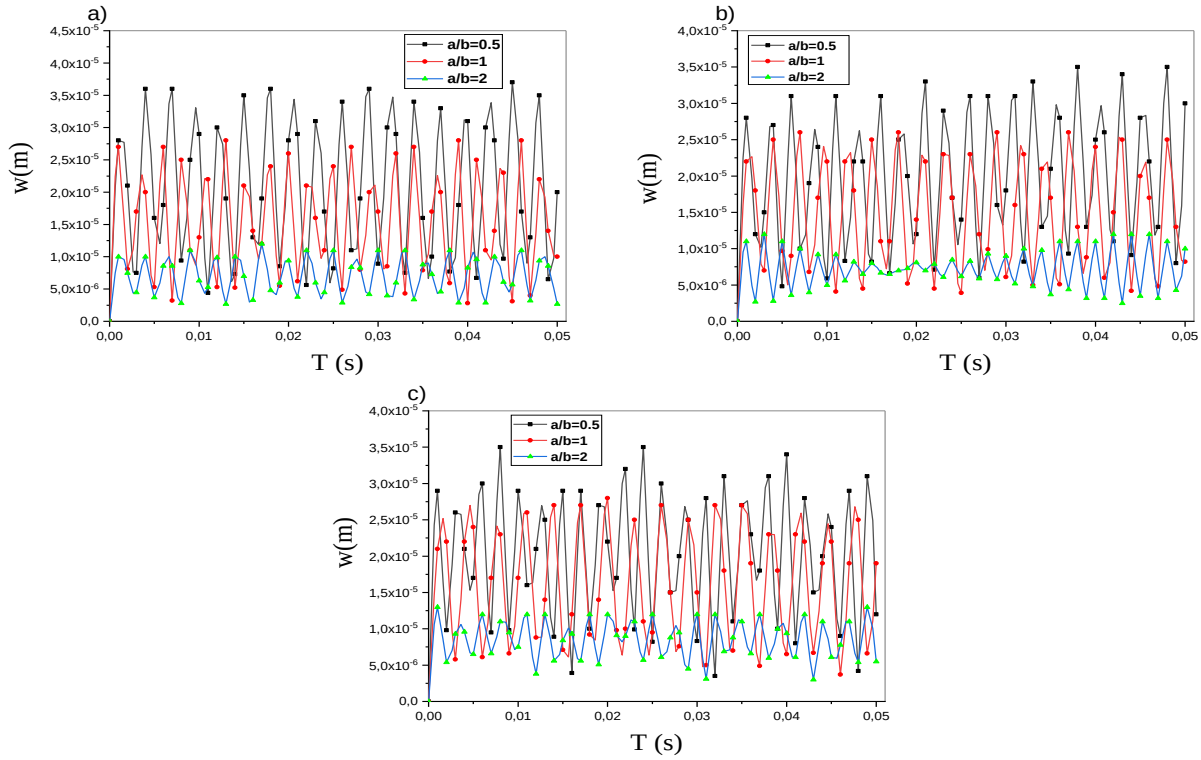


Figure 7.20 : Dynamic behavior of simply supported FG-CNTR sandwich plate with the influence of ratio a/b (UD; $a/h = 10$): a) $1-1-1$, b) $1-2-1$, c) $1-4-1$.

Figure 7.21 presents the variation of the central deflection corresponding to different sandwich plate configurations under the conditions $e = 0.1$, $n = 2$, and $V_{CNT}^{*} = 0.12$. It is observed that the 1-0-1 plate exhibits the highest deflection amplitude, which can be attributed to the absence of a core layer. This configuration, consisting solely of two porous FGM face sheets of equal thickness, possesses lower overall stiffness, leading to a greater deformation response.

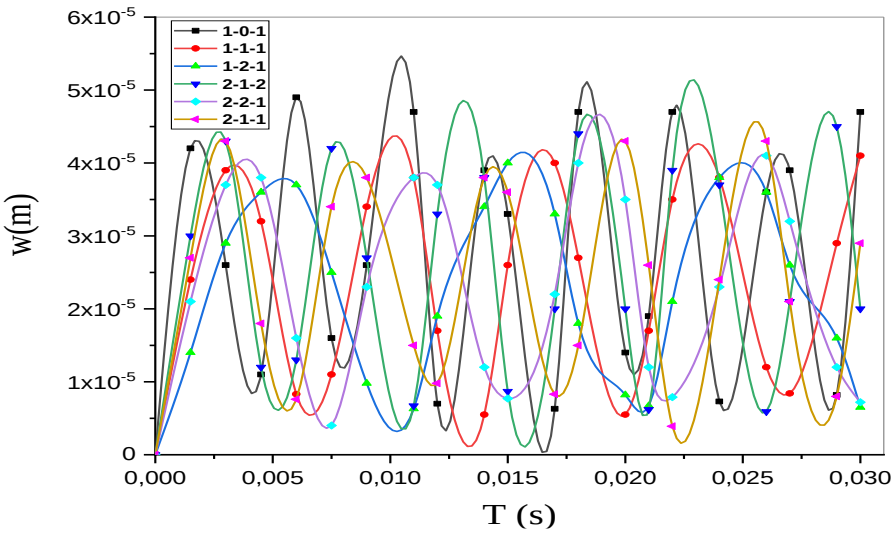


Figure 7.21 : Dynamic response analysis for different models of simply supported FG-CNTR sandwich plate ($a/b = 1;\ a/h = 10;\ C_0 = 10\ 000$ N).

To clearly demonstrate the influence of different parameters on the static response of simply supported square FG-CNTR porous sandwich plates, the first mode shape is plotted by systematically varying several key factors, including the volume fraction exponent, porosity coefficient, CNT volume fraction, and the core-to-facesheet thickness ratio h_c/h_f.

Figure 7.22 illustrates the effect of different volume fraction exponents on the dimensionless central deflection of the 1-2-1 plate with the even porosity model “Imperfect I.” It is observed that increasing the volume fraction exponent results in a higher deflection amplitude, indicating a reduction in the effective stiffness of the graded material.

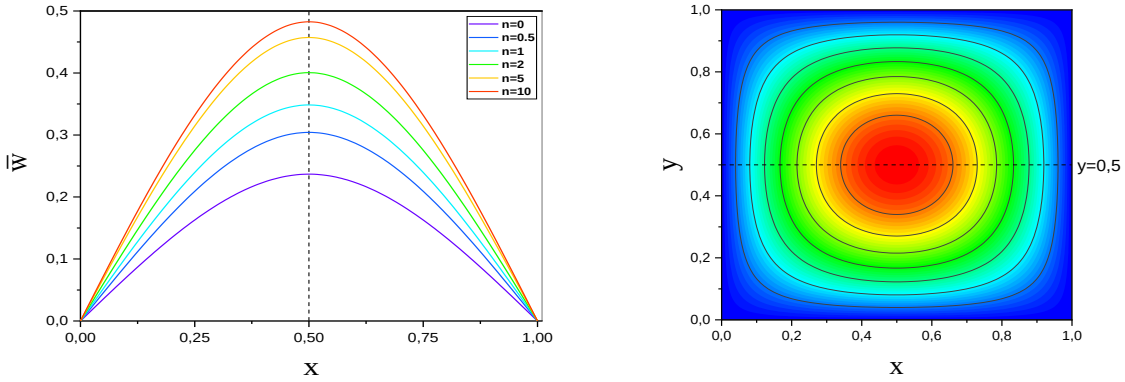


Figure 7.22 : Influence of volume fraction exponent on dimensionless central deflection of simply supported square FG-CNTR sandwich plate for the first mode (UD, a/h = 10; e=0.1; $V^*_{CNT} = 0.17$)

Figure 7.23 presents the influence of the porosity coefficient on the central deflection of the CNT-reinforced porous FGM sandwich plate. Under identical conditions, an increase in the

porosity coefficient leads to a higher central deflection, which is attributed to the reduction in the effective stiffness of the material caused by the presence of pores.

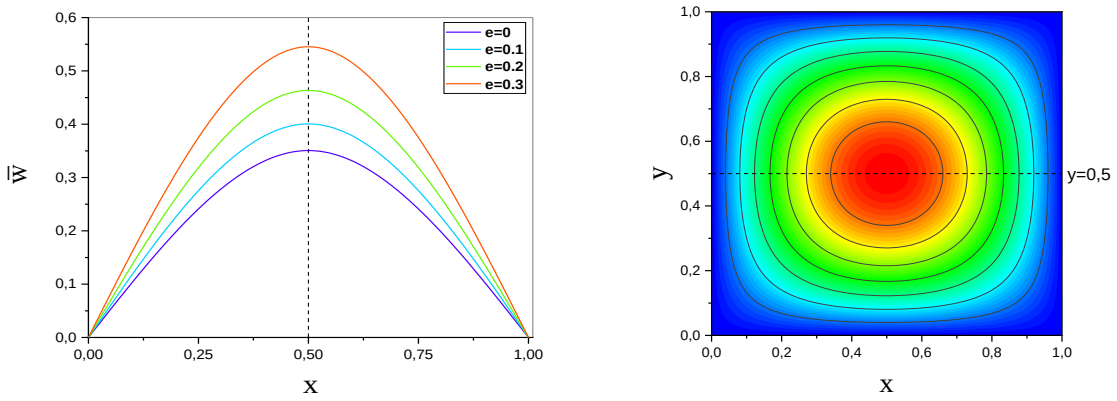


Figure 7.23 : Effect of coefficient of porosity on dimensionless central deflection of simply supported square FG-CNTR sandwich plate for the first mode (UD, a/h = 10; n=2; $V_{CNT}^{*} = 0.17$)

Figure 7.24 illustrates the static response of the porous FGM sandwich plate considering three different CNT volume fractions, $V_{CNT}^{*} = 0.12, 0.17$ and 0.28. It is clearly observed that increasing the CNT volume fraction leads to a decrease in the central deflection. This behavior indicates that the CNT volume fraction plays a crucial role in enhancing the overall stiffness of the FGM sandwich structure, thereby reducing its deformation and improving its vibration resistance.

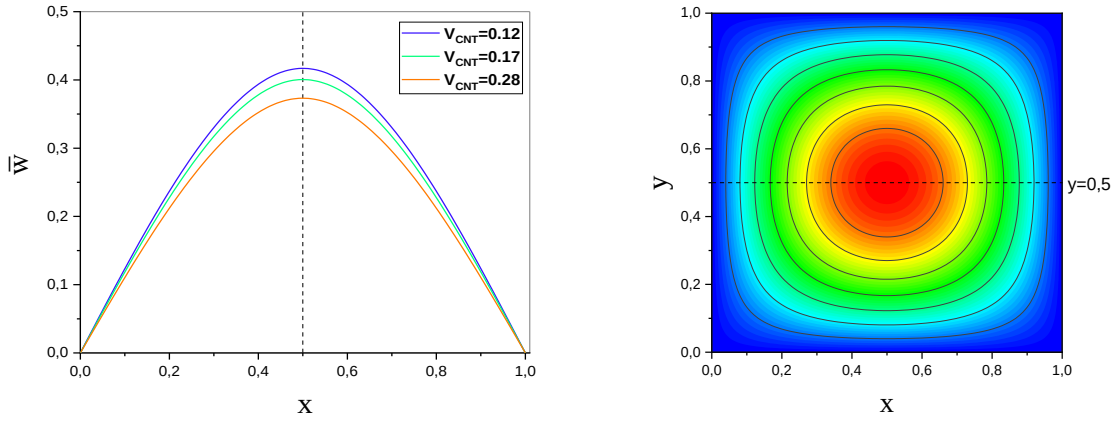


Figure 7.24 : Influence of CNT volume fraction on dimensionless central deflection of simply supported square FG-CNTR sandwich plate for the first mode (UD; $a/h = 10$; $e = 0.1$; $n = 2$; $h_c/h_f = 2$)

Under the same conditions, an additional study is carried out to examine the effect of the core-to-face sheet thickness ratio (h_c/h_f). As shown in Figure 7.25, the central deflection of the simply supported square FGM sandwich plate increases with increasing h_c/h_f. This

behavior can be explained by the reduction in core stiffness associated with a higher h_c/h_f ratio, which makes the structure more flexible and results in greater deflection.

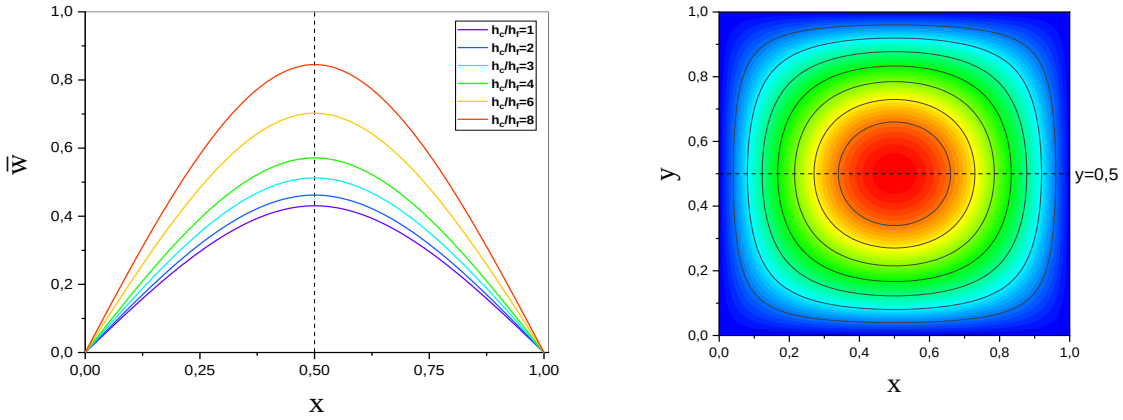


Figure 7.25 : Effect of core-to-face sheet thickness ratio h_c/h_f on dimensionless central deflection of simply supported square FG-CNTR sandwich plate for the first mode (FG-X; a/h = 10; n=2; $V_{CNT}^{*} = 0.17$)

The results obtained clearly demonstrate that the static response of FG-CNTR porous sandwich plates is highly sensitive to both material and geometric parameters. It is evident that the overall structural stiffness is governed by the combined effect of the volume fraction exponent, porosity coefficient, CNT reinforcement, and core-to-face sheet thickness ratio.

An increase in the volume fraction exponent leads to a noticeable rise in the central deflection, which can be attributed to the reduction in the effective stiffness associated with a less favorable distribution of the graded constituents. Similarly, the porosity coefficient significantly affects the mechanical behavior of the structure. Higher porosity levels introduce additional voids within the material, thereby decreasing its load-bearing capacity and increasing the central deflection.

In contrast, the incorporation of carbon nanotubes enhances the stiffness of the sandwich structure. An increase in the CNT volume fraction results in a reduction of the central deflection, confirming the reinforcing effect of CNTs in improving the mechanical performance of FG-CNTR porous plates.

Furthermore, the core-to-face sheet thickness ratio h_c/h_f plays a crucial role in governing the global response of the structure. An increase in this ratio leads to higher deflection values, which is mainly due to the relative reduction in the contribution of the face sheets to the overall bending stiffness, resulting in a more flexible configuration. Overall, the presented results highlight the possibility of tailoring the mechanical response of FG-CNTR porous sandwich

plates through an appropriate selection of material gradation parameters, porosity distribution, CNT content, and geometric configuration.

General Conclusions and Perspectives

The finite element formulation and its evaluation models for structural analysis represent one of the major research areas in solid and structural modeling. Within this framework, the present study falls and aims to provide theoretical and numerical study devoted to the development of a finite element model for both static and dynamic analysis of porous FGM sandwich plate structures reinforced with carbon nanotubes (CNTs). This study investigates the effect of various parameters on the behavior of rectangular plates, using the First-order Shear Deformation Theory (FSDT), which considers the effects of transverse shear deformation and rotary inertia in static and dynamic responses. The central deflection of the plate under constant loading is determined employing the p-version of the Finite Element Method (FEM). A rectangular quadrilateral p-element is employed in this study. The hierarchical shape functions for the quadrilateral p-element are constructed based on orthogonal Legendre polynomials. The equations of motion for the vibration are obtained by applying Lagrange's equation. The present plate is composed of three layers: a core layer made of functionally graded carbon nanotube-reinforced composite (FG-CNTRC), and top and bottom face sheets consisting of porous functionally graded materials (FGMs). From the findings of this study, several significant conclusions can be highlighted:

1. The First-order Shear Deformation Theory is particularly suitable for modeling moderately thick porous sandwich FG-CNTR plates and for studying their static and dynamic behaviors.
2. The monotonic and uniform convergence of the rectangular p-element is examined by increasing the interpolation polynomial degree p. The numerical results demonstrate excellent agreement with available literature solutions for the static analysis and with the analytical solution for the dynamic analysis.
3. The ratio h_c/h_f has an important effect on the central deflection amplitude, with the vibration response increasing progressively as the h_c/h_f ratio is raised.

4. The CNT volume fraction has a notable effect on the vibrations of a porous FGM sandwich plate with CNT-reinforced core, with higher CNT content leading to reduced deflection.

5. Regarding reinforcement with CNTs, the FG-X distribution has more pronounced effect on static and dynamic behaviors of the central deflection, due to the higher concentration of carbon nanotubes near the surfaces, which enhances the stiffness of the plate.

6. The geometry of the plate plays significant role in its static and dynamic responses. Both the thickness ratio and the length-to-width ratio exhibit similar effects: increasing either of these parameters leads to reduction in the vibration amplitudes.

7. The presence of pores reduces the structural stiffness, which accounts for the observed increase in central deflection as the porosity coefficient rises.

8. Concerning the influence of the volume fraction exponent, it is evident that the static and dynamic central deflection increase as the exponent increases.

9. The dynamic response of the central deflection is inversely affected by variations in the damping coefficient.

10. The analysis of boundary conditions shows that a clamped FG-CNTRC porous sandwich plate exhibits greater stiffness than a simply supported one. This is because clamped edges fully restrain both displacements and rotations, providing stronger constraints that limit deformation, whereas simply supported edges allow rotations, resulting in lower structural rigidity.

The perspectives for future studies are:

- **Experimental validation:** Future work should include experimental testing to validate the numerical predictions, as the absence of experimental data currently limits the reliability of the model.
- **Nonlinear material behavior:** Research should incorporate nonlinear material responses, since the present study assumes linear elastic behavior.
- **Thermo-mechanical coupling:** Future investigations should consider thermal effects and their interaction with mechanical behavior, especially for applications involving temperature gradients or thermal loading.

Bibliography

A. Szabó, Barna. 1986.
Mesh design for the p-version of the finite element method.
Computer Methods in Applied Mechanics and Engineering 55 (1-2): 181-97.
https://doi.org/10.1016/0045-7825(86)90091-5.

Abramowitz, M., Stegun, I.A. 1965.
Handbook of mathematical functions.
Dover Publications, New York.

Adhi, I Gusti Agung Ketut Catur, Ketut Adi Atmika, Ni Made Dwidiani, et I Dewa Gede Ary Subagia. 2024.
Adhesives type on the burning rate and emission properties of honeycomb sandwich composite.
International Journal of Technology 15 (4): 999.
https://doi.org/10.14716/ijtech.v15i4.5728.

Adhikari, Balakrishna, Padmanav Dash, et B.N. Singh. 2020.
Buckling analysis of porous FGM sandwich plates under various types nonuniform edge compression based on higher order shear deformation theory.
Composite Structures 251 112597.
https://doi.org/10.1016/j.compstruct.2020.112597.

A.G. Peano. 1975.
Hierarchies of conforming finite elements.
Washington University.

Ait Atmane, Hassen, Abdelouahed Tounsi, Ismail Mechab, et El Abbas Adda Bedia. 2010.
Free Vibration Analysis of Functionally Graded Plates Resting on Winkler–Pasternak Elastic Foundations Using a New Shear Deformation Theory.
International Journal of Mechanics and Materials in Design 6 (2): 113-21.
https://doi.org/10.1007/s10999-010-9110-x.

Alibeigloo, A., et M. Alizadeh. 2015.
Static and free vibration analyses of functionally graded sandwich plates using state space differential quadrature method.
European Journal of Mechanics - A/Solids 54: 252-66.
https://doi.org/10.1016/j.euromechsol.2015.06.011.

Ansari, Md Irfan, Ajay Kumar, Stanisław Fic, et Danuta Barnat-Hunek. 2018.
Flexural and free vibration analysis of CNT-reinforced functionally graded plate.
Materials 11 (12): 2387.
https://doi.org/10.3390/ma11122387.

Aydogdu, Metin. 2009.
A new shear deformation theory for laminated composite plates.
Composite Structures 89 (1) : 94-101.
https://doi.org/10.1016/j.compstruct.2008.07.008.

Babuska, I., B. A. Szabo, et I. N. Katz. 1981.
The *p*-version of the finite element method.
SIAM Journal on Numerical Analysis 18 (3): 515-45.
https://doi.org/10.1137/0718033.

Babuška, Ivo, et Manil Suri. 1990.
The p- and h-p versions of the finite element method, an overview.
Computer Methods in Applied Mechanics and Engineering 80 (1-3): 5-26.
https://doi.org/10.1016/0045-7825(90)90011-a.

Bao, G., et L. Wang. 1995.
Multiple cracking in functionally graded ceramic/metal coatings.
International Journal of Solids and Structures 32 (19): 2853-71.
https://doi.org/10.1016/0020-7683(94)00267-z.

Belalia, S. A. 2017.
A new analysis of nonlinear free vibration behavior of bi-functionally graded sandwich plates using the p -version of the finite element method.
Mechanics of Advanced Materials and Structures 26 (8): 727-40.
https://doi.org/10.1080/15376494.2017.1410912.

Belalia Sid Ahmed. 2011.
Développement d'éléments finis courbés version-p pour les plaques de formes géométriques arbitraires.
University of Tlemcen.

Belalia, Sid Ahmed. 2019.
Investigation of the mechanical properties on the large amplitude free vibrations of the functionally graded material sandwich plates.
Journal of Sandwich Structures & Materials 21 (3): 895-916.
https://doi.org/10.1177/1099636217701299.

Belarbi, Mohamed-Ouejdi, Ahmed Amine Daikh, Aman Garg, et al. 2022.
Bending and free vibration analysis of porous functionally graded sandwich plate with various porosity distributions using an extended layerwise theory.
Archives of Civil and Mechanical Engineering 23 (1): 15.
https://doi.org/10.1007/s43452-022-00551-0.

Belkhodja, Yamna, Mohamed El Amine Belkhodja, Hamida Fekirini, et Djamel Ouinas. 2023.
New quasi-three, and two-dimensional trigonometric-cubic monomial HSDT for thermal buckling and thermo-mechanical bending analyses of FGM Symmetrical/non-symmetrical sandwich plates with hard/soft core.
Composite Structures 304 : 116402.
https://doi.org/10.1016/j.compstruct.2022.116402.

Bentrar, Hakim, Sidi Mohammed Chorfi, Sid Ahmed Belalia, Abdelouahed Tounsi, Mofareh Hassan Ghazwani, et Ali Alnujaie. 2023.
Effect of porosity distribution on free vibration of functionally graded sandwich plate using the p-version of the finite element method.
Structural Engineering and Mechanics 88 (6): 551-67.
https://doi.org/10.12989/SEM.2023.88.6.551.

Berreur, Louis. 2002.
L'industrie française des matériaux composites, DiGITIP / SIM, Ministry of Economy, Finance and Industry.

Bidgoli, E. Mohammad-Rezaei, et Mohammad Arefi. 2023.
Effect of porosity and characteristics of carbon nanotube on the nonlinear characteristics of a simply-supported sandwich plate.
Archives of Civil and Mechanical Engineering 23 (3): 214.
https://doi.org/10.1007/s43452-023-00752-1.

Burlayenko, Vyacheslav N., et Tomasz Sadowski. 2020.
Free vibrations and static analysis of functionally graded sandwich plates with three-dimensional finite elements.
Meccanica 55 (4): 815-32.
https://doi.org/10.1007/s11012-019-01001-7.

Carnevali, P., R. B. Morris, Y. Tsuji, et G. Taylor. 1993.
New basis functions and computational procedures for p-version finite element analysis.
International Journal for Numerical Methods in Engineering 36 (22): 3759-79.
https://doi.org/10.1002/nme.1620362202.

Chen, Weinong W., A. M. Rajendran, Bo Song, et Xu Nie. 2007.
Dynamic fracture of ceramics in armor applications.
Journal of the American Ceramic Society 90 (4): 1005-18.
https://doi.org/10.1111/j.1551-2916.2007.01515.x.

Chi, Shyang-ho, et Yen-Ling Chung. 2003.
Cracking in coating–substrate composites with multi-layered and FGM coatings.
Engineering Fracture Mechanics 70 (10): 1227-43.
https://doi.org/10.1016/s0013-7944(02)00114-5.

Chung, D. D. L. 2002.
Review Graphite.
Journal of Materials Science 37 (8): 1475-89.
https://doi.org/10.1023/a:1014915307738.

Cook, R.D., Malkus, D.S., and Plesha, M.E. 1989.
Concepts and applications of finite element analysis.
John Wiley & Sons. Inc, New York, 3rd Ed.

D. Baptiste, R. O. Polit, R. A. Chabot, E. M. Boussu, and J. F. Caron. 2004.
Modelisation globale et locale des structures multicouches par elements finis de plaque, 'Viet Tung NGUYEN'.

Daikh, Ahmed Amine, et Ashraf M Zenkour. 2019a.
Effect of porosity on the bending analysis of various functionally graded sandwich plates.
Materials Research Express 6 (6): 065703.
https://doi.org/10.1088/2053-1591/ab0971.

Daikh, Ahmed Amine, et Ashraf M Zenkour. 2019b.

Free vibration and buckling of porous power-law and sigmoid functionally graded sandwich plates using a simple higher-order shear deformation theory.
Materials Research Express 6 (11): 115707.
https://doi.org/10.1088/2053-1591/ab48a9.

Daniel, Isaac M., et Ori Ishai. 2006.
Engineering mechanics of composite materials. 2nd ed.
Oxford University Press.

Dat, Ngo Dinh, Nguyen Van Thanh, Vu MinhAnh, et Nguyen Dinh Duc. 2022.
Vibration and nonlinear dynamic analysis of sandwich FG-CNTRC plate with porous core layer.
Mechanics of Advanced Materials and Structures 29 (10): 1431-48.
https://doi.org/10.1080/15376494.2020.1822476.

Dat, Pham Tien, Do Van Thom, et Doan Trac Luat. 2016.
Free vibration of functionally graded sandwich plates with stiffeners based on the third-order shear deformation theory.
Vietnam Journal of Mechanics 38 (2): 103-22.
https://doi.org/10.15625/0866-7136/38/2/6730.

David R. Lide, ed. 2005.
CRC Handbook of Chemistry and Physics, Internet Version.
http://www.hbcpnetbase.com.

Dawe, D.J. 1978.
Finite Strip Models for Vibration of Mindlin Plates.
Journal of Sound and Vibration 59 (3): 441-52.
https://doi.org/10.1016/s0022-460x(78)80009-1.

Delale, F., et F. Erdogan. 1983.
The Crack Problem for a Nonhomogeneous Plane.
Journal of Applied Mechanics 50 (3): 609-14.
https://doi.org/10.1115/1.3167098.

Demirhan, Pinar Aydan, et Vedat Taskin. 2019.
Bending and free vibration analysis of Levy-Type porous functionally graded plate using state space approach.
Composites Part B: Engineering 160: 661-76.
https://doi.org/10.1016/j.compositesb.2018.12.020.

Dong, C.Y. 2008.
Three-dimensional free vibration analysis of functionally graded annular plates using the Chebyshev–Ritz method.
Materials & Design 29 (8): 1518-25.
https://doi.org/10.1016/j.matdes.2008.03.001.

Dozio, Lorenzo. 2013.
Natural frequencies of sandwich plates with FGM core via variable-kinematic 2-D Ritz models.
Composite Structures 96 : 561-68.

https://doi.org/10.1016/j.compstruct.2012.08.016.

Draoui, Aicha, Mohamed Zidour, Abdelouahed Tounsi, et Belkacem Adim. 2019.
Static and dynamic behavior of nanotubes-reinforced sandwich plates using (FSDT).
Journal of Nano Research 57: 117-35.
https://doi.org/10.4028/www.scientific.net/JNanoR.57.117.

El Meiche, Noureddine, Abdelouahed Tounsi, Noureddine Ziane, Ismail Mechab, et El Abbes Adda.Bedia. 2011.
A New Hyperbolic Shear Deformation Theory for Buckling and Vibration of Functionally Graded Sandwich Plate.
International Journal of Mechanical Sciences 53 (4): 237-47.
https://doi.org/10.1016/j.ijmecsci.2011.01.004.

Elsa Garrido. 2010.
Fonctionnalisation de nanotubes de carbone pour leur incorporation dans des matrices métalliques. Matériaux.
Université Sciences et Technologies - Bordeaux I, Français.

Fazzolari, Fiorenzo A. 2015.
Natural frequencies and critical temperatures of functionally graded sandwich plates subjected to uniform and non-uniform temperature distributions.
Composite Structures 121 : 197-210.
https://doi.org/10.1016/j.compstruct.2014.10.039.

Ghazwani, Mofareh Hassan. 2024.
A novel Nth-order shear deformation theory for the bending and free vibration analysis of bi-functionally graded sandwich plates.
Iranian Journal of Science and Technology, Transactions of Civil Engineering 48 (1): 239-70.
https://doi.org/10.1007/s40996-023-01162-2.

Hajmohammad, Mohammad Hadi, Reza Kolahchi, Mohammad Sharif Zarei, et Amir Hossein Nouri. 2019.
Dynamic response of auxetic honeycomb plates integrated with agglomerated CNT-Reinforced face sheets subjected to blast load based on visco-sinusoidal theory.
International Journal of Mechanical Sciences 153-154: 391-401.
https://doi.org/10.1016/j.ijmecsci.2019.02.008.

Herrmann, Michael, et Werner Sobek. 2017.
Functionally graded concrete: numerical design methods and experimental tests of mass-optimized structural components.
Structural Concrete 18 (1): 54-66.
https://doi.org/10.1002/suco.201600011.

Hirsch, Andreas. 2002.
Functionalization of Single-Walled Carbon Nanotubes.
Angewandte Chemie International Edition 41 (11): 1853.
https://doi.org/10.1002/1521-3773(20020603)41:11<1853::aid-anie1853>3.0.co;2-n.

Houmat, A. 1997.

Hierarchical finite element analysis of the vibration of membranes.
Journal of Sound and Vibration 201 (4): 465-72.
https://doi.org/10.1006/jsvi.1996.0779.

Houmat, A. 2000.
A triangular fourier p -element for the analysis of membrane vibrations.
Journal of Sound and Vibration 230 (1): 31-43.
https://doi.org/10.1006/jsvi.1999.2613.

Houmat, A. 2001.
A sector Fourier p-element applied to free vibration analysis of sectorial plates.
Journal of Sound and Vibration 243 (2): 269-82.
https://doi.org/10.1006/jsvi.2000.3410.

Houmat, A. 2001.
A sector Fourier P-Element for free vibration analysis of sectorial membranes.
Computers & Structures 79 (12): 1147-52.
https://doi.org/10.1016/s0045-7949(01)00013-x.

Houmat, A. 2004.
Three-dimensional hierarchical finite element free vibration analysis of annular sector plates.
Journal of Sound and Vibration 276 (1-2): 181-93.
https://doi.org/10.1016/j.jsv.2003.07.020.

Houmat A. 2022.
Course Dynamic Response.

I.N. Katz, A.G. Peano and M.P. Rossow. 1978.
Nodal variables tbr complete conforming finite elements of arbitrary polynomial order.
Comp. Math, Appl. 4, pp. 85 112.

Iyengar, K. T. Sundara Raja, K. Chandrashekhara, et V. K. Sebastian. 1974.
On the Analysis of Thick Rectangular Plates.
Ingenieur-Archiv 43 (5) : 317-30.
https://doi.org/10.1007/bf00537220.

Jang, Jaewon, Maydison Maydison, Yeonjun Kim, Zhiqiang Han, et Daekyun Oh. 2023.
Effect of void content on the mechanical properties of GFRP for ship design.
Journal of Marine Science and Engineering 11 (6): 1251.
https://doi.org/10.3390/jmse11061251.

Karama, M., K.S. Afaq, et S. Mistou. 2003.
Mechanical behaviour of laminated composite beam by the new multi-layered laminated composite structures model with transverse shear stress continuity.
International Journal of Solids and Structures 40 (6): 1525-46.
https://doi.org/10.1016/s0020-7683(02)00647-9.

Karami, Behrouz, Davood Shahsavari, Maziar Janghorban, et Li Li. 2019.
Influence of homogenization schemes on vibration of functionally graded curved microbeams.

Composite Structures 216 : 67-79.
https://doi.org/10.1016/j.compstruct.2019.02.089.

Kausar, Ayesha, Ishaq Ahmad, Sobia A. Rakha, M. H. Eisa, et Abdoulaye Diallo. 2023.
State-of-the-art of sandwich composite structures: manufacturing to high performance applications.
Journal of Composites Science 7 (3): 102.
https://doi.org/10.3390/jcs7030102.

Kiani, Y. 2017.
Free vibration of FG-CNT reinforced composite spherical shell panels using gram-schmidt shape functions.
Composite Structures 159 : 368-81.
https://doi.org/10.1016/j.compstruct.2016.09.079.

Kiani, Y, E Bagherizadeh, et M R Eslami. 2012.
Thermal and mechanical buckling of sandwich plates with FGM face sheets resting on the pasternak elastic foundation.
Proceedings of the Institution of Mechanical Engineers, Part C: Journal of Mechanical Engineering Science 226 (1): 32-41.
https://doi.org/10.1177/0954406211413657.

Kim, Seung-Eock, Huu-Tai Thai, et Jaehong Lee. 2009.
Buckling analysis of plates using the two variable refined plate theory.
Thin-Walled Structures 47 (4): 455-62.
https://doi.org/10.1016/j.tws.2008.08.002.

Koizumi, M. 1997.
FGM Activities in Japan.
Composites Part B: Engineering 28 (1-2): 1-4.
https://doi.org/10.1016/S1359-8368(96)00016-9.

Krishna Murty, A.V. 1987.
Flexure of Composite Plates.
Composite Structures 7 (3) : 161-77.
https://doi.org/10.1016/0263-8223(87)90027-4.

Kumar Sah, Supen, et Anup Ghosh. 2022.
Influence of porosity distribution on free vibration and buckling analysis of multi-directional functionally graded sandwich plates.
Composite Structures 279 : 114795.
https://doi.org/10.1016/j.compstruct.2021.114795.

L. Hadji, H. A. Atmane, A. Tounsi, I. Mechab & E. A. Adda Bedia. 2011.
Free vibration of functionally graded sandwich plates using four-variable refined plate theory.
https://doi.org/10.1007/s10483-011-1470-9.

Lakhdar, Zeddoune, Sidi Mohammed Chorfi, Sid Ahmed Belalia, et al. 2024.
Free vibration and bending analysis of porous bi-directional FGM sandwich shell using a TSDT p-version finite element method.

Acta Mechanica 235 (6): 3657-86.
https://doi.org/10.1007/s00707-024-03909-y.

Lei, Z.X., L.W. Zhang, et K.M. Liew. 2016.
Vibration of FG-CNT reinforced composite thick quadrilateral plates resting on pasternak foundations.
Engineering Analysis with Boundary Elements 64: 1-11.
https://doi.org/10.1016/j.enganabound.2015.11.014.

Li, Q., V.P. Iu, et K.P. Kou. 2008.
Three-dimensional vibration analysis of functionally graded material sandwich plates.
Journal of Sound and Vibration 311 (1-2): 498-515.
https://doi.org/10.1016/j.jsv.2007.09.018.

Liang, Chen, et Yan Qing Wang. 2020.
A Quasi-3D trigonometric shear deformation theory for wave propagation analysis of FGM sandwich plates with porosities resting on viscoelastic foundation.
Composite Structures 247 : 112478.
https://doi.org/10.1016/j.compstruct.2020.112478.

Liew, K.M., Wang, C.M., Xiang, Y., and Kitipornchai, S. 1998.
Vibration of Mindlin plates: programming the p-version Ritz method.
Elsevier.

Liu, Ming, Jun Liu, et Yuansheng Cheng. 2018.
High-Order free vibration analysis of FGM sandwich plates with non-monotonically graded flexible core.
Journal of Sandwich Structures & Materials 20 (6): 759-80.
https://doi.org/10.1177/1099636216680397.

Loja, M.A.R., C.M. Mota Soares, et J.I. Barbosa. 2013.
Analysis of functionally graded sandwich plate structures with piezoelectric skins, using b-spline finite strip method.
Composite Structures 96 : 606-15.
https://doi.org/10.1016/j.compstruct.2012.08.010.

Mahamood, Rasheedat Modupe, et Esther Titilayo Akinlabi. 2017.
Types of Functionally Graded Materials and Their Areas of Application.
In Functionally Graded Materials, par Rasheedat Modupe Mahamood et Esther Titilayo Akinlabi. Topics in Mining, Metallurgy and Materials Engineering.
Springer International Publishing.
https://doi.org/10.1007/978-3-319-53756-6_2.

Mahi, Amale, El Abbas Adda Bedia, et Abdelouahed Tounsi. 2015.
A new hyperbolic shear deformation theory for bending and free vibration analysis of isotropic, functionally graded, sandwich and laminated composite plates.
Applied Mathematical Modelling 39 (9): 2489-508.
https://doi.org/10.1016/j.apm.2014.10.045.

Mallikarjuna, et T. Kant. 1993.

A critical review and some results of recently developed refined theories of fiber-reinforced laminated composites and sandwiches.
Composite Structures 23 (4) : 293-312.
https://doi.org/10.1016/0263-8223(93)90230-n.

Mantari, J.L., A.S. Oktem, et C. Guedes Soares. 2012.
A new higher order shear deformation theory for sandwich and composite laminated plates.
Composites Part B: Engineering 43 (3): 1489-99.
https://doi.org/10.1016/j.compositesb.2011.07.017.

Marshall, A. 1982.
Sandwich Construction.
In *Handbook of Composites*, Springer US.
https://doi.org/10.1007/978-1-4615-7139-1_21.

Matsuo, Shingo, Fumio Watari, et Noboru Ohata. 2001.
Fabrication of a functionally graded dental composite resin post and core by laser lithography and finite element analysis of its stress relaxation effect on tooth root.
Dental Materials Journal 20 (4): 257-74.
https://doi.org/10.4012/dmj.20.257.

Medani, Mohammed, Abdelillah Benahmed, Mohamed Zidour, et al. 2019.
Static and dynamic behavior of (FG-CNT) reinforced porous sandwich plate using energy principle.
Steel and Composite Structures 32 (5): 595-610.
https://doi.org/10.12989/SCS.2019.32.5.595.

Mindlin, R. D. 1951.
Influence of rotatory inertia and shear on flexural motions of isotropic, elastic plates.
Journal of Applied Mechanics 18 (1): 31-38.
https://doi.org/10.1115/1.4010217.

Mohammadi, Y., et S. M. R. Khalili. 2012.
Free vibration analysis of sandwich plates with temperature-dependent properties of the core materials and functionally graded face sheets.
In Mechanics and Properties of Composed Materials and Structures, Advanced Structured Materials. Springer Berlin Heidelberg.
https://doi.org/10.1007/978-3-642-31497-1_13.

Murty, A. V. Krishna. 1977.
Higher order theory for vibrations of thick plates.
AIAA Journal 15 (12) : 1823-24.
https://doi.org/10.2514/3.7490.

Murty, A. V. Krishna. 1986.
Toward a consistent plate theory.
AIAA Journal 24 (6) : 1047-48.
https://doi.org/10.2514/3.9388.

Nanowerk. 2025.
Introduction to Nanotechnology, [Online]. July 22.
Available:
https://www.nanowerk.com/nanotechnology/introduction/introduction_to_nanotechnology_22.php.

Natarajan, S., et Ganapathi Manickam. 2012.
Bending and vibration of functionally graded material sandwich plates using an accurate theory.
Finite Elements in Analysis and Design 57: 32-42.
https://doi.org/10.1016/j.finel.2012.03.006.

Natarajan, Sundararajan, Mohamed Haboussi, et Ganapathi Manickam. 2014.
Application of higher-order structural theory to bending and free vibration analysis of sandwich plates with CNT reinforced composite facesheets.
Composite Structures 113 : 197-207.
https://doi.org/10.1016/j.compstruct.2014.03.007.

Neves, A.M.A., A.J.M. Ferreira, E. Carrera, M. Cinefra, R.M.N. Jorge, et C.M.M. Soares. 2012.
Static Analysis of functionally graded sandwich plates according to a hyperbolic theory considering zig-zag and warping effects.
Advances in Engineering Software 52: 30-43.
https://doi.org/10.1016/j.advengsoft.2012.05.005.

Nguyen, T.-K., K. Sab, et G. Bonnet. 2007.
Shear correction factors for functionally graded plates.
Mechanics of Advanced Materials and Structures 14 (8): 567-75.
https://doi.org/10.1080/15376490701672575.

Nguyen, Trung-Kien, Thuc P Vo, et Huu-Tai Thai. 2014.
Vibration and buckling analysis of functionally graded sandwich plates with improved transverse shear stiffness based on the first-order shear deformation theory.
Proceedings of the Institution of Mechanical Engineers, Part C: Journal of Mechanical Engineering Science 228 (12): 2110-31.
https://doi.org/10.1177/0954406213516088.

Niino, Masayuki, Katsuto Kisara, et Masahiro Mori. 2005.
Feasibility study of FGM technology in space solar power systems (SSPS).
Materials Science Forum 492-493: 163-70.
https://doi.org/10.4028/www.scientific.net/msf.492-493.163.

O.C. Zienkiewicz, D.W. Kelly, J.P. de S,R. Gago and 1. Babuska. 1981.
Hierarchical finite element approaches, error estimates and adaptive refinement.
in: Proc. MAFELAP, Brunel University, pp. 313-346.

P. M. Naghdi. s. d. 1957.
On the theory of thin elastic shells.
Quarterly Appl. Math, 14: 369-380.

Pandey, Shashank, et S. Pradyumna. 2015a.
An accurate prediction of natural frequencies of sandwich plates with functionally graded material core in thermal environment using a layerwise theory.

In *Advances in Structural Engineering*, Springer India.
https://doi.org/10.1007/978-81-322-2190-6_16.

Pandey, Shashank, et S. Pradyumna. 2015b.
Free vibration of functionally graded sandwich plates in thermal environment using a layerwise theory.
European Journal of Mechanics - A/Solids 51: 55-66.
https://doi.org/10.1016/j.euromechsol.2014.12.001.

Papadrakakis, Manolis, et George P. Babilis. 1994.
Solution techniques for the *p*-version of the adaptive finite element method.
International Journal for Numerical Methods in Engineering 37 (8): 1413-31.
https://doi.org/10.1002/nme.1620370809.

Peano, A., A. Pasini, R. Riccioni, et L. Sardella. 1979.
Adaptive approximations in finite element structural analysis.
Computers & Structures 10 (1-2): 333-42.
https://doi.org/10.1016/0045-7949(79)90102-0.

Peano, Alberto. 1976.
Hierarchies of conforming finite elements for plane elasticity and plate bending.
Computers & Mathematics with Applications 2 (3-4): 211-24.
https://doi.org/10.1016/0898-1221(76)90014-6.

Pereira, António Bastos, et Fábio A.O. Fernandes. 2019.
Sandwich panels bond with advanced adhesive films.
Journal of Composites Science 3 (3): 79.
https://doi.org/10.3390/jcs3030079.

Rai, Saurabh, et Ankit Gupta. 2024.
Dynamic response of sandwich functionally graded nanoplate under thermal environments and elastic foundations using dynamic stiffness method.
Scientific Reports 14 (1).
https://doi.org/10.1038/s41598-024-70210-2.

Rameshchandra P. Shimpi. 2012.
Refined plate theory and its variants.
https://doi.org/10.2514/2.1622.

Reddy, J. N. 1984.
A simple higher-order theory for laminated composite plates.
Journal of Applied Mechanics 51 (4): 745-52.
https://doi.org/10.1115/1.3167719.

Reddy, J. N. 1990.
On refined theories of composite laminates.
Meccanica 25 (4): 230-38.
https://doi.org/10.1007/bf01559685.

Reddy, J. N. 2003.
Mechanics of laminated composite plates and shells.

CRC Press.
https://doi.org/10.1201/b12409.

Reddy, J. N. 2006.
Theory and analysis of elastic plates and shells.
CRC Press.
https://doi.org/10.1201/9780849384165.

Reissner, E. 1975.
On transverse bending of plates, including the effect of transverse shear deformation.
International Journal of Solids and Structures 11 (5): 569-73.
https://doi.org/10.1016/0020-7683(75)90030-x.

Reissner, E., et Y. Stavsky. 1961.
Bending and stretching of certain types of heterogeneous aeolotropic elastic plates.
Journal of Applied Mechanics 28 (3): 402-8.
https://doi.org/10.1115/1.3641719.

Reissner, Eric. 1945.
The effect of transverse shear deformation on the bending of elastic plates.
Journal of Applied Mechanics 12 (2): A69-77.
https://doi.org/10.1115/1.4009435.

Sadollah, Ali, Ardeshir Bahreininejad, Hadi Eskandar, et Mohd Hamdi. 2013.
Optimum material gradient for functionally graded dental implant using particle swarm optimization.
Advanced Materials Research 647: 30-36.
https://doi.org/10.4028/www.scientific.net/amr.647.30.

Saleh, Bassiouny, Jinghua Jiang, Reham Fathi, et al. 2020.
30 Years of functionally graded materials: An overview of manufacturing methods, applications and future challenges.
Composites Part B: Engineering 201: 108376.
https://doi.org/10.1016/j.compositesb.2020.108376.

Singh, S.J., et S.P. Harsha. 2020.
Thermo-mechanical analysis of porous sandwich s-FGM plate for different boundary conditions using Galerkin Vlasov's method: A semi-analytical approach.
Thin-Walled Structures 150: 106668.
https://doi.org/10.1016/j.tws.2020.106668.

Singh, Surya Dev, et Rosalin Sahoo. 2021.
Analytical solution for static and free vibration analysis of functionally graded CNT-reinforced sandwich plates.
Archive of Applied Mechanics 91 (9): 3819-34.
https://doi.org/10.1007/s00419-021-01979-1.

Soldatos, K.P., et T. Timarci. 1993.

A unified formulation of laminated composite, shear deformable, five-degrees-of-freedom cylindrical shell theories.
Composite Structures 25 (1-4) : 165-71.
https://doi.org/10.1016/0263-8223(93)90162-j.

Srinivas, S., et A.K. Rao. 1970.
Bending, vibration and buckling of simply supported thick orthotropic rectangular plates and laminates.
International Journal of Solids and Structures 6 (11): 1463-81.
https://doi.org/10.1016/0020-7683(70)90076-4.

Swaminathan, K., Sachin Hirannaiah, et T. Rajanna. 2023.
Vibration and stability characteristics of functionally graded sandwich plates with/without porosity subjected to localized edge loadings.
Mechanics Based Design of Structures and Machines 51 (11): 6254-92.
https://doi.org/10.1080/15397734.2022.2038619.

Szabó, B.A. 1991.
On reliability in finite element computations.
Computers & Structures 39 (6) : 729-34.
https://doi.org/10.1016/0045-7949(91)90216-9.

Szabo, B.A., et R.L. Actis. 1996.
Finite element analysis in professional practice.
Computer Methods in Applied Mechanics and Engineering 133 (3-4): 209-28.
https://doi.org/10.1016/0045-7825(95)00941-8.

Szilard, Rudolph. 2004.
Theories and applications of plate analysis: classical, numerical, and engineering methods.
John Wiley.

Tahir, Saeed I., Abdelbaki Chikh, Abdelouahed Tounsi, Mohammed A. Al-Osta, Salah U. Al-Dulaijan, et Mesfer M. Al-Zahrani. 2021.
Wave propagation analysis of a ceramic-metal functionally graded sandwich plate with different porosity distributions in a hygro-thermal environment.
Composite Structures 269 : 114030.
https://doi.org/10.1016/j.compstruct.2021.114030.

Tammas-Williams, S., P. J. Withers, I. Todd, et P. B. Prangnell. 2017.
The influence of porosity on fatigue crack initiation in additively manufactured Titanium components.
Scientific Reports 7 (1).
https://doi.org/10.1038/s41598-017-06504-5.

Thai, Chien H., Loc V. Tran, Dung T. Tran, T. Nguyen-Thoi, et H. Nguyen-Xuan. 2012.
Analysis of laminated composite plates using higher-order shear deformation plate theory and node-based smoothed discrete shear gap method.
Applied Mathematical Modelling 36 (11): 5657-77.
https://doi.org/10.1016/j.apm.2012.01.003.

Thai, Huu-Tai, et Seung-Eock Kim. 2011.
Levy-type solution for buckling analysis of orthotropic plates based on two variable refined plate theory.
Composite Structures 93 (7) : 1738-46.
https://doi.org/10.1016/j.compstruct.2011.01.012.

Thai, Huu-Tai, et Seung-Eock Kim. 2013.
A simple Quasi-3D sinusoidal shear deformation theory for functionally graded plates.
Composite Structures 99 : 172-80.
https://doi.org/10.1016/j.compstruct.2012.11.030.

Timošenko, Stepan P., et Sergius Woinowsky-Krieger. 1996.
Theory of Plates and Shells. 2. ed.
McGraw-Hill Classic Textbook Reissue. McGraw-Hill.

Tossapanon, Prapot, et Nuttawit Wattanasakulpong. 2020.
Flexural vibration analysis of functionally graded sandwich plates resting on elastic foundation with arbitrary boundary conditions: Chebyshev collocation technique.
Journal of Sandwich Structures & Materials 22 (2): 156-89.
https://doi.org/10.1177/1099636217736003.

Touratier, M. 1991.
An efficient standard plate theory.
International Journal of Engineering Science 29 (8): 901-16.
https://doi.org/10.1016/0020-7225(91)90165-y.

Van Vinh, Pham. 2023.
Deflections, stresses and free vibration analysis of bi-functionally graded sandwich plates resting on Pasternak's elastic foundations via a hybrid Quasi-3D theory.
Mechanics Based Design of Structures and Machines 51 (4): 2323-54.
https://doi.org/10.1080/15397734.2021.1894948.

Van Vinh, Pham, et Le Quang Huy. 2022.
Finite element analysis of functionally graded sandwich plates with porosity via a new hyperbolic shear deformation theory.
Defence Technology 18 (3): 490-508.
https://doi.org/10.1016/j.dt.2021.03.006.

Volterra, E., E. C. Zachmanoglou, et H. Kolsky. 1966.
Dynamics of Vibrations.
Journal of Applied Mechanics 33 (4): 956-956.
https://doi.org/10.1115/1.3625222.

Vu, Tan-Van, et Huu-Loi Cao. 2023.
Deflection and natural frequency analysis of FG porous plates embedded in elastic foundations using four-variable hyperbolic Quasi-3D theory.
Arabian Journal for Science and Engineering 48 (4): 5407-45.
https://doi.org/10.1007/s13369-022-07423-y.

Vu, Tan-Van, H. T. Tai Nguyen, Hieu Nguyen-Van, Trong-Phuoc Nguyen, et Jose L. Curiel-Sosa. 2021.
A refined Quasi-3D logarithmic shear deformation theory-based effective meshfree method for analysis of functionally graded plates resting on the elastic foundation.
Engineering Analysis with Boundary Elements 131: 174-93.
https://doi.org/10.1016/j.enganabound.2021.06.021.

Vu, Tan-Van, Hieu Nguyen-Van, Cung H. Nguyen, Trong-Phuoc Nguyen, et Jose L. Curiel-Sosa. 2023.
Meshfree analysis of functionally graded plates with a novel four-unknown arctangent exponential shear deformation theory.
Mechanics Based Design of Structures and Machines 51 (2): 1082-114.
https://doi.org/10.1080/15397734.2020.1863227.

Watari, Fumio, Atsuro Yokoyama, Mamoru Omori, et al. 2004.
Biocompatibility of materials and development to functionally graded implant for bio-medical application.
Composites Science and Technology 64 (6): 893-908.
https://doi.org/10.1016/j.compscitech.2003.09.005.

Wittrick, W.H. 1987.
Analytical, three-dimensional elasticity solutions to some plate problems, and some observations on Mindlin's plate theory.
International Journal of Solids and Structures 23 (4): 441-64.
https://doi.org/10.1016/0020-7683(87)90010-2.

Xiang, Song, Gui-wen Kang, Ming-sui Yang, et Yan Zhao. 2013.
Natural frequencies of sandwich plate with functionally graded face and homogeneous core.
Composite Structures 96 : 226-31.
https://doi.org/10.1016/j.compstruct.2012.09.003.

Yang, P.Constance, Charles H. Norris, et Yehuda Stavsky. 1966.
Elastic wave propagation in heterogeneous plates.
International Journal of Solids and Structures 2 (4): 665-84.
https://doi.org/10.1016/0020-7683(66)90045-x.

Zenkour, A.M. 2005.
A comprehensive analysis of functionally graded sandwich plates: part 1—deflection and stresses.
International Journal of Solids and Structures 42 (18-19): 5224-42.
https://doi.org/10.1016/j.ijsolstr.2005.02.015.

Zenkour, Ashraf M. 2018.
A Quasi-3D refined theory for functionally graded single-layered and sandwich plates with porosities.
Composite Structures 201 : 38-48.
https://doi.org/10.1016/j.compstruct.2018.05.147.

Zhang, Wei, Chunxiao Wang, et Yuewu Wang. 2023.
Thermo-mechanical analysis of porous functionally graded graphene reinforced cylindrical panels using an improved third order shear deformable model.
Applied Mathematical Modelling 118: 453-73.
https://doi.org/10.1016/j.apm.2023.01.026.

Zhang, Yantao, Guoyong Jin, Mingfei Chen, Tiangui Ye, Chuanmeng Yang, et Yaowei Yin. 2020.
Free vibration and damping analysis of porous functionally graded sandwich plates with a viscoelastic core.
Composite Structures 244 : 112298.
https://doi.org/10.1016/j.compstruct.2020.112298.

Zhou, Kai, Xiuchang Huang, Jiajin Tian, et Hongxing Hua. 2018.
Vibration and flutter analysis of supersonic porous functionally graded material plates with temperature gradient and resting on elastic foundation.
Composite Structures 204 : 63-79.
https://doi.org/10.1016/j.compstruct.2018.07.057.

Zhu, Ping, Z.X. Lei, et K.M. Liew. 2012.
Static and free vibration analyses of carbon nanotube-reinforced composite plates using finite element method with first order shear deformation plate theory.
Composite Structures 94 (4) : 1450-60.
https://doi.org/10.1016/j.compstruct.2011.11.010.

Zienkiewicz, O.C., and Taylor, R.L. 1994.
The finite element method, fourth edition, vol. 1 basic formulation and linear programs.
McGraw-Hill Book Company Europe.

Appendix A

A.1 Analytical solution for FGM plates

The equilibrium equation regarding forced vibration based on the Classical Plate Theory (CPT), expressed in terms of the plate deflections (w), can be written as:

$$D_f\left(\frac{\partial^4 w}{\partial x^4}+2\frac{\partial^4 w}{\partial x^2\partial y^2}+\frac{\partial^4 w}{\partial x^4}\right)+I_0\frac{\partial^2 w}{\partial t^2}=p(x,y,t) \tag{A.1}$$

For a square plate with all edges simply supported boundary conditions along its edges, and to facilitate the demonstration, we assume that the side length of the plate is 2a. The plate's transverse displacement is given by [31].

$$w(x,y,t)=\sum_{i=1,3,5\ldots}^{\infty}\sum_{j=1,3,5\ldots}^{\infty}W_{ij}\sin\left(\frac{i\pi x}{2a}\right)\sin\left(\frac{j\pi y}{2a}\right) \tag{A.2}$$

By substituting Eq. (A.2) into Eq. (A.1), we obtain

$$\frac{D_f\pi^4}{I_0}\left(\sum_{i=1,3,5\ldots}^{\infty}\sum_{j=1,3,5}^{\infty}\left(\left(\frac{i}{2a}\right)^4+\left(\frac{j}{2a}\right)^4+2\left(\frac{i}{2a}\right)^2\left(\frac{j}{2a}\right)^2\right)W_{mn}\sin\left(\frac{i\pi x}{2a}\right)\sin\left(\frac{j\pi y}{2a}\right)\right)$$
$$=\frac{p(x,y,t)}{I_0}-\sum_{i=1,3,5\ldots}^{\infty}\sum_{j=1,3,5\ldots}^{\infty}\frac{d^2W_{ij}}{dt^2}\sin\left(\frac{i\pi x}{2a}\right)\sin\left(\frac{j\pi x}{2a}\right) \tag{A.3}$$

Multiply both sides of Eq. (A.3) by $\sin\left(\frac{i\pi x}{2a}\right)\sin\left(\frac{j\pi y}{2a}\right)$ and integrate over $0 \le x \le 2a$ and $0 \le y \le 2a$. Through the use of trigonometric orthogonality relations, Eq. (A.3) is transformed into

$$\frac{d^2W_{ij}}{dt^2}+\frac{D_f\pi^4}{I_0}\left(\frac{i^2+j^2}{(2a)^2}\right)^2W_{ij}(t)=\frac{P_{ij}(t)}{a^2I_0} \tag{A.4}$$

where

$$P_{ij}(t)=\int_0^{2a}\int_0^{2a}C_0\sin\left(\frac{i\pi x}{2a}\right)\sin\left(\frac{j\pi y}{2a}\right)dx\,dy \tag{A.5}$$

The general solution of Eq. (A.5) can then be written as [32].

$$W_{ij}(t)=B_{ij}\cos\left[\pi^2\left(\frac{i^2+j^2}{(2a)^2}\right)\sqrt{\frac{D_f}{I_0}}t\right]$$
$$+\overline{B}_{ij}\sin\left[\pi^2\left(\frac{i^2+j^2}{(2a)^2}\right)\sqrt{\frac{D_f}{I_0}}t\right] \tag{A.6}$$
$$+\frac{4}{\pi^2(2a)^2I_0\left(\frac{i^2+j^2}{(2a)^2}\right)\sqrt{\frac{D_f}{I_0}}}\times\int_0^t P_{ij}(\tau)\sin\left[\pi^2\left(\frac{i^2+j^2}{(2a)^2}\right)\sqrt{\frac{D_f}{I_0}}(t-\tau)d\tau\right]$$

Considering the imposed initial conditions (plate initially at rest): $w(x,y,t) = 0, \dot{w}(x,y,0) = 0$, B_{ij} and $\overline{B}_{ij}$ in Eq. (A.6), which correspond to the free vibration component, are zero [Timošenko et Woinowsky-Krieger (1996)]. Thus, the function P_{ij} defined in Eq. (A.5) takes the form

$$P_{ij} = \frac{16C_0a^2}{\pi^2 ij} \tag{A.7}$$

Substituting the Eq. (A.7) in Eq. (A.6) gives

$$W_{ij}(t) = \frac{16C_0}{\pi^6 ij\left(\frac{i^2+j^2}{4a^2}\right)^2 D_f} \times \left[1 - \cos\left(\pi^2\left(\frac{i^2+j^2}{(2a)^2}\right)\sqrt{\frac{D_f}{I_0}}\right)t\right] \tag{A.8}$$

with

$$\omega_{ij} = \frac{\pi^2(i^2+j^2)}{4\,a^2}\sqrt{\frac{D_f}{I_0}} \tag{A.9}$$

In the case where $p(x,y,t) = C_0$ is a localized load acts at the center of the plate, the expression describing the central deflection can be written as

$$w(a,a,t) = \frac{4C_0}{\pi^4 D_f}\sum_{i=1,3,5\ldots}^{\infty}\sum_{j=1,3,5\ldots}^{\infty}\frac{1-\cos(\omega_{ij}t)}{\left(\frac{i^2+j^2}{4a^2}\right)^2}\sin\left(\frac{i\pi}{2}\right)\sin\left(\frac{j\pi}{2}\right) \tag{A.10}$$

Consequently, the flexural stiffness and inertial coefficient of the FGM plate are expressed as

$$w(a,a,t) = \frac{16C_0a^2}{\pi^4 D_f}\sum_{i=1,3,5\ldots}^{\infty}\sum_{j=1,3,5\ldots}^{\infty}\frac{1-\cos(\omega_{ij}t)}{(i^2+j^2)^2} \tag{A.11}$$

where

$$D_f = \int_{\frac{-h}{2}}^{\frac{h}{2}} \frac{z^2E(z)}{1-\nu^2}\,dz \tag{A.12.1}$$

and,

$$I_0 = \int_{\frac{-h}{2}}^{\frac{h}{2}} \rho(z)\,dz \tag{A.12.2}$$

The derived expressions for the flexural stiffness and inertial coefficient of the FGM plate are

$$D_f = \frac{(E_c - E_m)h^3}{1-\nu^2}\left\{\frac{1}{n+3} - \frac{1}{n+2} + \frac{1}{4(n+1)}\right\} + \frac{E_mh^3}{12(1-\nu^2)} \tag{A.13.1}$$

and,

$$I_0 = \frac{(\rho_c - \rho_m)h}{n+1} + \rho_m h \tag{A.13.2}$$

For an isotropic plate, the flexural stiffness and inertial coefficient are expressed as

$$D_f = \frac{Eh^3}{12(1-\nu^2)} \tag{A.14.1}$$

and

$$I_0 = \rho h \tag{A.14.2}$$

Therefore, the central deflection of an isotropic plate is written as

$$w(a,a,t) = \frac{192C_0a^2(1-\nu^2)}{\pi^4 Eh^3} \sum_{i=1,3,5\ldots}^{\infty} \sum_{j=1,3,5\ldots}^{\infty} \frac{1-\cos(\omega_{ij}t)}{(i^2+j^2)^2} \tag{A.15}$$

With

$$\omega_{ij} = \frac{\pi^2(i^2+j^2)h}{4\,a^2}\sqrt{\frac{E}{12(1-\nu^2)\rho}} \tag{A.16}$$

Abstract

Functionally graded material (FGM) sandwich plates are widely used as structural components in various branches of engineering such as mechanical, aerospace, civil, and naval engineering. To ensure proper design and performance of these structures, it is essential to analyze and understand their behavior. In this thesis, both the static and dynamic behavior of FGM sandwich plate incorporate the effect of porosity distribution and Carbone nanotube (CNT) reinforcement are analyzed using the p-version of the Finite Element Method (p-FEM) based on the First- order Deformation Theory (FSDT). The sandwich plate consists of three layers, where the core layer is made of functionally graded carbon nanotube-reinforced material (FG-CNTR), including three distribution types: Uniform, FG-X, and FG-O. The top and bottom face sheets are composed of a porous functionally graded material (FGM), modeled using five different porosity distributions: Perfect, Imperfect I, …, V. The numerical results demonstrate convergence and are validated through comparison with previously published data, confirming the accuracy of the proposed formulation. The dynamic behavior is analyzed by comparing the results obtained from the p-version of the (FEM) with the mode superposition approach those derived from a newly developed analytical solution formulated within the framework of the Classical Plate Theory (CPT). The effects of several parameters such as the carbon nanotube distribution pattern, porosity model, CNT volume fraction, geometric characteristics, mechanical loading, volume fraction exponent, damping coefficient, and boundary conditions are thoroughly illustrated and analyzed for static and dynamic responses.

Keywords: FGM; sandwich plates; p-FEM; dynamic response; static analysis; porosities; FG-CNTRC; FSDT; Carbon nanotubes distribution; bending analysis.

Résumé

Les plaques sandwich en matériau à gradient fonctionnel (FGM) sont largement utilisées comme composants structurels dans divers domaines de l'ingénierie, tels que l'ingénierie mécanique, aérospatiale, civile et navale. Pour assurer une conception appropriée et des performances optimales de ces structures, il est essentiel d'analyser et de comprendre leur comportement. Dans cette thèse, les comportements statique et dynamique des plaques sandwich FGM, en tenant compte de l'effet de la distribution de porosité et du renforcement par nanotubes de carbone, sont analysés en utilisant la méthode des éléments finis (MEF) en p-version basée sur la théorie des déformations du premier ordre. La plaque sandwich est constituée de trois couches, où la couche centrale est faite d'un matériau renforcé par des nanotubes de carbone à gradient fonctionnel (FG-CNTR), comprenant trois types de distribution : Uniforme, FG-X et FG-O. Les faces supérieure et inférieure sont composées d'un matériau à gradient fonctionnel poreux (FGM), modélisé selon cinq distributions de porosité différentes : Parfaite, Imperfect I, …, V. Les résultats numériques démontrent la convergence et sont validés par comparaison avec des données publiées précédemment, confirmant l'exactitude de la formulation proposée. Le comportement dynamique est analysé en comparant les résultats obtenus par la p-version de la MEF utilisant la méthode de superposition des modes avec ceux dérivés d'une solution analytique récemment développée, formulée dans le cadre de la théorie classique des plaques. Les effets de plusieurs paramètres, tels que le type de distribution des nanotubes de carbone, le modèle de porosité, la fraction volumique de Carbone nanotube, les caractéristiques géométriques, la charge mécanique, l'exposant de la fraction volumique, le coefficient d'amortissement et les conditions aux limites, sont décrits et analysés en profondeur pour les réponses statiques et dynamiques.

Mots clés : FGM ; plaques sandwich ; p-MEF ; réponse dynamique ; analyse statique ; porosités ; FG-CNTRC ; Théorie du premier ordre des plaques ; distribution des nanotubes de carbone ; analyse de flexion.

ملخص

تُستخدم صفائح الساندويتش المصنوعة من المواد متدرجة الخصائص على نطاق واسع كمكونات هيكلية في مختلف فروع الهندسة، مثل الهندسة الميكانيكية، والهندسة الفضائية، والهندسة المدنية، والهندسة البحرية. لضمان تصميم مناسب وأداء مثالي لهذه الهياكل، من الضروري تحليل سلوكها وفهمه. في هذه الأطروحة تم تحليل السلوكين الثابت والديناميكي لصفائح الساندويتش مع الأخذ بعين الاعتبار تأثير توزيع المسامية وتعزيزها بـالأنابيب النانوية الكربونية باستخدام النسخة p من طريقة العناصر المحددة المستندة إلى نظرية تشوه القص من الرتبة الأولى. تتكون صفيحة الساندويتش متدرجة الخصائص من ثلاث طبقات، حيث تتألف الطبقة الوسطى من مادة معززة بـالأنابيب النانوية الكربونية، وتشمل ثلاثة أنواع من التوزيع Uniform، FG-X وFG-O، أما الطبقات العليا والسفلى فهي مكونة من مادة متدرجة الخصائص مسامية تم نمذجتها وفق خمسة توزيعات مختلفة للمسامية Perfect، Imperfect I،...،V. تُظهر النتائج العددية التقارب وتم التحقق من صحتها بالمقارنة مع البيانات المنشورة مسبقًا، مما يؤكد دقة الصياغة يتم تحليل السلوك الديناميكي من خلال مقارنة النتائج التي تم الحصول عليها بواسطة (p-FEM) باستخدام طريقة تراكب الأوضاع (mode superposition method)مع النتائج المستمدة من حل تحليلي تم تطويره حديثًا وصياغته ضمن إطار نظرية الصفائح الكلاسيكية.قدمت هذه الدراسة تأثير عدة عوامل مثل نوع توزيع الانابيب النانوية الكربونية، المسامية، الكسر الحجمي للكربون، الخصائص الهندسية، القوى الميكانيكية، أسس كسر الحجم، معامل التخميد، والظروف الحدودية بشكل مفصل للاستجابات الثابتة والديناميكية.

الكلمات المفتاحية :المواد المتدرجة وظيفيا؛ صفائح الساندويتش؛ النسخة p من طريقة العناصر المحددة؛ الاستجابة الديناميكية؛ التحليل الثابت؛ المسامية؛ النسخة p من طريقة العناصر المحددة؛ توزيع الأنابيب النانوية الكربونية؛ تحليل الانحناء.